Functional analysis of the parkinsonism-associated protein FBXO7 (PARK15) in neurons

Ph.D. Thesis

in partial fulfillment of the requirements for the award of the degree

"Doctor rerum naturalium"

in the Neuroscience Program

at the Georg-August-Universität Göttingen

Faculty of Biology

Submitted by

Guergana Ivanova Dontcheva

born in

Gabrovo, Bulgaria

Aachen 2017

Functional analysis of the parkinsonism-associated protein FBXO7 (PARK15) in neurons

Ph.D. Thesis

in partial fulfillment of the requirements for the award of the degree

"Doctor rerum naturalium"

in the Neuroscience Program

at the Georg-August-Universität Göttingen

Faculty of Biology

Submitted by

Guergana Ivanova Dontcheva

born in

Gabrovo, Bulgaria

Aachen 2017

Members of the Thesis Committee:

P.D. Dr. Judith Stegmüller, Reviewer

Department of Cellular and Molecular Neurobiology, Max Planck Institute of Experimental Medicine, Göttingen, Germany

Department of Neurology, University Hospital, RWTH Aachen, Germany

Prof. Dr. Anastassia Stoykova, Reviewer

Department of Molecular Developmental Neurobiology, Max Planck Institute for Biophysical Chemistry, Göttingen, Germany

Prof. Dr. Nils Brose

Department of Molecular Neurobiology, Max Planck Institute of Experimental Medicine, Göttingen, Germany

Date of submission: 03 May, 2017

Date of oral examination: 23 June, 2017

Affidavit

I hereby declare that this Ph.D. Thesis entitled "**Functional analysis of the parkinsonism-associated protein FBXO7 (PARK15) in neurons**" has been written independently with no external sources or aids other than quoted.

Guergana Dontcheva

April 2017

Aachen, Germany

Table of Contents

List of Figures

List of Tables

Abstract

Parkinson's disease (PD) is a debilitating neurodegenerative disease affecting the elderly population. It has been a challenge elucidating the molecular mechanisms underlying the selective loss of dopaminergic neurons, since much of the etiopathology of the disease remains unknown. Genetic studies of the familial PD cases have yielded a handful of Parkinson's related loci- the *PARK* loci, that have attributed most of the molecular knowledge we have. In this study, I investigated the role of PARK15- the FBXO7 protein in neurons at the molecular, cellular and histological level. I found that FBXO7 interacts with the microtubule associated protein 1B light chain 1 (MAP1B LC1) independently of its E3-ligase activity. Furthermore, FBXO7 is an important factor in mitochondrial maintenance and it is essential for neuronal morphogenesis. Quantitative mass spectrometry supported this data and further expanded the involvement of FBXO7 in multiple cellular mechanisms such as DNA repair and vesicular transport. Additionally, I examined the effect of knockout of *Fbxo7* in the forebrain in *Mus musculus*, and observed a generalized brain damage without the loss of cortical neurons. Taken together, these findings further broaden our understanding of the pathological mechanisms leading to neuronal death in PD patients.

1. Introduction

1.1. Parkinson's Disease

Ever since humanity discovered the healing benefit of plants, the goal of medicine has been to increase the life expectancy and decrease pain and suffering. In modern history, the introduction of penicillin, vaccinations and advances in health care have led to an unprecedented life expectancy highs, largely due to decrease in child mortality (Jamison et al., 2013). The new objective of medicine has then shifted to increase the quality of life of the ever-growing elderly population.

Parkinson's disease (PD) is the most common neurodegenerative motor disorder (Van Laar and Berman, 2009), and it is estimated that it affects about 1% of the population older than 65 and 4% of the population older than 80 years (de Lau and Breteler, 2006). The major risk factor of PD is aging and it was grossly considered sporadic in its etiopathology (de Lau and Breteler, 2006) until 1983, when a group of young people developed PD-like symptoms after intravenous injection of 1-Methyl-4-phenyl-1,2,3,6-tetrahydropyridin (MPTP)-containing drugs (Langston et al., 1983; Shulman et al., 2011). The patients presented very severe form of parkinsonism, substantiated by stiffness and immobility, fixed stare (bradykinesia), "pill-rolling" tremor and postural instability (Langston et al., 1983). It was predicted that the patients had selective loss of dopaminergic neurons in substantia nigra- the major histopathological hallmark of PD, next to Lewy body pathology (Braak et al., 2003; Langston et al., 1983). The earliest genetic studies, showing that PD may also be caused by hereditary mutations in these genes, were performed in 1996, identifying the first monogenetic *PARK1/4* locus (4q21) also known as *SNCA*, encoding the α–synuclein protein and the major constituent of Lewy Bodies (Polymeropoulos et al., 1996; Shulman et al., 2011; Wakabayashi et al., 1998). Lewy bodies are intracellular aggregation of proteins into fibrils, known as inclusions, where the α–synuclein fibrils are accompanied by many other proteins including FBXO7 and ubiquitin (Engelender, 2008; Zhao et al., 2013). In the following years, a total of 18 PD related loci were identified accounting for around 10% of the total PD cases (Klein and Westenberger, 2012). These encode most notably Parkin, PTEN-induced putative kinase 1 (PINK1), DJ-1, Leucine-rich repeat kinase 2 (LRRK2), ATPase 13A2 (ATP13A2), F-box protein other 7 (FBXO7) and the vacuolar protein sorting-associated protein 35 (VPS35) which together defined the familial PD as genetically heterogenous (Klein and Schlossmacher, 2007; Klein and Westenberger, 2012). Even though these cases account for only a small fraction of the total epidemiology of PD, studying these genes has granted us invaluable insights into the cellular pathology leading to neurodegeneration.

1.2. The Parkinsonian pyramidal syndrome

Mutations in the FBXO7 gene were first recognized by Shojaee *et al*. where the authors performed a genome-wide linkage analysis on a large Iranian pedigree with Parkinsonian-pyramidal syndrome (PPS) (Shojaee et al., 2008). The exact onset of the disease is not specified but the clinical symptoms are well characterized: all patients exhibited pyramidal syndromes such as Babinski sign, spasticity in lower limbs and hyperactive deep tendon reflexes (Shojaee et al., 2008). Extrapyramidal symptoms such as rigidity and bradykinesia, characteristic of parkinsonism, have evolved at later stages and not in all patients and none of the patients had tremor or dementia (Shojaee et al., 2008). Since PPS is a rarely developed syndrome and the fact that the affected offspring was from a consanguineous family, it was suggested that the mutation (R378G) segregates with the PPS in an autosomal recessive inheritance pattern (Shojaee et al., 2008). Further mutations on FBXO7 were identified by Di Fonzo *et al.*: the R498X truncating mutation in a Dutch family and the compound heterozygous mutation at the splice-site IVS7 + 1G/T together with the missense T22M mutation in an Italian family (Di Fonzo et al., 2009). Both mutations resulted in early-onset parkinsonism- 10 and 13 years of age for the Dutch family and 18 and 19 years for the Italian family, followed by pyramidal signs and no cognitive disturbances (Di Fonzo et al., 2009). Further cases of the R498X mutation were reported with similar clinical symptoms but these did not exhibit pyramidal signs (Paisan-Ruiz et al., 2010; Yalcin-Cakmakli et al., 2014). Lastly, two single nucleotide polymorphisms (SNPs) of the *Fbxo7* gene were identified in a Taiwanese cohort with early onset of PD- the Y52C and the M115I, but clinical data on these is sparse (Chen et al., 2014). Interestingly, a new L34R mutation in a Turkish family was shown to lead to a classical late onset PD (Lohmann et al., 2015).

All of the patients' clinical reports include early-onset parkinsonism-like motor dysfunctions together with pyramidal signs **(Table 1.1)**. A striking distinction between PPS and PD patients is that non-motor features of PPS patients were significantly different from the classical PD. In classical PD, the prodromal features such as disturbances in the rapid eye movement (REM) sleeping behavior, loss of olfaction, autonomic disturbances, depression and anxiety are usually followed by cognitive impairment such as dementia as well as verbal and attention deficits as the disease progresses (Goldman and Postuma, 2014). Patients with PPS have a large spectrum of non-motor disturbances, ranging from none to mental retardation (Shojaee et al., 2008; Yalcin-Cakmakli et al., 2014). The clinical data of patients with early-onset parkinsonism is summarized in **Table 1.1**

Table 1.1 **List of patients with parkinsonian pyramidal syndrome with the corresponding mutations in the *Fbxo7* gene**

Patient (reference)	Mutation /SNP	Age at onset	Ethnical background	Pyramidal syndrome	Parkinsonism	Non-motor symptoms
Various, (Shojaee et al., 2008)	R378G	N/A	Iranian	+	not all patients; none had tremors	-
BO-53, (Di Fonzo et al., 2009)	R498X	10	Italian	+	+	unsteadiness
BO-56, (Di Fonzo et al., 2009)	R498X	13	Italian	+	+	Unsteadiness
NIJ-002, (Di Fonzo et al., 2009)	IVS7+1G/T;T22M	18	Dutch	+	+ (no tremor)	Nervousness
NIJ-006, (Di Fonzo et al., 2009)	IVS7+1G/T;T22M	19	Dutch	+	+	social withdrawal
FamilyC-Pat2, (Paisan-Ruiz et al., 2010)	R498X	24	Pakistani	+	+ (no tremor)	cognitive decline
FamilyC-Pat3, (Paisan-Ruiz et al., 2010)	R498X	17	Pakistani	+	+ (no tremor)	cognitive decline
FamilyD-Pat1, (Paisan-Ruiz et al., 2010)	R498X	17	Turkish	-	+ (no data for tremor)	-
ANK-07, (Yalcin-Cakmakli et al., 2014)	R498X	14	Turkish	-	+	poor scholastic performance
ANK-07, (Yalcin-Cakmakli et al., 2014)	R498X	10	Turkish	-	+	mentally challenged; cognitive dysfunction
N/A, (Chen et al., 2014)	Y52C	N/A	Taiwanese	-	+	N/A

1.3. Fbxo7 and FBXO7

The variance in clinical symptoms in PPS patients can be attributed to the fact that they are elicited by different mutations in the *Fbxo7* gene, all located within different functional domains of the protein **(Fig. 1.1)** (Nelson et al., 2013).

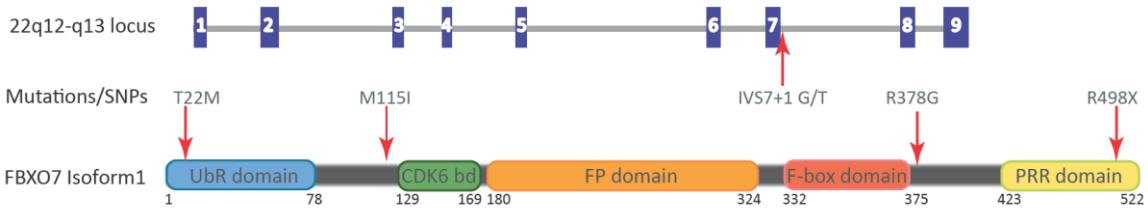

Fig. 1.1 The Fbxo7 locus, transcript and pathological mutations

Schematic representation of the nine exons of the *Fbxo7* gene in blue boxes and the primary protein structure with its different domains. The pathological mutations and SNP along the protein and the gene (splicing mutation) are indicated with red arrows. (UbR= ubiquitin related; Cdk6 bd= cyclin-dependent kinase 6 binding domain; FP= FBXO7/PI31; PRR= Proline rich)

The *Fbxo7* locus is on the long arm of chromosome 22 and it comprises of nine exons, further transcribed into three functional isoforms (Nelson et al., 2013). Isoform 1 has the longest mRNA transcript encoded by 552 amino acids and it is expressed in all types of human and murine tissue: brain, heart, kidney, liver, lung, spleen, skeletal muscle, pancreas and the placenta (Vingill et al., 2016; Winston et al., 1999). The functional domains were discovered chronologically and are involved in different cellular mechanisms, including cell cycle, proteasome regulation, ubiquitination and mitophagy (Burchell et al., 2013; Cenciarelli et al., 1999; Kirk et al., 2008; Laman et al., 2005; Vingill et al., 2016)

1.3.1. FBXO7 functions in cell cycle and proteostasis

While studying the cell cycle mechanisms in yeast, Bai *et al.* identified Skp1 as the direct interactor of mitotic cyclin F through a novel evolutionary conserved 40 amino acid motif the F-box **(Fig. 1.1)** (Bai et al., 1996). The authors stressed the importance of the precise timing and the balance of expression and degradation of the cell cycle related proteins in order to ensure the orchestration of the cell cycle transitions (Bai et al., 1996). The spatial and temporal control is largely accomplished by the post-translational ubiquitination of an array of proteins, and thus the binding of Skp1 to the F-box domain of proteins was identified as the link between the ubiquitin proteasome system (UPS) and the cell cycle regulators (Bai et al., 1996).

FBXO7 was firstly identified simultaneously by two research groups as part of a family of F-box proteins whose main role was constituting one of the subunits of the Skp1-cul1-F-box protein (SCF) E3 ubiquitin ligase **(Fig. 1.2)** (Cenciarelli et al., 1999; Winston et al., 1999). Within a short span of time, it was recognized that FBXO7 has not only SCF but also non-SCF functions, where the latter is implicated in cell-cycle progression (Laman et al., 2005). It was found that FBXO7 interacts with the D cyclin/cdk6 complexes through its CDK6 domain rather more as an assembly protein than an E3 ubiquitin ligase subunit **(Fig. 1.1)** (Laman et al., 2005). Through this interaction, FBXO7 was inaugurated as a potential proto-oncogene, since its overexpression leads to enhancement of the D cyclin/cdk6 assembly and subsequently activation, ultimately leading to transforming healthy cells into malignant (Laman et al., 2005).

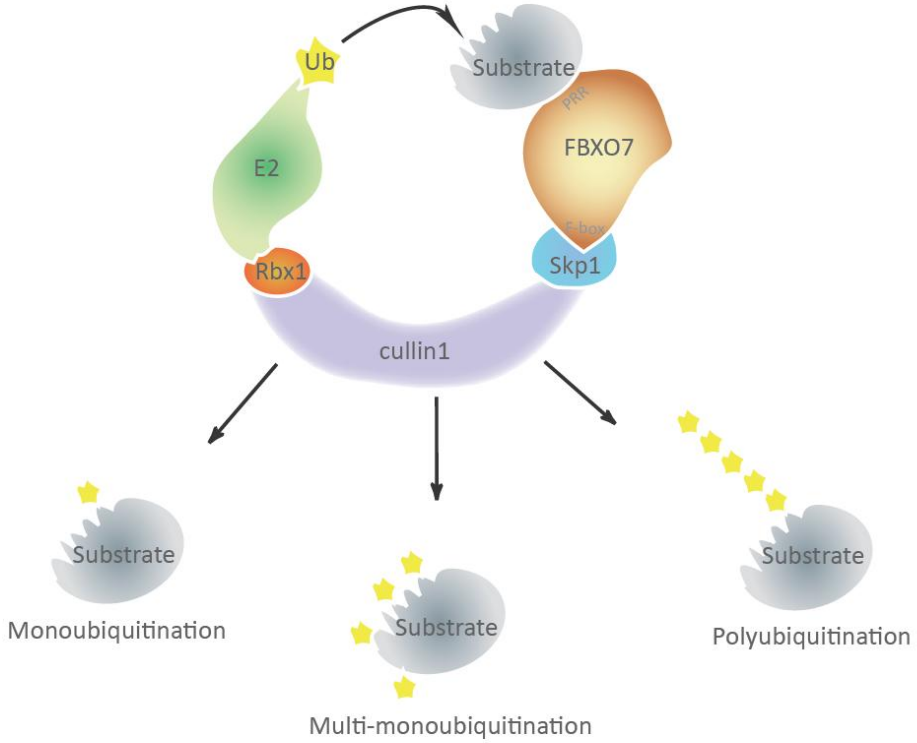

Fig. 1.2 The FBXO7-SCF ligase complex

The FBXO7-SCF ligase complex comprises of four major subunits- Rbx1, culllin1, Skp1 and FBXO7. The PRR domain on the FBXO7 protein recruits the substrate and the F-box domain is indispensable for its interaction with Skp1. Upon the assembly of the E2 and the E3 complex, the substrate can get mono-, multi-mono or polyubiquitinated.

FBXO7's function as the substrate recognition subunit of the SCF E3 ubiquitin ligase was reported in the canonical ubiquitination by the UPS of the Hepatoma Up-regulated Protein (HURP) (Hsu et al., 2004). The recruitment and ubiquitination of the HURP required its phosphorylation and intact FBXO7 C-terminal harboring the proline rich (PRR) domain, indicating that the PRR domain is the substrate-binding domain of the protein **(Fig. 1.2)** (Hsu et al., 2004). Canonical ubiquitination leads to the proteasomal degradation of the ubiquitin-tagged proteins by the UPS in five steps, starting with ubiquitin activation in adenosine triphosphate (ATP)-dependent manner by an E1 enzyme **(Fig. 1.3 i)** (Yi and Ehlers, 2007). Next, ubiquitin is conjugated to an E2 conjugating enzyme **(Fig. 1.3 ii)** that can then associate with E3 ubiquitin ligases, transferring the ubiquitin moiety onto a substrate **(Fig. 1.3 iii)** (Yi and Ehlers, 2007). Next, the ubiquitin tagged protein is degraded by the proteasome again in ATP-dependent manner **(Fig. 1.3 vi)** and finally, ubiquitin is recycled with the help of deubiquitinases (DUB) **(Fig. 1.3 v)** (Yi and Ehlers, 2007).

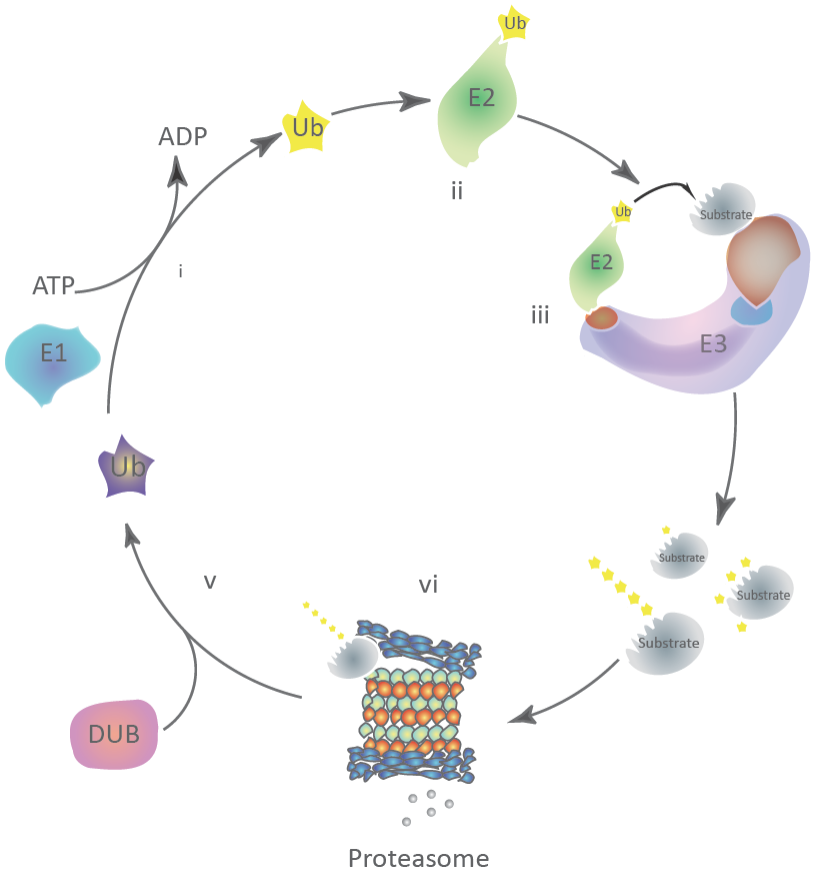

Fig. 1.3 Canonical ubiquitination cycle and the ubiquitin proteasome system

Ub (ubiquitin) is activated by an E1 enzyme utilizing the hydrolysis of ATP (i) and then conjugated to an E2 enzyme (ii). The E2 enzyme forms a complex with the E3 ubiquitin ligase, leading to substrate ubiquitination (iii). The substrate is degraded by the proteasome (vi), and Ub is recycled by deubiquitinases (DUBs) (v).

Ubiquitination can take different forms depending on the type of E2 enzyme, namely, mono-, multi-mono or polyubiquitination **(Fig. 1.2)** (Komander, 2009). When a single ubiquitin molecule is ligated to a lysine (Lys) residue on the substrate (mono-ubiquitination) or to multiple lysine residues (multi-mono-ubiquitination), it can trigger a cascade leading to lysosomal degradation of cell surface receptors or DNA damage response (Komander, 2009). Polyubiquitination on the other hand, can be much more diverse in its functions, since the ubiquitin polymers can be assembled differently depending on the type of lysine linkage (Komander, 2009). For example, Lys48 and Lys11 polyubiquitination leads to proteasomal degradation (canonical ubiquitination) **(Fig. 1.3)**; Lys11 has further non-degradative functions in cell cycle and endoplasmic reticulum-associated degradation (ERAD) pathways; Lys 48 polyubiquitination plays role in endocytosis, DNA-damage response and cytokine signaling and so on (Komander, 2009). This enormous complexity and control of substrate ubiquitination is responsible for the vastness of the acquired physiological roles of the modified protein.

1.3.2. Function of FBXO7 in proteasomal stability

Further research revealed a novel function of FBXO7 in the UPS, not just as part of E3 ubiquitin ligase, but also as regulator of proteasome activity (Bader et al., 2011; Kirk et al., 2008; Vingill et al., 2016). The first report linking FBXO7 with the proteasome inhibitor PI31, unraveled a new domain on the FBXO7 protein that was responsible for the homodimerization of FBXO7 as well as the heterodimerization of FBXO7 with the PI31, and was therefore named FP (FBXO7/PI31) domain **(Fig. 1.1)** (Kirk et al., 2008). This interaction had no effects on the stability of PI31, so it was argued that PI31 is not a substrate for the FBXO7-SCF complex (Kirk et al., 2008). The functional significance of this interaction was later shown in spermatogenesis in *Drosophila melanogaster,* where the fly orthologue of the FBXO7- the Nutcracker regulates the stability of DmPI31 in a positive fashion and mutations in the *nutcracker* resulted in male fly sterility (Bader et al., 2011).

The role and the molecular mechanism in which FBXO7 regulates the proteasome activity in mammals, were elucidated recently by Vingill *et al.* The authors found that FBXO7 interacts directly with the proteasomal subunit α2 (PSMA2) through its ubiquitin related domain (UbRD) **(Fig. 1.1)** leading to its Lys63 polyubiquitination (Vingill et al., 2016). The functional significance of this interaction is that, since FBXO7 facilitates the 20S core particle assembly with the 19S regulatory particles, mutations in *Fbxo7* result in net decrease in proteasomal activity due to increase of the fraction of free regulatory and core partides (Vingill et al., 2016). This reduced

proteasomal activity is then further reflected into the UPS inability to efficiently degrade ubiquitinated proteins (Vingill et al., 2016).

1.3.3. Functions of FBXO7 in mitophagy: the PINK1, Parkin and FBXO7 interaction

The 1-88 amino acid stretch on the FBXO7 partially coinciding with the UbRD **(Fig. 1.1)**, was found to be the binding site for two of the main mitophagy initiators and consecutively *PARK* loci encoding for PINK1 and Parkin (Burchell et al., 2013). Mitophagy is a part of the mitochondrial quality control mechanism together with mitochondrial dynamics and biogenesis (Scarffe et al., 2014). The delicate orchestration of mitochondrial fission, fusion, trafficking, degradation and biogenesis ensures the optimal ATP synthesis at simultaneously the lowest reactive oxygen species (ROS) generation rate (Scarffe et al., 2014). This balance however, can be disrupted by the introduction of mitochondrial stress, which can be initiated genetically or epigenetically (aging, environment), leading to an increase in ROS production (Youle and van der Bliek, 2012). These highly reactive radicals can disrupt the covalent bonds within molecules leading to DNA, protein and lipid aberrations (Youle and van der Bliek, 2012). The cell has evolved a whole battery of protective mechanisms in response to the degree of injury, for example: damaged proteins within mitochondria are repaired by mitochondrial proteases; proteins located on the outer mitochondrial membrane are kept under surveillance and regulated by the UPS and finally, if the mitochondrial damage cannot be handled, mitochondria will be catabolized through mitophagy (Campello et al., 2014). Mitophagy is a specialized process, in which unhealthy mitochondria destined for degradation are sequestered, transported and fused with the lysosomes (Campello et al., 2014). Even though there are many proteins involved in this copious process, two stand out because of their relevance in human disease: PINK1 and Parkin. Mutations in *Parkin (PARK2)* and *PINK1 (PARK6)* account for the highest and second highest prevalence of autosomal-recessive PD respectively (Scarffe et al., 2014). The general mechanism in which these two proteins interact to mediate mitophagy, starts with PINK1 scouting for mitochondria with depolarized inner membranes **(Fig. 1.4)** (Narendra et al., 2012). PINK1 is a serine/threonine protein kinase, that is synthesized in the cytoplasm, but is then transported to mitochondria, where under basal, healthy conditions is cleaved by mitochondrial proteases **(Fig. 1.4 A)** (Narendra et al., 2012; Valente et al., 2004; Whitworth et al., 2008). Upon reduction of the mitochondrial membrane potential ($\Delta\Psi m$), PINK1 accumulates on the outer mitochondrial membrane (OMM) and activates the E3 ubiquitin ligase Parkin by phosphorylating it within Parkin's ubiquitin-like domain (Ubl) **(Fig. 1.4 B)** (Kondapalli et al., 2012; Narendra et al., 2010). Once activated, Parkin then ubiquitinates a number of proteins of which 36 located on the OMM, including Mitofusin1 (Mfn1), Mitofusin2

(Mfn2) and Miro1 **(Fig. 1.4 B)** (Gegg et al., 2010; Sarraf et al., 2013). The ubiquitination of the Mfn1 and 2 arrests mitochondrial fusion, ensuring that damaged mitochondria will be prevented to fuse back into the healthy network of mitochondria **(Fig. 1.4 B)** (Narendra et al., 2012). Furthermore, mitochondrial transport towards the plus (+) end is halted by the degradation of Miro1, speculatively in order to ensure that unhealthy mitochondria cannot be transported to areas with high bio-energetic demands such as the axonal terminus (Narendra et al., 2012).

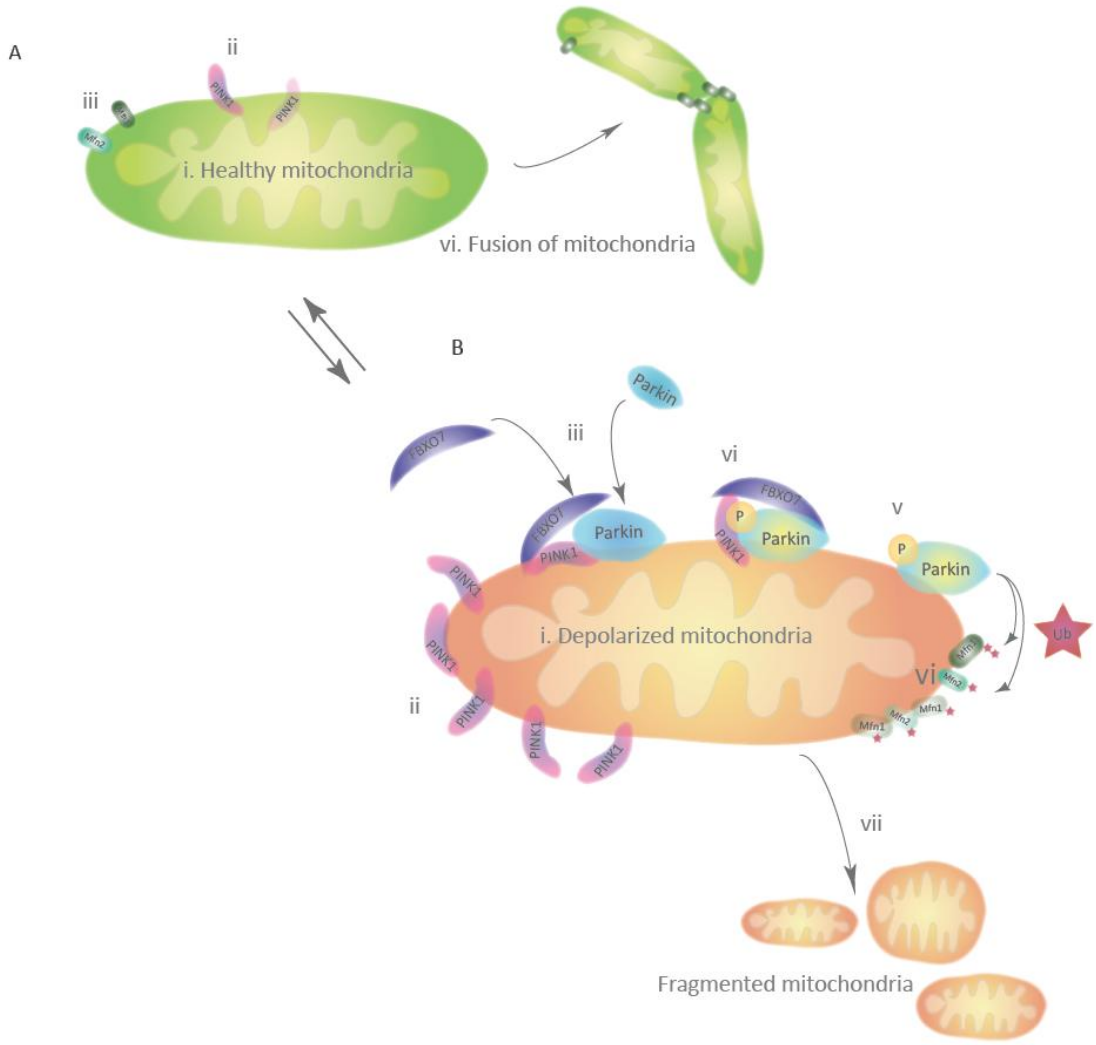

Fig. 1.4 PINK1/Parkin dependent mitochondrial maintenance and mitophagy

(A) Healthy mitochondria with regular $\Delta\Psi m$ (i) express proteinases that degrade PINK1 (ii). Mfn1 and 2 remain intact on the outer mitochondrial membrane OMM (iii) allowing for the fusion of mitochondria to the mitochondrial network (vi). **(B)** Depolarized mitochondria (i) accumulate PINK1 on their OOM, leading to the translocation of FBXO7 from the cytoplasm to the OOM, which acts as a scaffold protein for the formation of the PINK1-Parkin complex (iii). PINK1 then phosphorylates the E3 ligase Parkin, thus activating it (vi). Activated Parkin then ubiquitinates (Ub=ubiquitin) multiple proteins including Mfn1 and 2 (v), leading to their degradation (vi). This prevents mitochondria from fusing leading to their fragmentation (vii).

There are many pieces of the puzzle missing in explaining how exactly mitophagy is mediated by PINK1 and Parkin. FBXO7 appears to be one of them, since it is required for the translocation of Parkin to depolarized mitochondria by acting as a scaffold protein for the interaction between PINK1 and Parkin **(Fig. 1.4 B)** (Burchell et al., 2013). As mentioned previously, this interaction can be mapped to the N-terminus of FBXO7 and more specifically to the Ubiquitin-like (Ubl) domain for Parkin and the interaction with PINK1 spans not only the Ubl domain but the whole stretch up to the CDK6 binding domain (Burchell et al., 2013). The involvement of FBXO7 in mitochondrial quality control was further substantiated by two independently working groups, where the pathological mutants of *Fbxo7* were shown to aggregate in mitochondria, inhibit mitophagy, lead to increased generation of ROS at expense of decreased $\Delta\Psi$m and ATP production (Delgado-Camprubi et al., 2017; Zhou et al., 2015).

1.4. The Cytoskeleton: stability and dynamics

Microtubules (MTs) play paramount role in cellular architecture, motility, division and organellar transport (Mandelkow and Mandelkow, 1995). Since neurons have highly polarized morphology that is required for their function in signal transmission, microtubule dynamics and stabilization is of particular importance (Benitez-King et al., 2004). Furthermore, during synaptogenesis in embryonic development and plasticity, extracellular cues guide the growth cone through the intercellular space until it reaches its target, ensuring the correct connectivity pattern (Mattson et al., 1988). This axon guidance and motility is achieved because of the dynamic nature of microtubules (Gonzalez-Billault et al., 2001).

Microtubules are assembled through the polymerization of α and β tubulin homodimers into heterodimers and protofilaments, where 13 protofilaments form a hollow cylinder **(Fig. 1.5)** (Mohri, 1968). The heterodimers always polymerize such that the α-tubulin subunit binds to the β-tubulin subunit of another heterodimer, rendering the microtubules themselves as polar structures with a slow-growing minus end and a fast growing plus end **(Fig. 1.5)** (Benitez-King et al., 2004). Therefore, the dynamic equilibrium between the rate of assembly and disassembly establishes the directionality and growth of neurites (Benitez-King et al., 2004). Whenever necessary, this process of polymerization-depolymerization together with microtubular nucleation can be controlled with the help of microtubule-binding proteins **(Fig. 1.5)** (Benitez-King et al., 2004; Mandelkow and Mandelkow, 1995). Furthermore, they facilitate the formation of higher order microtubular structures such as axonemes, centrioles and axonal bundle formation **(Fig. 1.5)** (Ikegami and Setou, 2010).

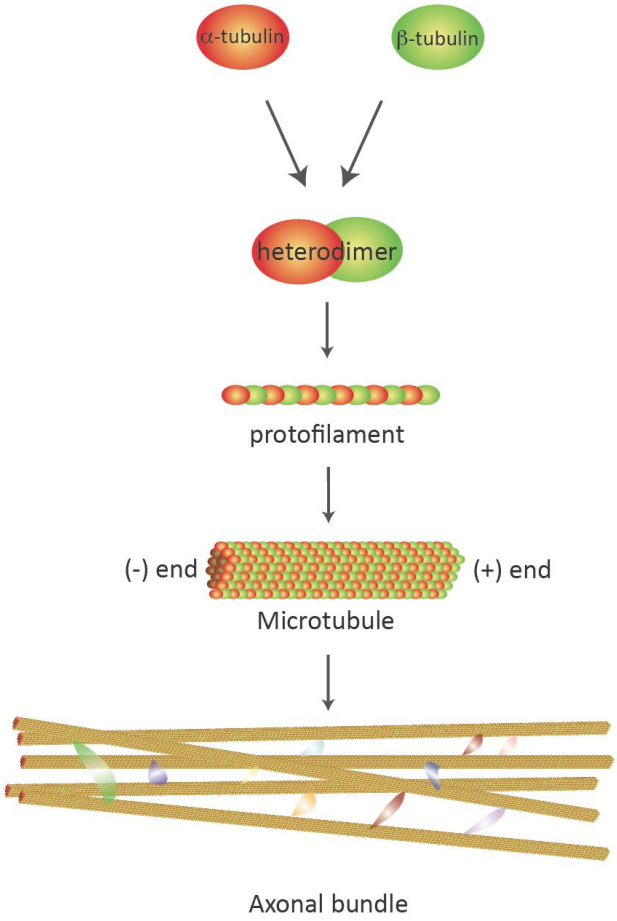

Fig. 1.5 Microtubules: from monomers to complex structures

α- and β-tubulin monomers form heterodimer complexes, which further grow into protofilaments. The protofilaments assemble into hollow cylinders known as microtubules (MTs). The MTs are polar structures, which then can assemble into complex cytoskeletal formations such as axonal bundles with the help of microtubular associated proteins (MAPs), depicted as brightly colored structures.

1.4.1. The MAP1B family

Microtubule associated proteins (MAPs) bind to microtubules and stabilize them **(Fig. 1.5)** (Mandelkow and Mandelkow, 1995). MAP1B is one of the earliest expressed MAPs in the brain and its expression drops drastically towards the end of neurogenesis (Tucker et al., 1989). This drop in expression is then matched by an increase of expression of the MAP1A complex (Binder et al., 1984). While MAP1A and MAP1B are predominantly expressed in neurons, MAP1S is the only member of the MAP1 family that is ubiquitously expressed in almost all tissues (Orban-Nemeth et al., 2005). The expression of MAP1B is highly regulated so that it coincides with the commence of neurite outgrowth and can be found in both axonal and dendritic processes highlighting its role in

neuritogenesis (Bloom et al., 1985; Riederer et al., 1986). The knockout of *Map1b* in mice leads to the complete absence of the corpus callosum, additionally establishing MAP1B as a major factor in axonal outgrowth during synaptogenesis (Meixner et al., 2000).

The MAP1B transcript encodes a polyprotein that is post-translationally cleaved into heavy chain (HC) and light chain, known as LC1 (Hammarback et al., 1991). The HC and the LC then associate back together in a non-covalently bound manner and in a stoichiometric ratio of 1:2 respectively to form the MAP1B protein (Hammarback et al., 1991). MAP1B LC1 is thought to mediate the interaction between the HC and MTs, since it contains MT binding domain (Togel et al., 1998a). Further analysis revealed that MAP1B LC1 is the active subunit, required for microtubular stabilization, where the HC most likely acts as regulatory particle by reducing the LC1's binding capacity to MTs (Diaz-Nido et al., 1990; Togel et al., 1998b). Intriguingly, MAP1B is highly phosophorylated protein, and the binding affinity to MT is regulated by the degree of phosphorylation, suggesting that this type of post-translational modification may inflict conformational change in the MAP1B complex, liberating the LC1 and thus allowing it to stabilize MTs (Diaz-Nido et al., 1990; Togel et al., 1998b). Functionally, MAP1B LC1 induces tubulin polymerization and because of its expression in early development, it plays an important role in axonal growth and elongation, where knocking-out of the *Map1B* resulted in shorter axons in cultured neurons (Gonzalez-Billault et al., 2001; Gonzalez-Billault et al., 2002; Noiges et al., 2002).

1.4.2. The role of MAP1B LC1 in microtubular transport

Another important function of microtubules is to provide a structural track for organellar transport (Mandelkow and Mandelkow, 1995). As previously noted, MTs are polarized structures, and in axons, there is very strict directionality, where the minus end is facing the soma, and the positive end faces the synapse (Baas and Black, 1990). A second type of MAPs facilitate the transport of organelles along the axon, depending on cellular demand (Mandelkow and Mandelkow, 1995). Kinesins are responsible for plus-end transport, and dyneins traffic organelles towards the minus-end (Mandelkow and Mandelkow, 1995; Schnapp and Reese, 1989; Schnapp et al., 1992). Although the MAP1B has a distinct function in axonal growth by regulating MT dynamics, it was also recently found to limit retrograde transport of mitochondria along the axon when overexpressed (Jimenez-Mateos et al., 2006). This implicates that overstabilization and overabundance of MAP1B can in turn cause blockage of binding sites for motor proteins, reducing the capacity of cells to shuttle cargo from the synaptic termini back to the soma (Jimenez-Mateos et al., 2006).

1.4.3. The Mitochondria-UPS relationship in neurodegenerative disorders

Mitochondria are the power plants of the cell. Just like fossil-fueled reactors, they convert energy stored in the strong covalent bonds in organic molecules into electric potential (Brookes et al., 2004). This process is termed oxidative phosphorylation because the potential is then further utilized for the phosphorylation of adenosine diphosphate (ADP) into ATP at the expense of oxidizing nutrients (Brookes et al., 2004). This process requires a series of reduction and oxidation reactions, where the final outcome is reducing oxygen into water (Brookes et al., 2004). The fundamental need and benefits of producing energy, however does not come without costs: oxidative phosphorylation generates highly reactive oxygen radicals such as peroxide and superoxide, commonly referred as reactive oxygen species (ROS) (Sena and Chandel, 2012). Cells and mitochondria are equipped with a battery of mechanisms to fend off ROS and to try and repair or degrade proteins, DNA or lipids that have been damaged by ROS as discussed in **Section 1.3.3**. If one of these lines of defense fails due to genetic or environmental reasons, the balance of the system is thrown off, ultimately leading to cellular collapse **(Fig. 1.6)**. The disruptive relationship between mitochondria and the UPS can be reciprocal: aberrations in mitochondria lead not only to a decrease in ATP production necessary for the UPS to function, but also to increase in the number of damaged and misfolded proteins, overwhelming the UPS **(Fig. 1.6)** (Nakamura and Lipton, 2009). Conversely, pathological protein accumulations causing UPS strain or intrinsic aberrations in the UPS can lead to failure in maintaining healthy mitochondrial proteostasis followed by mitochondrial dismay and triggering an increase in ROS production **(Fig. 1.6)** (Branco et al., 2010). These two processes then enter a cycle of fueling each other's detrimental effects **(Fig. 1.6)**.

Neurons are particularly sensitive to oxidative stress because of the high-energy demands required for the action potential propagation and the maintenance of the resting membrane potential (Chang and Reynolds, 2006). Furthermore, the "power plants" are frequently located at the synapse- the most energy-demanding and Ca^{2+} rich location, since cellular calcium levels are buffered by mitochondria (Chang et al., 2006a; Friedman and Nunnari, 2014; Morris and Hollenbeck, 1993). Aberrant mitochondria located at the synapse and are destined for repair need to be transported back to the soma, in order to fuse with the lysosomes (Friedman and Nunnari, 2014). Blocking the retrograde axonal transport can lead to aggregation of damaged mitochondria leading to the domino effect of the dysfunctional mitochondria-UPS relationship **(Fig. 1.6)** (Friedman and Nunnari, 2014; Jimenez-Mateos et al., 2006).

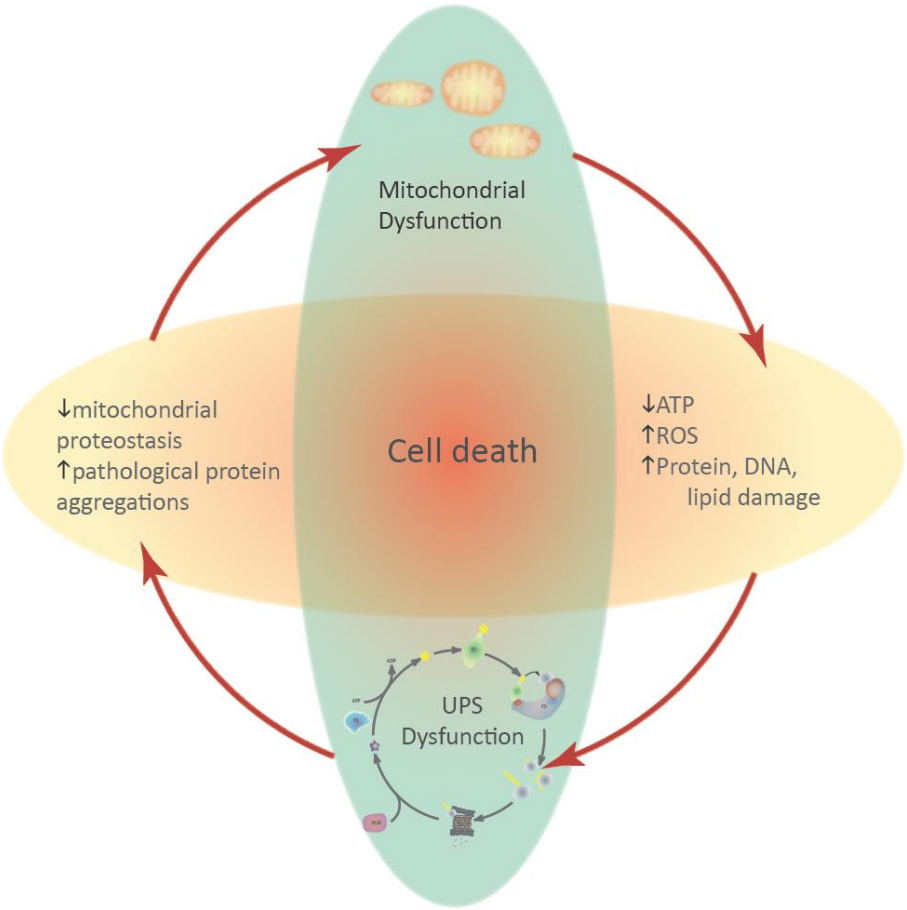

Fig. 1.6 Neuropathological relationship between mitochondria and the UPS

Aberrant mitochondria lead to decreased adenosine triphosphate (ATP) production accompanied by the increase in the reactive oxygen species (ROS) generation and protein, DNA and lipid damage. This in turn may stress the ubiquitin proteasome system (UPS), reducing its capability to degrade damaged proteins, causing protein aggregations and accumulation. Failure in the UPS to clear out misfolded and damaged mitochondrial proteins results in mitochondrial dysfunction, closing off the cycle. The perpetuation of these processes can eventually lead to cellular death.

1.5. Aim of the study

In this study, I applied different biochemical and genetic techniques to examine the role of the parkinsonism-associated protein FBXO7 in cells in culture as well as neurons *in vivo.* FBXO7 is involved in multiple pathways, and in my investigation of the functional analysis of FBXO7, I focused on how loss-of-function of *Fbxo7* affects mitochondrial health and neuronal morphology. I also evaluated the consequences of knocking-out *Fbxo7* in the forebrain, and saw a generalized response following brain damage, highlighting the importance of FBXO7 in neuronal health.

2. Materials and Methods

2.1. Materials

2.1.1. Laboratory Equipment

The experiments were carried out using the following Laboratory Equipment: **micropipettes**: Gilson, USA; **consumables and plastic ware**: Eppendorf, Hamburg, Germany; Thermo Fisher Scientific, Waltham, USA; Sarstedt AG & Co, Germany; Falcon BD, Le Pont de Claix, France; Greiner Bio-One, Frickenhausen, Germany; Croning|Sigma Aldrich, Munich, Germany; **Tabletop Centrifuges**: Eppendorf, Hamburg, Germany/ Thermoscientific, Waltham, USA; **Heating blocks**: Grant Instruments, UK; **Thermoshaker**: Biometra, Jena, Germany; **Rocker and Shaker**: Heidolph, Germany; **Spectrophotometer**: Amersham Biosciences, UK/ TECAN Infinite M200, Männedorf, Switzerland; **UV Transilluminator**: Intas, Germany; **Chemiluminescence Documentation System Alliance**: Biometra, Jena, Germany; **Thermocycler:** Biometra, Jena, Germany; **Dissection Microscope**: SMZ645, Nikon, Japan; **Brightfield Light Microscope**: Zeiss Axiophot, Oberkochen, Germany; **Fluorescent Microscopes**: Eclipse TI, Nikon, Japan/ Olympus BX51, Japan; **Inverted Light Microscope**: Eclipse TS100 Nikon, Japan/ Olympus CKX 41, Japan; **Embedding Tissue Processor:** HMP 110, MICROM; **Microtome:** HM 430, Thermo Fisher Scientific; **Waterheating basin:** HIR-3, Kunz Instruments.

2.1.2. Reagents, Chemicals and Kits

All the reagents and chemicals used in this study (unless otherwise indicated) were purchased from Applichem (Darmstadt, Germany), Biomol (Hamburg, Germany), Bio-Rad Laboratories (Hercules, USA), DAKO North America, Inc. (Carpinteria, USA), GE Health Care (New Jersey, USA), Invitrogen (Darmstadt, Germany), Merk (Darmstadt, Germany), New England BioLabs (Frankfurt, Germany), Promega (Fitchburg, USA), Roth (Karlsruhe, Germany), Sigma-Aldrich (Munich, Germany), Thermo Fisher Scientific (Massachusetts, USA) and Worthington (Lakewood, USA).

All media and supplements for used for primary and immortalized cell culture were purchased from GIBCO®|Thermo Fisher Scientific (Massachusetts, USA).

The Commercially available kits used for DNA extraction and purification - Nucleobond Xtra Midi EF, NudeoSpin Plasmid QuickPure and Nucleospin Gel and PCR Clean-up kit were purchased from Macherey-Nagel (Düren, Germany).

DNA and Protein ladders were supplied by Fermentas|Thermo Fisher Scientific (Massachusetts, USA).

Mounting solution for immunohistochemistry was obtained from Eukitt (Freiburg, Germany). The paraffin used for embedding the brain tissue was produced by Paraplast, Leica (Wetzlar, Germany).

2.1.3. Antibodies

List of the primary and secondary Antibodies used in this study is summarized in **Table 2.1** and **Table 2.2**:

Table 2.1 Primary Antibodies used and their specifications

Primary Antibody	Application	Dilution	Host	Source	Type
14-3-3β	WB	1:5000	mouse	Santa Cruz	monodonal
α-synudein	IHC	1:200	rabbit	Invitrogen	monodonal
β-galactosidase	ICC	1:1000	mouse	Santa Cruz	monodonal
APP	IHC	1:100	mouse	Thermo Fisher Scientific	monodonal
Myc	WB ICC	1:1000 1:1000	mouse	Santa Cruz	monodonal
FLAG	WB ICC	1:1000 1:1000	mouse	Santa Cruz	monodonal
GFP	WB ICC	1:1000 1:1000	mouse rabbit	Santa Cruz Invitrogen	monodonal
HA	WB	1:500	mouse	Santa Cruz	monodonal
GFAP	IHC	1:200	mouse	Nova Castra	monodonal
Iba1	IHC	1:1000	mouse	WAKO	monodonal
MAP1B LC1	ICC IHC	1:500 1:200, 1:500	mouse	Santa Cruz	monodonal
NFM	IHC	1:500	mouse	Santa Cruz	monodonal

cullin1	WB	1:50	mouse	Santa Cruz	monoclonal
FBXO7	WB	1:500	mouse	Santa Cruz	monoclonal
MAP2	ICC	1:1000	mouse	Santa Cruz	monoclonal

Table 2.2 Secondary Antibodies used in this study

Secondary Antibody	Conjugated probe	Application	Dilution	Host	Supplier
α-mouse IgG	HRP	WB	1:10000	goat	Dianova
α-mouse IgG	Cy2	ICC	1:1000	goat	Dianova
α-rabbit IgG	Cy2	ICC	1:1000	goat	Dianova
α-mouse IgG	Cy3	ICC	1:1000	goat	Dianova
α-rabbit IgG	Cy3	ICC	1:1000	goat	Dianova

2.1.4. Enzymes

All enzymes used in this study are listed in **Table 2.3**

Table 2.3 List of Enzymes used

Enzyme	Supplier
Restriction Enzymes	New England Biolabs
GoTaq DNA Polymerase	Promega
Pfu DNA polymerase	Thermo Fisher Scientific
T4 DNA Ligase	Thermo Fisher Scientific
Proteinase K	AppliChem
DNase I	Roche
Alkaline Calf Intestinal Phosphatase	New England Biolabs

2.1.5. Solutions, Media and Buffers

The solutions, media and buffers used in this study are listed in **Table 2.4.**

Table 2.4 List and recipes for all buffers and solutions used in this study

	Buffer/Solution	Chemicals and Media used	pH
Media for immortalized cell lines	Enriched DMEM for HEK 293T cells	DMEM [+] 4.5 g/L glucose, [-] glutamine, [-] pyruvate, 10% heat inactivated calf serum (HyClone), 1% GlutaMAX®	7.4
	Medium for SH-SY5Y cells	45% DMEM [+] 4.5 g/L glucose, [-] glutamine, [-] pyruvate, 45% F12 Nutrient Mixture [+] GlutaMAX, 10% heat inactivated calf serum (HyClone)	7.4
	Trypsin	0.05% Trypsin- EDTA in 1XHBSS (from 10X stock Gibco®)	7.4
Transfection buffers	2XHBSS	50 mM HEPES, 280 mM NaCl, 10 mM KCl, 15 mM glucose, 1.5 mM Na_2HPO_4	7.05-7.11
	$CaCl_2$	2.5 M $CaCl_2$ in H_2O	-
Media for primary cortical culture	HHGN	1X HBSS (from 10X stock Gibco®), 2.5 mM HEPES, 35 mM glucose, 4 mM $NaHCO_3$	7.4
	TDn	50 mg Trypsin (Worthington), 250 µL DNase (stock 2 µg/µL), 5mL HHGN	7.4
	Plating Medium	Neurobasal® [-] L-glutamine, 1% PSG, 2% B27 supplement	7.4
Biochemistry	Triton® X-100 lysis buffer	150 mM NaCl, 50 mM Tris-HCl, 1 mM EDTA, 1% Triton® X-100	7.4
	Co-IP buffer	150 mM NaCl, 20 mM Tris-HCl, 1 mM EDTA, 1% Nonidet P-40, 10% Glycerol	7.4
	RIPA Buffer	150 mM NaCl, 5 mM Tris-HCl, 1 mM EDTA, 1% Nonidet P-40, 0.5% sodium deoxycolate, 0.1 % SDS	-
	Ubiquitination Assay Lysis Buffer	150 mM NaCl, 50 mM HEPES, 1.5 mM $MgCl_2$, 1% Triton® X-100, 10% Glycerol	-
	4X SDS Sample buffer	300 mM Tris- HCl pH 6.8, 10 % SDS, 50% Glycerol, 25% β-mercaptoethanol, bromophenol blue	-

Table 2.4 List and recipes for all buffers and solutions used in this study (Continued)

Blotting Buffers	Lower Buffer	1.5 M Tris- HCl, 0.4% SDS	8.8
	Upper Buffer	0.5 M Tris- HCl, 0.4% SDS	6.8
	Running Buffer	125 mM Tris, 1.25 M glycine, 0.5% SDS	-
	Transfer Buffer	20 mM Tris, 153 mM glycine, 20% Methanol	-
	10X PBS	1.37 M NaCl, 14.7 mM KCl, 78.1 mM Na_2HPO_4, 26.8 mM KH_2PO_4	7.3-7.4
	PBS-T	1X PBS, 0.1% Tween-20	7.3-7.4
	Primary Antibody Blocking Solution	3% BSA w/v, 0.02% NaN_3 in 1X PBS	7.3-7.4
Genotyping	Tail Lysis Buffer	10 mM Tris, 200 mM NaCl, 10 mM EDTA, 0.5% SDS	8.0
Anesthetics	Ketamine/Xylazine	10% Ketamine v/v (10% Medistar, Arzneimittelvertrieb GmbH; 5 % Xylazine (2% Xylazine, CP Pharma ®)	-
Immunohistochemistry	0.2 M Phosphate Fixation Buffer	0.36% w/v NaH_2PO_4, 3.1% w/v Na_2HPO_4, 1% w/v NaCl	~7.4
	4% PFA for paraffin embedding	4% w/v PFA, 0.1 M phosphate fixation buffer	-
	Citrate Buffer	1.8 mM $C_6H_8O_7 \bullet H_2O$, 8.2 mM $C_6H_5Na_3O_7 \bullet 2H_20$	6.0
	Tris Buffer	0.9% w/v NaCl, 50 mM Tris-Cl	7.6
	BSA/PBS	0.04 M NaH_2PO_4, 0.16 M Na_2HPO_4, 1.8% w/v NaCl, 1% w/v BSA	-
	Proteinase K digestion buffer	10 mM Tris- HCl, 100 mM NaCl, 0.1% NP40	7.4
	Blocking Buffer	20% Goat Serum v/v in BSA/PBS	-
	Scott's reagent	ready to use	-

Table 2.4 List and recipes for all buffers and solutions used in this study (Continued)

	Haematoxylin	ready to use	-
	HCl-Alcohol	0.09% v/v HCl, 70% v/v Ethanol	-
Immunocytochemistry	8% PFA	40 g PFA, 50 mL 10X PBS, 40 g Sucrose in final volume of 500 mL sterile H_20	7.4
	0.04% Tx-100 Permeabilization Buffer	0.4% Tx-100 v/v in PBS	7.4
	BME Blocking Buffer	10% heat inactivated Goat/Horse serum in BME [+] Earle's salts [-] L-glutamine	-
	DAPI	1 μg/μL stock, dilution 1:8000 in ddH_2O	-
	Mowiol Mounting Media	6 g 85% Glycerol, 2.4 g Mowiol 4-88, 6 mL H_2O, 12 mL Tris-HCl, 2.5% $C_6H_{12}N_2$/DABCO®	8.5
Molecular cloning buffers and media	Annealing Buffer	1 M Tris- HCl, 2 M KCl	7.5
	2X TAE	80 mM Tris-Acetate, 2 mM EDTA	8.5
	2X YT medium	5 g NaCl, 16 g tryptone, 10 g yeast extract in 1 L ddH_2O	-
	2X YT agar plates	1.5% agar, 50 μg/mL Ampicillin/Kanamycin	-
	LB broth	20 g LB in 1 L sterile H_2O	-
	LB agar plates	32 mg LB agar in 1 L sterile H_2O	-

2.2. Methods

2.2.1. Molecular cloning

i. Molecular cloning of the MAP1S LC expression plasmids

Cloning of the MAP1S LC cDNA in pCMV10-3xFLAG expression vector, required primers, designed to target the gene of interest and be unique for that sequence. The primers chosen have the following nucleotide sequence:

Forward primer: 5'- ATAAAGCTTATGGTGGACCCGGAGGCGCTA - 3'

Reverse primer: 5'- CTCGTCGACCTAGAACTCCACCTTGCAGGCC - 3'

Since each primer has a unique melting temperature (Tm), they were also so designed as to have similar Tm, which then served as guidelines for the annealing temperature for the primers, set to be 5°C below the Tm. The elongation step was also estimated, taking under consideration the elongation rate of the Pfu polymerase of 500bp/min. The reagent mixture settings are mentioned in **Table 2.5**:

Table 2.5 Reagent mixture settings

Reagent	Volume (μL)
Template DNA (50 ng)	0.5-1
Forward and reverse primers (10 pmol/μL)	1
dNTP (25 mM)	0.4
Pfu DNA Polymerase	0.5
10x Pfu polymerase reaction buffer	5
Total reaction Volume	50

This reaction mixture was then subjected to amplification by a polymerase chain reaction (PCR) following the protocol form Saiki *et al.,* with modifications to achieve exponential multiplication of the desired product (Saiki et al., 1985). The PCR settings for molecular cloning of the MAP1S LC were set as in **Table 2.6:**

Table 2.6 PCR settings for molecular cloning of the MAPS1S LC

Process	Temperature (°C)	Duration (min)	
Initial denaturation	95	3	
PCR denaturation	95	0.5	30 cycles
Primer annealing	57	0.5	
Elongation	72	2	
Final elongation	72	10	

The resulting PCR product was then ran through 1% agarose gel electrophoresis and the bands corresponding to the correct insert size were excised and purified using Nudeospin Gel and PCR Clean-up kit following manufacturer's instructions. The PCR product was then eluted in 60 μL ddH_2O and digested for 2 hours and 37°C using 2 μL of the HindIII and SalI restriction enzymes (final reaction volume 60 μL) corresponding to the cutting sites on the designed primers and the vector's multiple cloning site. 3 μg of the pCMV10-3xFLAG vector was also digested and then dephosphorylated using CIP for 1 hour at 37°C. Next, both the vector and the insert from the digestion reactions were purified and eluted using Nudeospin Gel and PCR Clean-up kit (Macherey-Nagel) according to manufacturer's instructions in 15 μL and 50 μL ddH_2O respectively.

The purified products were used to set up a ligation reaction as listed in **Table 2.7**:

Table 2.7 Ligation reaction settings

Reagent	Volume (μL)
Dephosphorylated pCMV10 vector	1
Insert	3.5
ATP (10 mM)	0.6
10x T4 ligation buffer	0.9
T4 DNA ligase	1
Final volume	10

The ligation reaction was left overnight in icy water, to gradually increase the temperature to RT.

ii. Bacterial transformation, inoculation and plasmid verification

The ligation reaction was used to transform DH5α *E. coli* bacteria by incubating the whole reaction mixture with 10 μL of the highly competent bacteria for 30 min on ice. Next, the bacteria were heat- shocked for 2 min at 37°C, placed back on ice. 300 μL of the 2x YT medium was added to the tube, and the cells were allowed to grow for 30 min at 37°C. The cells were then spun down at 4000 rpm for 3 min, approximately 300 μL of the supernatant was removed and the cells were resuspended in the remaining supernatant and plated onto ampicillin agar plate.

Colonies were picked and inoculated in 2 mL of the 2x YT medium containing ampicillin (1:1000) overnight. The DNA was extracted using the NucleoSpin Plasmid QuickPure (Macherey-Nagel), and the purified DNA from 10 colonies was tested for the presence of the insert through restriction test digest. To finalize the cloning process, samples from positive clones were sent for sequencing by the AGTC Lab at the Max Planck Institute of Experimental Medicine, Göttingen.

iii. Molecular cloning of vector-based RNA interference oligonucleotides

The MAP1B LC1 shRNAs were designed to target the protein expression in human, mouse and rat. The sense shRNA sequence was homologous to a targeted mRNA region (highlighted in red) on the MAP1B LC1, followed by a 9-nucleotide loop and then the antisense sequence:

5'-GGCCTCCCTGTGTATTTGGAAAGTTAACGTCCAAATACACAGGGAGGCC -3'

For the **annealing** of the primers, 2 µL of each oligonucleotide (50 pmol/µL) were incubated first for 5 min at 95°C, then 10 min at 72°C in 46 µL annealing buffer, and then the reaction mixture was allowed to cool down at rate of 0.1°C/sec. Next 20 µL of the annealed oligonucleotides were phosphorylated for 30 min at 37°C using reaction mixture in **Table 2.8**:

Table 2.8 Reaction mixture for annealing of the primers

Reagent	Volume (µL)
Annealed oligonucleotides	20
10x PNK buffer	5
PNK	1
ATP (10 mM)	0.5
Final volume	50

Next, 4 µL of the phosphorylated oligonucleotides were ligated with 1µL of the pre-digested (Bgl II and Hind III) and pre-dephosphorylated pSuper vector as described previously in **Section 2.2.1.i**. Next, the ligation reaction was used to transform SURE bacteria following the DH5α bacterial transformation protocol **(Section 2.2.1.ii)**, except the volume of bacteria used was 100 µL. The bacteria were plated and subsequently inoculated as described earlier, and a test digest using HpaI (specifically cutting through the 9 bp loop sequence) was used to identify the positive clones.

2.2.2. Immortalized cell lines maintenance and transfection

All cell cultures were maintained in HERAsafe® or alternatively HERAcell 150i (Thermo Fisher Scientific) under sterile conditions at 37°C and 5% CO_2. Propagation, maintenance and transfection of all cell lines were carried out under a sterile biological safety hood HERAsafe® (Thermo Fisher Scientific).

i. HEK 293T cells passaging:

HEK 293T cells were grown in enriched DMEM at 37°C and 5% CO_2. At about 100% confluency, the HEK 293T cells were regularly passaged by washing them with 4-5 mL sterile PBS and then trypsinizing them with 2 mL trypsin-EDTA for no longer than 2 minutes at 37°C. Trypsinization was stopped using 8 mL enriched DMEM and the detached cells were collected in a 15 mL FALCON tube and spun at 4°C for 5 min at 800 rpm. The medium was aspirated and the cell pellet was carefully resuspended in 9 mL of fresh enriched DMEM. The cells were then seeded in 10 cm cell culture dishes in dilution 1:10 for further passaging. For biochemical experimental procedures, 200 µL of the cell resuspension was seeded in 2 mL enriched DMEM in 6-well plates or alternatively, 20 µL of the cell resuspension was seeded onto poly-ornithine coated glass slides in 500 µL enriched DMEM in a 24-cell plate.

ii. HEK 293T cell transfection:

Once reaching confluency of 60-80%, the HEK 293T cells were transfected following a modified version of the Calcium Phosphate Transfection protocol (Konishi et al., 2004). Briefly, 90 µL of ddH_20 containing the desired amount of plasmid was mixed with10 µL 2.5 M $CaCl_2$. To this solution, 100 µL 2xHBSS (pH 7.08-7.11) was pipetted in by introducing bubbles during the mixing. The DNA was allowed to precipitate for 5 minutes at RT, and the final volume of 200 µL was added dropwise to the cells in the 6-well plate.

HEK 293T cells seeded in 24-well plates were transfected using the same method, but with final volume of DNA in ddH_2O of 20 µL, mixed with 2 µL 2.5 M $CaCl_2$ and 20 µL 2xHBSS (pH 7.08-7.11).

iii. SH-SY5Y cells passaging:

The SH-SY5Y cells were grown and maintained in Enriched DMEM/F12 medium at 37°C and 5% CO_2. The medium was regularly exchanged every 3-4 days. The cells were passaged after reaching confluence of about 80% by washing them with sterile PBS followed by trypsinization for no more than 1 min. The cells were then collected in 8 mL DMEM/F12 medium and spun down for 3 min at 300 rpm and 4°C. The supernatant was discarded and the SH-SY5Y cells were then

resuspended in 5 mL DMEM/F12. The cell count was determined using haemocytometer and the cells were seeded as needed in 24-well plates (60 000- 100 000 cells) onto 12 mm coverslips, previously incubated for minimum 30 min at 37 °C with poly-ornithine and then washed with ddH_2O.

iv. SH-SY5Y transfection:

The SH-SY5Y cells were transfected using Lipofectamine 2000 following the manufacturer instructions and adapting them for maximal efficacy. Briefly, 2 μL of Lipofectamine diluted in 50 μL GIBCO® Opti-MEM™ (Thermo Fisher Scientific) was carefully mixed with 50 μL GIBCO® Opti-MEM™ containing the required plasmid dilute. The lipofectamine and DNA mixture was then incubated for 10 min, to ensure DNA entrapment into the lipid droplets, and then it was added dropwise to the cells. The medium was exchanged within 6-18 hours with warm DMEM/F12.

2.2.3. Primary cortical cell culture generation, maintenance and transfection

Primary cell cultures were maintained in HERAsafe® or alternatively HERAcell 150i (Thermo Fisher Scientific) under sterile conditions at 37°C and 5% CO_2. Generation, maintenance and transfection were carried out under a sterile biological safety hood HERAsafe® (Thermo Fisher Scientific).

i. Primary cortical culture generation

P0-P2 C57BL/6N pups were decapitated and the brains were isolated in cold 1xHBSS medium. The cortices were dissected out, ensuring that the meninges, the midbrain, hippocampus, and olfactory bulbs were removed. All of the following steps were performed in sterile conditions. The cortices were washed three times in cold 1xHBSS, and the neurons were dissociated in TDn for 10-15 min at 37°C and 5% CO_2. Washing the cortices again with 1xHBSS terminated the trypsin digestion. To completely dissociate the neurons, a 10 mL serological pipette was used to triturate the cells in 5 mL plating medium containing freshly added DNase (2 mg/mL). The cell suspension was then centrifuged at 800 rpm for 7.5 min at 4°C. Next, the supernatant containing cellular debris was aspirated off, and the remaining pellet was once more resuspended in 10 mL of cold plating medium. The cells were counted and plated at desired density (0.75-1.2 x10^6) in a final volume of 500 μL onto 12 mm poly-ornithine coated cover slips in 24-well plates. Neuronal cultures kept for longer than DIV6, were supplied with 15 μL 1M glucose.

ii. Primary cortical culture transfection

The cortical neurons were transfected using calcium chloride at either DIV1 for axonal length analysis or at DIV3 for all other experiments. The conditioned plating medium was collected and the cells were washed three times with warm DMEM ([+] 4.5 g/L glucose, [-] glutamine, [-] pyruvate). The cells were then left to starve in glucose free 0.5 mL DMEM at 37°C and 5% CO_2 for 45-60 min. Meanwhile, the required DNA concentration was diluted in ddH_2O for a final volume of 18 μL. 2 μL $CaCl_2$ was then pipetted into the mixture, and finally 20 μL 2xHBSS of optimal pH (7.08-7.11) was added, by introducing bubbles. The final solution was incubated for 8 min at RT, and was then added drop-wise to the neuronal culture and incubated for 18 min at 37°C and 5% CO_2. Finally, the DNA/$CaCl_2$ mixture was washed away thoroughly with DMEM ([+] 4.5 g/L glucose, [-] glutamine, [-] pyruvate) and the neurons were allowed to incubate further in the original plating medium.

2.2.4. Immunocytochemistry

Cells were fixed by washing them twice with PBS and then incubating them in 4% PFA in PBS for 10 minutes. The PFA was washed 2-3 times using PBS and then the cellular membranes were permeabilized with 0.4% Triton X-100 in PBS [v/v] for 10 min at RT and then washed again with PBS. The cells were then blocked for minimum of 30 min at RT with 10% horse serum (HS) in BME, and the cover slips were transferred onto a wet, light-impermeable chamber. Next, 50 μL of the primary antibody diluted in 10% HS in BME was added to the sides and incubated according to the optimized results. The primary antibody was washed using the HS in BME. Secondary antibody also diluted in 50 μL HS in BME was incubated for 45-60 min and washed with PBS. Optionally, the cellular nuclei were stained with DAPI for 8 min at RT, and washed with PBS. Lastly, the cover slips were mounted onto microscope slides (Marienfeld, Germany) using Mowiol.

2.2.5. Axonal and total dendritic length analysis

The cultured neurons were transfected at DIV 1 as described in **Section 2.2.3.ii** with the plasmid of interest together with c1-GFP plasmid serving as transfection marker and the anti-apoptosis protein Bcl-xL. Immunocytochemistry was performed at DIV6, and the transfected neurons were visualized under an epifluorescent microscope (Eclipse TI, Nikon). Next, 40-60 transfected neurons per condition with healthy nuclei were imaged (NIS- Elements Basic Research, Nikon Instruments) and the axonal and the dendritic lengths were determined using the ImageJ macro plug NeuronJ (NIH).

2.2.6. Biochemical Methods

i. Cell lysis

The HEK 293T or the SH-SY5Y cells were washed with cold PBS to ensure the removal of any dead cells. Next, 200 µL of cold Triton® X-100 lysis buffer or co-immunoprecipitation buffer containing 3 µg/mL Aprotinin, 1 µg/µL Leupeptin and 1 µg/µL Pepstatin protease inhibitors together with 1 mM 1,4-dithiothreitol (DTT) as reducing agent were pipetted into the 6-well plates. The cells were then scraped off the surface of the plates using cell scraper (Greiner Bio-One|VWR), collected and incubated 30 min on ice. The lysates were then spun down at 14 000 rpm for 10 min at 4°C. The supernatant was used for further analysis and the pellet was discarded.

ii. Protein concentration determination

Protein concentration was determined using the Bio-Rad® Protein Assay based on the Bradford Method (Bradford, 1976). Briefly, the reagent was diluted 1:5 in cold PBS and 1 mL of the diluted reagent was pipetted into disposable spectrophotometer cuvettes (Greiner Bio-One|VWR). 2 µL of the lysate was pipetted into the cuvettes and the mixture was thoroughly vortexed to ensure even distribution of the proteins. Next, the absorbance at wavelength 595 nm was determined using spectrophotometer. Furthermore, a standard curve was generated by measuring the absorbances corresponding to 5, 10 and 15 µg/ml BSA in the diluted Bradford reagent, and the resulting correlation curve was used to calculate the relative lysate concentration.

Alternatively, the concentration was determined using a modified version of the Lowry Protein assay (Lowry et al., 1951). 24.5 µL of Reagent A was mixed with 0.5 µL of reagent S (DC™ Protein Assay, BioRad, USA). The mixed reagents were then pipetted into 96-well Nunclon Delta surface plate (NUNC|Thermo Fisher Scientific, Denmark). 5 µL of 0.0, 0.2, 0.5, 0.8, 1.2 and 1.2 µg of BSA diluted in the same buffer as the samples (necessary for generation of the standard curve) as well as 5 µL of the samples was pipetted into the Reagent A+S. Finally, 200 µL of the Folin–Ciocalteu reagent was added and the reaction was allowed to develop over 15 min at 26°C with initial 5 seconds shaking. The absorbance at 750 nm was measured using the TECAN Infinite M200 and analyzed by the i-control 1.8 SPI software.

iii. Co-immunoprecipitation

After protein determination, 0.75-1.5 mg of protein was pipetted into a 1.5 mL tube and the final volume was equalized for all samples using co-immunoprecipitation buffer. 50 µg of protein from the total cell lysate was boiled in 4xSDS Sample buffer for 5 min at 95°C to serve as

input control. The optimized amount of primary antibody was added to the lysates and allowed to incubate rotating for 2-4 hours at 4°C according to on the antibody specifications. 15-20 μL of Protein A Sepharose beads slurry (Protein A Sepharose™ Fast Flow, GE Healthcare, UK), previously washed with co-immunoprecipitation buffer with final dilution 1:1, were added to the lysates. After 1 hour incubation at 4°C on the roller mixer, the beads were collected at the bottom of the tube (10 000 rpm, 1 min at RT), and washed 2-3 times either with 200-300 μL of the Triton® X-100 lysis buffer or the RIPA buffer followed by 300 μL PBS wash. Finally, approximately 30 μL of 4xSDS Sample buffer was pipetted and mixed into the beads followed by a 5 min denaturating step at 95°C.

iv. Ubiquitination assay/ Interaction strength assay

The cell-based ubiquitination assay was performed following a modified version of the methods described in Lu *et al*. (Lu et al., 2007). The transfected HEK 293T cells were washed with cold PBS and lysed in 200 μL RIPA (without SDS) supplemented freshly with 3 μg/mL Aprotinin, 1 μg/μL Leupeptin, 1 μg/μL Pepstatin as well as 10 mM N-ethylmaleimide (NEM) serving as a deubiquitinase inhibitor (addition of NEM was omitted for the mutant interaction strength analysis). Once the cellular debris was discarded and the protein concentration determined, 50 μg of the lysate was denatured by boiling it with 4xSDS. 1 mg of protein per sample was then pipetted into a 2 mL Eppendorf tube, and the volumes of all samples were equalized using RIPA buffer. In order to avoid unspecific ubiquitin smears possibly resulting from autoubiquitination of FBXO7, the samples were first incubated with 1.5 % SDS for 10 min on the roller mixer at RT, followed by boiling step at 95°C for 30 min. The samples were then transferred onto 15 mL test tubes and diluted 1:10 in Ubiquitination Assay Lysis bufer. The samples were then incubated with 10 μL anti-FLAG® M2 affinity Gel beads (SIGMA ALDRICH®) overnight on the roller mixer at 4°C. For the interaction strength assay, an initial incubation with 0.75 μL anti-FLAG antibody for 1 hour at 4°C was followed by 1 hour incubation with 20 μL Protein A Sepharose bead slurry. The beads were then transferred back into 1.5 mL tubes and washed twice with RIPA (with SDS) or alternatively for the mutant interaction strength assay- lysis buffer, followed by a PBS wash. Finally the proteins were eluted from the samples by boiling them for 5 min with ca. 30 μL SDS Sample buffer.

v. Quantitative mass spectrometry sample preparation

The transfected HEK 293T cells were lysed in co-immunoprecipitation buffer as previously described in **Section 2.2.6.i**. 500-750 μg dry protein weight was incubated with 20 μL anti-FLAG® M2 affinity Gel beads (SIGMA ALDRICH®) for 4 hours at 4°C on the roller mixer. The beads were

spun down at 6000 rpm, and washed twice with lysis buffer and twice with cold PBS, resuspended in 20 μL of PBS and snap frozen in liquid nitrogen and stored at -80°C. 20 μg of the lysates were boiled with 4x SDS as input control as well as 5 μL of the immunoprecipitated solution. The mass spectrometry was performed by Dr. Christian Preisinger at the Proteomics Facility, Interdisciplinary Center for Clinical Research (IZKF) Aachen, Medical Faculty, RWTH Aachen. Briefly, the samples were digested using 2M urea, desalted and lyophylized. The peptides were resuspended in formic acid and analyzed using Orbitrap Elite mass spectrometer (Vingill et al., 2016). The resulting data was analyzed using MaxQuant (v. 1.5.2.8) and SwissProt (v. 06/2015) Database (Cox and Mann, 2008; Cox et al., 2011; Vingill et al., 2016).

vi. SDS-PAGE and Western Blotting

The SDS-PAGE was performed following the method described in Laemmli *et al.*(Laemmli, 1970), with modifications. The SDS-PAGE acrylamide gels were cast in the Mini-PROTEAN® Tetra Electrophoresis System (BioRad) using the 1.0 or the 1.5 mm spacer plates and combs. Detailed volumes for the preparation of the gels are listed in **Table 2.9**:

Table 2.9 Volumes of reagents used to prepare SDS-PAGE acrylamide gels

	Separating Gel		Stacking Gel
	10%	12%	
Acrylamide (mL)	2.5	3	0.65
Lower/Upper Buffer (mL)	1.875	1.875	1.25
H_2O (mL)	3.125	2.625	3.05
10% APS (μL)	30	30	30
TEMED (μL)	3	3	3

Firstly, the 10-12 % (depending on the experiment) separating gel was poured into the gel casting chambers and covered with 1 mL of isopropanol to ensure the removal of bubbles as well as sharp horizontal separation. Once the separating gel had solidified and the isopropanol washed, a 3.9 % separating gel was poured on top of the stacking gel, a comb was inserted and the stacking gel was allowed to polymerize.

The denatured in 4xSDS sample Buffer lysates were loaded onto the gels together with PageRuler Prestained protein ladder (Thermo Fisher Scientific) and the proteins were resolved at

35 mA (max Voltage) per gel. After electrophoresis, the gels were stacked on top of a nitrocellulose blotting membrane (Amersham™, GE Healthcare Life Sciences) and the proteins were transferred for 90-110 min at 250 mA using the wet transfer system Mini Trans-Blot (BioRad) or alternatively the dry transfer system from Biometra Analytic (Jena). The membranes were then incubated for 30 min, shaking at RT with 4% milk in PBST to block the potential sites of non-specific antibody bindings. Next, the membranes were washed 3 times each with PBST for 10 min. The membranes were then incubated with the required primary antibody diluted in primary antibody blocking solution at the optimized dilutions and durations listed in **Table 2.1**. The membranes were then washed again three times with PBST and incubated for 35-45 min with secondary HRP-conjugated antibody diluted 1:10000 in 4% milk in PBST. After a final washing step with PBST, the membranes were incubated briefly with enhanced chemiluminescent horseradish peroxidase substrate kit (Pierce™, ThermoFisher Scientific). The membrane was visualized either using a photographic film (Amersham Hyperfilm™) that was developed in an automatic developer (Curix 60, Agfa) or using the Chemiluminescence Documentation System Alliance (Biometra) and the Alliance (UVITECH, Cambridge) software.

2.2.7. NEX-Cre;Fbxo7$^{fl/fl}$ mouse line generation and genotyping

i. Generation of NEX-Cre;Fbxo7$^{fl/fl}$ transgenic mice

The *Fbxo7* knockout mouse line was generated as described in Vingill *et al*. by Nicola Schwedhelm-Domeyer, Cellular and Molecular Neurobiology, Max Planck Institute of Experimental Medicine, Göttingen (Vingill et al., 2016). In brief, embryonic stem cells containing the transgenomic sequence, where exon four of the *Fbxo7* gene is flanked by loxP sites, were injected in pseudopregnant C57BL/6 mice to create chimeric offspring. The chimeric mice were then further bred until achieving homozygous offspring that was then crossed with a NEX-Cre mouse line to generate the NEX-Cre/*Fbxo7*$^{fl/fl}$ mice (Goebbels et al., 2006; Vingill et al., 2016)

ii. Isolation of genomic DNA

Genomic DNA for sequencing was extracted from the mouse tails, that were digested for minimum 2 hours in 200 µL of Tail lysis buffer containing 3 µL proteinase K (200 µg/mL) and 8 µL of 5 M NaCl. After ensuring that the tails are completely digested, the samples were spun down for 10 min at 14000 rpm and the supernatant was transferred into fresh eppendorf, omitting the undigested remains. The DNA was precipitated using 300 µL of 99% ethanol and collected at the bottom of the tube by centrifugation for 3 min at max speed. The DNA was washed with 70% ethanol, air-dried, and finally resuspended in 100-200 µL of ddH_2O.

iii. Genotyping

Two separate primer sets were designed to genotype the NEX-Cre/*Fbxo7*$^{fl/fl}$ mice. The first set targets only *Fbxo7* wild type alleles, where the second set would test for the expression of Cre recombinase. The list of the sequences of the primers used can be found in **Appendix, Table A**. The primers were added to the genotyping mix as follows:

Table 2.10 Genotyping reaction mix

Reagent	Volume (μL)
Genomic DNA	0.5-1
Forward and reverse primers (10 pmol/μL)	1
dNTP (2.5 mM)	0.4
GoTaq® DNA Polymerase	0.1
5x GoTaq® reaction buffer	5
Total reaction Volume	25

The PCR reaction was then amplified using the programs that are mentioned in **Table 2.11**:

Table 2.11 PCR thermocycler program used

Process	Temperature (°C)	Duration (min)	
Denaturation	95	3	
PCR denaturation	95	0.5	28 cycles
Primer annealing	51	0.5	
Elongation	72	2	
Final elongation	72	10	

2.2.8. Immunohistochemistry

i. Transcardial perfusion and fixation of mouse brains

Adult mice were initially anesthetized by intraperitoneal injection of 10% ketamine [v/v] mixed with 5% xylazine [v/v]. The mice were fixed dorsally and their diaphragm was exposed and cut, allowing access to the heart. A butterfly cannula (Venoflix®, Braun) connected to peristaltic pump was inserted carefully into the left ventricle avoiding piercing through the ventral wall of the heart or the left atrium. The right atrium was incised and PBS was allowed to flow through the peristaltic pump to flush away the blood form the organs. Next, freshly prepared 4% PFA for paraffin embedding was run through the pumps until the organs were fixed. The brain was dissected out and left overnight in 4% PFA at 4°C, and then diluted down to 1% PFA using PBS and left for another 2 days.

ii. Post-fixation paraffin embedding and sectioning

The fixed brains were embedded in paraffin (Paraplast®, Leica) using a pre-set program of the embedding tissue processor described in **Table 2.12**:

Table 2.12 Pre-set dehydration/paraffinization program

Procedure	Duration (hr)
50% Ethanol	1
70% Ethanol	2x2
96% Ethanol	2x2
100% Ethanol	2x2
Isopropanol	1
Xylol	2x2
Paraffin	2x2

Finally, the brains were positioned horizontally in metal moulds, embedded in 60°C paraffin and allowed to set by cooling. The paraffin blocks were cut into 5 μm thin sections using a microtome, and then allowed to settle and unwrinkle in a 40°C water bath, collected onto slides and allowed to dry at RT. Dr. Siv Vingill kindly provided some of the brain samples.

iii. Deparaffinization, rehydration and antigen retrieval

The sections were subjected to deparaffinization through two incubation steps with xylol, 10 min each, and incubation with Xylol/Isopropanol (1:1) for another 10 min. The slides were then rehydrated in a series of 5 min incubation steps in decreasing percentages of ethanol (100%, 90%, 70%, and 50%) and a final step of incubation in ddH_2O. In order to ensure antibody-antigen binding, an antigen retrieval step was carried out by initially incubating the slides for 5 min in cold citrate buffer and then submerging the slides in preheated citrate buffer and a final boiling step at 650 Watts for 10 min. The slides were then allowed to cool down at RT in the citrate buffer.

iv. Immunohistological staining of tissues embedded in paraffin

Proteinase K digestion step was preformed only for immunohistological staining with α-synudein. The slides were incubated for 35 min at 37°C in 1:500 Proteinase K (200 μg/mL) diluted in Proteinase K digestion buffer. The sections were rinsed with fine- filtered 2% milk in Tris buffer [w/v] and mounted into a vertical position with the help of cover plates (Shandon™, Thermo Fisher Scientific, UK) and immunohistological rack. Special care was taken to avoid any trapped bubbles between the surface of the microscopy slides and the cover plates. The sections were washed in 2% milk in Tris buffer again, followed by endogenous peroxidase inhibition step performed by 5 min incubation with 3% H_2O_2. After one more wash with 2% milk in Tris buffer, the non-specific epitopes were blocked in blocking buffer for 10 min at RT and the primary antibody diluted in blocking buffer was incubated overnight at 4°C. On the next day, the slides were rinsed with 2% milk in Tris buffer and a secondary antibody conjugated to biotin ($LSAB_2$ kit, Dako, USA) was incubated with the brain sections for 10 min at RT. Next, the slides were further incubated with peroxidase-conjugated streptavidin for 10 min, and finally rinsed with Tris buffer. The cover plates were then carefully detached from the coverslips, the sections of interest were encirded using a Dako pen, and the binding sites were stained using the chromogen 3-3'-diaminobenzidine (DAB) (Dako, USA) that results in brown precipitation in the presence of peroxidase activity. Finally, the slides were rinsed twice with ddH_2O

v. Nuclear staining, rehydration and mounting

The sections were briefly dipped in 0.1% haematoxylin [w/v], rinsed in ddH_2O and developed in HCl/Alcohol. To increase the saturation of the blue tint, the slides were dipped in Scott's solution (Thermo Fisher Scientific) and then rinsed once more with ddH_2O. Next, the slides were dehydrated using the same ethanol concentrations described in the previous section, but in the reverse order followed by Xylol/Isopropanol and two times 10 min Xylol incubation. Eukitt®

(Kindler) mounting medium was spread thinly over cover slips, which were then carefully placed onto the slides, clearing off any air bubbles.

vi. Terminal deoxynucleotidyl transferase dUTP nick end labeling assay (TUNEL) assay

The slides were deparaffinized and dehydrated as mentioned in **Section 2.2.8.iii**. The TUNEL assay was performed as per the manufacturer's instructions- DeadEnd™ Colorimetric TUNEL System kit (Promega). Following heamatoxylin staining, the slides were rinsed in ddH_2O and covered using the Aqua-PolyMount (Polysciences) mounting medium.

vii. Imaging, analysis and quantification

All images were acquired using a bright field microscope Axio-Observer Z1, Zeiss, and the ZEN 2011 imaging software. The number of cell nuclei stained by the TUNEL assay as well as the Iba1 positive cells were manually counted in blinded manner. The area quantification as well as the GFAP- and Iba1- positive areas was quantified using imageJ macro provided by Dr. Mitkovski, Max Planck Institute of Experimental Medicine, Göttingen, and previously published by Dr. David Brockelt (Brockelt, 2015). The threshold was determined for each individual imaging session.

3. Results

Although research in the FBXO7 field in the recent years has yielded results that are helpful in entangling the pathways of neurodegeneration, there are still many questions to be raised. Some of these questions were investigated in my research. For example, is FBXO7 localization nuclear or cytoplasmic? Does *Fbxo7* knockout have effect on the cellular and/or mitochondrial morphology? Are there any unknown processes or interactors that FBXO7 may be involved in/with? And last but not least, what is the role of FBXO7 in the forebrain? To answer them, I used an array of biochemical, molecular, cellular and histological procedures, that resulted in the following findings:

3.1. FBXO7 localization and interactome

3.1.1. FBXO7 is localized in the cytoplasm

Localization of FBXO7 in cells has been controversial. Previous immunocytochemical analysis on HEK 293T, SH-SY5Y cells and patients' fibroblasts have showed that wild type FBXO7 localizes to the nucleus (Zhao et al., 2011). However, in our laboratory, it was previously found by using the transgenic *Fbxo7* knockout mice, that commercially available antibodies against FBXO7 fail to detect the presence of FBXO7 by immunocytochemical analysis. Furthermore, nuclear fractionation assay results showed that FBXO7 was predominantly localized in the cytoplasmic fraction (Brockelt, 2015). In order to shed more light on the localization of FBXO7, I transfected different cell types with FBXO7 constructs that were tagged either C-terminally or N-terminally. Upon overexpression of the different FBXO7 proteins in mouse cortical neurons **(Fig. 3.1 A)**, HEK 293T **(Fig. 3.1 B)** and SH-SY5Y cells **(Fig. 3.1 C)**, I saw that nearly all healthy cells had the FBXO7 signal within their cytoplasm, confirming the previous findings from our lab.

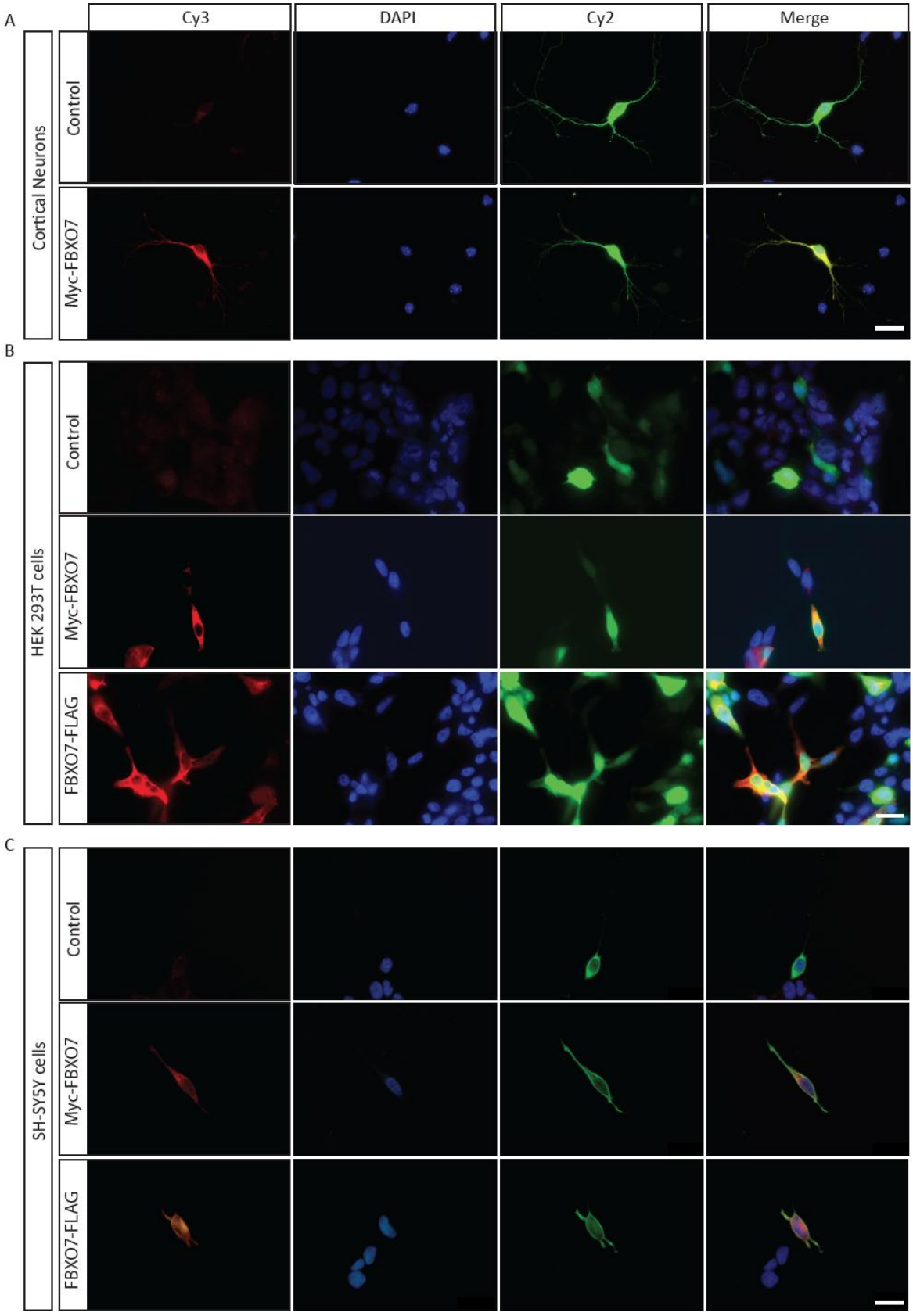
A
Cy3
DAPI
Cy2
Merge
Cortical Neurons
Control
Myc-FBXO7
B
HEK 293T cells
Control
Myc-FBXO7
FBXO7-FLAG
C
SH-SY5Y cells
Control
Myc-FBXO7
FBXO7-FLAG

Fig. 3.1 FBXO7 localizes to the cytoplasm

(A-C) Representative images of mouse cortical neurons **(A)**, HEK 293T cells **(B)** or SH-SY54Y cells **(C)** transfected with tagged FBXO7 or control together with GFP transfection marker. The cells were transfected at DIV 3 and stained at DIV 8 **(A)** or at DIV 1 and stained at DIV 3 **(B** and **C)**. The N-terminally Myc-tagged FBXO7 was then detected using the anti-Myc antibody as primary antibody and Cy3-conjugated secondary antibody, depicted in red. Cy2 was used to enhance the GFP signal depicted in green. The nuclei were counter-stained with DAPI. Magnification: 60x. Scale bar = 20 μm.

3.1.2. FBXO7 is involved in multiple cellular mechanisms according to quantitative mass spectrometry data

There are several major interaction partners known for FBXO7 such as PINK1, Parkin, Skp1 and PSMA2 (Burchell et al., 2013; Cenciarelli et al., 1999; Vingill et al., 2016). However, we wanted to get a full representation of FBXO7 interactome in the HEK 293T cell line, and link the interaction partners according to their function in the cell. In order to achieve this, I overexpressed FLAG-FBXO7 in HEK 293T cells, and using FLAG-beads, immunoprecipitated FBXO7 together with all proteins and complexes it associates with and sent the samples for mass spectrometry analysis at the Proteomics Facility at the Medical Faculty of the RWTH Aachen **(Fig. 3.2 B)**. The proteins that were most enriched in the FBXO7 overexpressing cells were, as expected, part of the SCF complex, namely, the known interactors cul1, Skp1 and Rbx1 (Cenciarelli et al., 1999), as well as proteins that associate to form the proteasome such as PSMA2, PSMA6, PSMB1, PSMB3 and PSMB4 **(Fig. 3.2 A i)** (Vingill et al., 2016). The second major cluster of proteins that were quite eminent are those involved in mitochondrial maintenance and cellular respiration **(Fig. 3.2 A ii)**. Proteins, responsible for cytoskeletal organization and maintenance as well as non-clathrin mediated vesicular transport noticeably between the endoplasmic reticulum and the Golgi apparatus were also enriched in the mass spectrometry analysis **(Fig. 3.2 A v, vi)**. Furthermore, there was an overrepresentation of protein and protein complexes involved in DNA repair as well as nuclear pore formation and transport **(Fig. 3.2 A iii, iv)**. To further confirm the data from the mass spectrometry analysis, I went on to check some of the newly identified interactions. I selected two of the proteins from the DNA repair cluster, and performed a simple one-way co-immunoprecipitation using antibodies that would immunoprecipitate the targeted potential novel interaction partners of FBXO7 and observed a positive co-immunoprecipitation bands **(Fig. 3.2 C)**.

These findings simultaneously confirmed the known interaction partners and opened the possibility for novel proteins and complexes that may interact directly or indirectly with FBXO7.

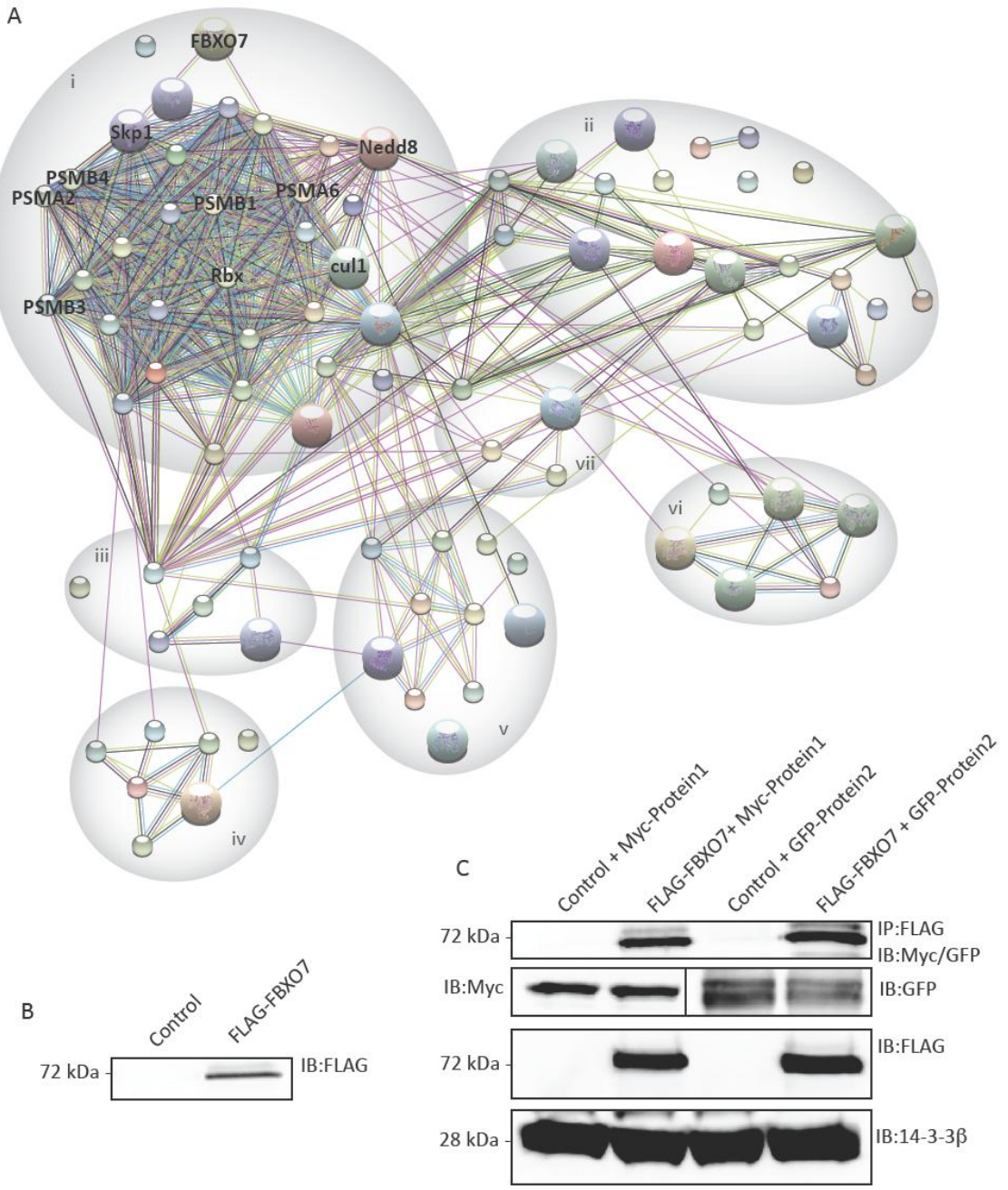

Fig. 3.2 FBXO7 interactors predicted by quantitative mass spectrometry

(A) Network of FBXO7 interactors generated by using STRING database (http://string-db.org). The interactor list was obtained through mass spectrometry analysis of the 88 candidates and the data was fed into the STRING database. The interactors were then grouped according to their generalized function in the cells as follows: ubiquitination and proteasomal degradation (i), mitochondrial maintenance (ii), DNA repair (iii), formation of nuclear pores and protein transport (iv), cytoskeletal organization and remodeling (v), ER to Golgi vesicular transport (vi) and proteins with dual functionality (vii). **(B)** Western blotting of 50 μg of input obtained from the lysis of HEK 293T cells transfected with either empty vector or FLAG-tagged FBXO7.

The FLAG-FBXO7 was immunoprecipitated and sent for mass spectroscopy analysis performed by Dr. Christian Preisinger at the Proteomics Facility at the RWTH Aachen. **(C)** Co-immunoprecipitation analysis represented in one blot showing the interaction between FBXO7 and two of its potential interactors. The proteins of interest were overexpressed in HEK 293T cells together with FLAG-FBXO7 control vectors. Cells were lysed ca. 72 hours after transfection and the lysates were subjected to immunoprecipitation with either anti-GFP or anti-Myc antibody. The interaction was detected by immunoblotting the membrane using anti-FLAG antibody. 50 μg of the lysate were used as expression (anti-Myc, anti-GFP and anti-FLAG antibody) and loading (14-3-3β antibody) control.

3.2. Biochemical analysis of the FBXO7-MAP1B LC1 interaction

3.2.1. FBXO7 binds to the light chains of the MAP1 family

In a yeast-two-hybrid assay using FBXO7 as bait, Dr. David Brockelt showed that amongst the known interaction partners, FBXO7 could also interact with the microtubule associated protein 1B light chain1 (MAP1B LC1) (Brockelt, 2015). Since the light chains of the MAP1s are highly homologous, Dr. Brockelt reasoned that FBXO7 may also interact with the other members of the MAP1 family. I re-confirmed these interactions by forward and reverse co-immunoprecipitation followed by western blotting of FBXO7 together with MAP1B LC1 and MAP1B LC2 **(Fig. 3.3 A-B).** I also established that FBXO7 interacts with the light chain of the MAP1S **(Fig. 3.3 C).** Additionally I checked if there is interaction between FBXO7 and α-synuclein, since both are encoded by *PARK* loci and it was previously found that FBXO7 interacts directly with PINK1 (PARK6) and Parkin (PARK2) (Burchell et al., 2013), but observed no interaction band on the western blot analysis after co-immunoprecipitating either FBXO7 or α-synuclein **(Fig. 3.3 D).** Taken together, these data establish MAP1S LC as novel interactor for FBXO7 and indicate that α-synudein does not interact with FBXO7.

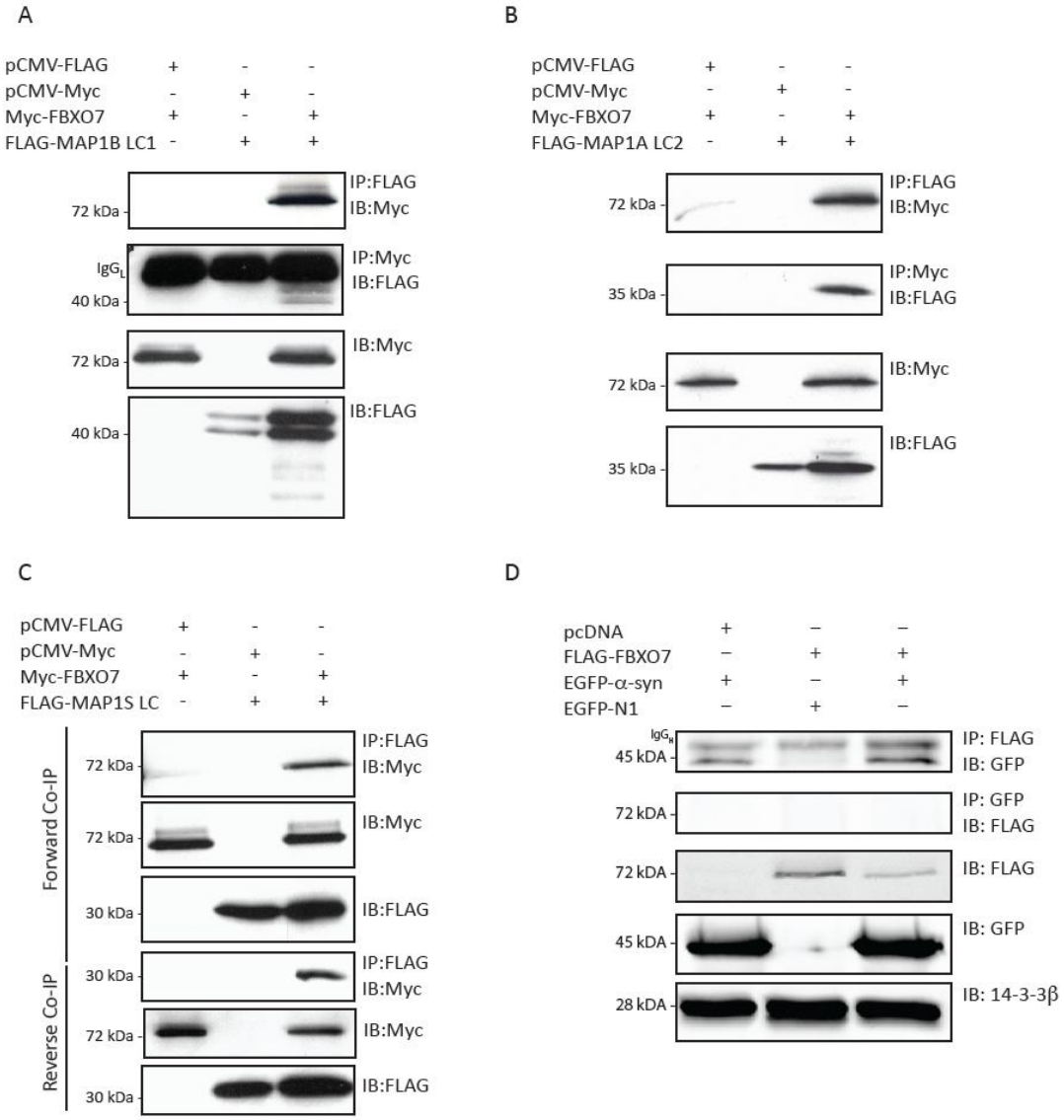

Fig. 3.3 FBXO7 interacts with the members of the MAP1 family but not with α-synuclein

(A-B) Forward and reverse co-immunoprecipitation represented in one blot showing the interaction between FBXO7 and MAP1B LC1 **(A)** or FBXO7 and MAP1A LC2 **(B)** performed by overexpressing of the proteins of interest and their respective cloning vectors as control in HEK 293T cells. Cells were lysed ca. 72 hours after transfection and the lysates were subjected to immunoprecipitation with the corresponding antibodies. The presence of the interaction partner was detected by immunoblot analysis with the corresponding antibody. 50 µg of the lysate was used for expression (anti-Myc antibody and anti-FLAG antibody) and loading (14-3-3β antibody) control. **(C)** Forward and reverse co-immunoprecipitation on different blots showing the interaction between FBXO7 and MAP1S LC, performed by overexpressing of the proteins of interest and their respective cloning vectors as control in HEK 293T cells. **(D)** Co-immunoprecipitation assay performed by overexpressing α-synuclein and FBXO7 and their respective cloning vectors as control in HEK 293T cells. Cells were lysed ca. 72 hours after transfection and the lysates

were subjected to immunoprecipitation with the corresponding antibody. 50 mg of the lysate was used as expression (GFP and FLAG antibody) and loading (14-3-3β antibody) control.

3.2.2. FBXO7 binds strongly to MAP1B LC1 independently of its SCF functions

In order to see if the interaction would result in a functional modification of MAP1B LC1, I co-transfected empty, wild type or ΔF-box construct of FBXO7 (lacking the F-box domain) together with MAP1B LC1. I observed, similarly to Dr. Brockelt, a slight increase in the signal for MAP1B LC1 every time I overexpressed the protein together with FBXO7 but not the control vectors. This is indicative that the stabilization of MAP1B LC1 is possibly susceptible to the FBXO7's ligase activity **(Fig. 3.4 A)**. Since one of the main functions of FBXO7 is ubiquitin ligation to substrate proteins, I checked if in the presence of FBXO7, MAP1B LC1 gets ubiquitinated (Chang et al., 2006b). To test this, I overexpressed ubiquitin and MAP1B LC1 in all conditions, together with empty control vector, FBXO7 wild type plasmid or a FBXO7 version of the protein lacking its F-box domain, rendering it incapable of binding to the SCF complex. To avoid detection of the auto-ubiquitination signal of FBXO7, I subjected the lysates to a boiling protocol that I had previously established. Under these conditions, I observed no increase in the ubiquitin signal **(Fig. 3.4 B)**. Furthermore, the immunoblotting corresponding to MAP1B LC1 was again stronger and had multiple bands whenever FBXO7 and MAP1B LC1 were co-expressed, but not when MAP1B LC1 was co-expressed with the empty vector or with the FBXO7 ΔF-box construct **(Fig. 3.4 B)**.

To further confirm that the interaction between FBXO7 and MAP1B LC1 does not lead to the ubiquitination of the substrate, I checked if it is dependent on the formation of the SCF complex. Therefore, I performed another co-immunoprecipitation analysis in which I immunoprecipitated either FBXO7 or MAP1B LC1 using either anti-FLAG or anti-Myc antibody **(Fig. 3.4 C)**. I then blotted the membrane to check for the presence of cul1, since cul1 is the main scaffolding protein of the SCF complex **(Fig. 3.4 C)** (Willems et al., 2004). I was able to detect signal whenever I immunoprecipitated the FBXO7 protein but the signal was absent when I immunoprecipitated the MAP1B LC1 indicating that MAP1B LC1 does not interact with the cytoplasmic FBXO7 associated with the SCF-complex **(Fig. 3.4 C)**. I went on to further show that the interaction between FBXO7 and MAP1B LC1 was still present by stripping the membranes and reblotting them with either anti-FLAG or anti-Myc antibody **(Fig. 3.4 C)**. In summary, MAP1B LC1 stabilization is influenced by FBXO7 in HEK 293T cells, and the interaction between these two proteins does not lead to the light chain's ubiquitination.

Whilst standardizing the boiling steps of the ubiquitination assay, I realized that the interaction between FBXO7 and MAP1B LC1 is quite strong as I needed a higher than usual concentration of SDS and up to 30 min of boiling to disrupt the interaction. Therefore, I asked whether the strength of this interaction is altered in the known pathological mutants of FBXO7. I subjected the lysates to similar protocol as the boiling protocol, except, I used 1.0% of the SDS instead of 1.5% to avoid complete loss of the signal. I observed that the interaction remained strong in all mutants except for the M115I **(Fig. 3.4 D)**. However, the expression control blotting revealed that this interaction decreases also the MAP1B LC1 stability and thus the band for MAP1B LC1 was of similar thickness as the control band **(Fig. 3.4 D)**.

These results corroborated previous findings in our lab and further enhanced our knowledge on the non-E3 ligase dependant interaction between FBXO7 and MAP1B LC1 and the significance of the M115I SNP in the MAP1B LC1 stability.

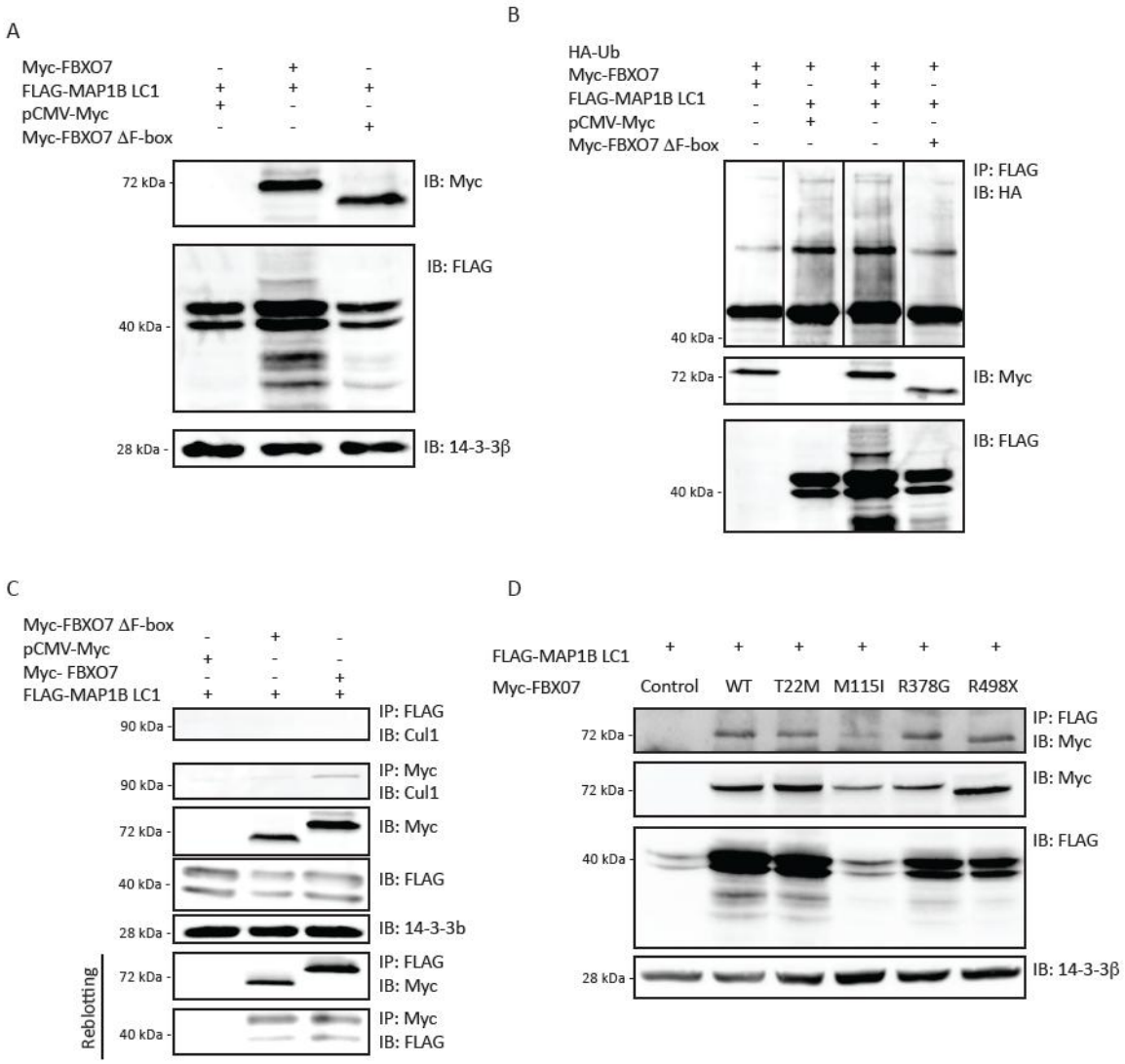

Fig. 3.4 FBXO7 interacts with the MAP1B LC1 proteins independent of its ligase activity

(A) Representative western blot analysis of the effect of co-expressing FBXO7 together with MAP1B LC1. 50 µg of HEK 293T cells lysate either overexpressing control, wild type or ΔF-box variant of FBXO7 and MAP1B LC1 were immunoblotted using the anti-Myc and the anti-FLAG antibody respectively. (**B)** Ubiquitination assay of MAP1B LC1. HEK 293T cells were transfected either with control vector, FBXO7 wild type or a ΔF-box FBXO7 together with HA-Ubiquitin and MAP1B LC1. The cells were lysed using RIPA buffer and subjected to incubation with 1.5% SDS for 10 min at RT and then 30 min at 95°C. The presence of ubiquitin was tested by immunoblotting the membrane with anti-HA antibody. 50 µg of the lysate was used for expression and loading control. **(C)** Representative co-immunoprecipitation analysis showing the interaction between FBXO7 and MAP1B LC1 with cul1, performed by overexpressing myc-FBXO7 and FLAG-MAP1B LC1 in HEK 293T cells. Cells were lysed ca. 72 hours after transfection and the lysates were subjected to immunoprecipitation with the corresponding antibody. The presence of the interaction partner was detected by immunoblotting the membrane for endogenously expressed cul1. 50 µg of the lysate was used

for expression (anti-Myc antibody and anti-FLAG antibody) and loading (14-3-3β antibody) control. The membranes were then subjected to stripping and re-blotting with the indicated antibodies. **(D)** Representative co-immunoprecipitation blot showing the interaction between MAP1B LC1 and different known mutations of FBXO7. The mutated FBXO7 plasmids were transfected together with MAP1B LC1 in HEK 293T cells. Cells were lysed and subjected to immunoprecipitation using anti-FLAG antibody. The presence of the interaction partner was detected by immunoblotting the membrane with the anti-myc antibody. 50 µg of the lysate was used for expression (anti-Myc antibody and anti-FLAG antibody) and loading (14-3-3β antibody) control.

3.3. Cellular pathways influenced by FBXO7 and MAP1B LC1

Once the interaction was established, I wondered which cellular processes would be influenced and what is the molecular relevance of the knockdown of the proteins. I performed a series of experiments trying to illuminate the role of both FBXO1 and MAP1B LC1 in the cell, starting with an all-encompassing mass spectroscopy analysis and then diving down to cellular and organellar morphology.

3.3.1. Mass Spectroscopy analysis of the MAP1B LC1 pull down enriched for FBXO7 hints for mitochondrial involvement

Since the interaction between MAP1B LC1 and FBXO7 was confirmed, we wanted to see which proteins would be upregulated in the presence of both proteins. In order to do this, I transfected HEK 293T cells with FBXO7 and MAP1B LC1, immunoprecipitated for the MAP1B LC1 and sent the samples for mass spec analysis at the Proteomics Facility at the RWTH Aachen (**Fig. 3.5 B**). The resulting list contained different protein members responsible for ubiquitination of proteins, which was expected since the cells were transfected with FBXO7: an E3 ubiquitin ligase. I also saw an increase in cytoskeletal subunits, again an expected result, since I overexpressed MAP1B LC1, whose main function is cytoskeletal stabilization (Togel et al., 1998b). Interestingly, there was a large group of proteins that are involved in mitochondrial homeostasis and metabolic processes as well as proteins involved in the repair and transcription of DNA **(Fig. 3.5 A)**.

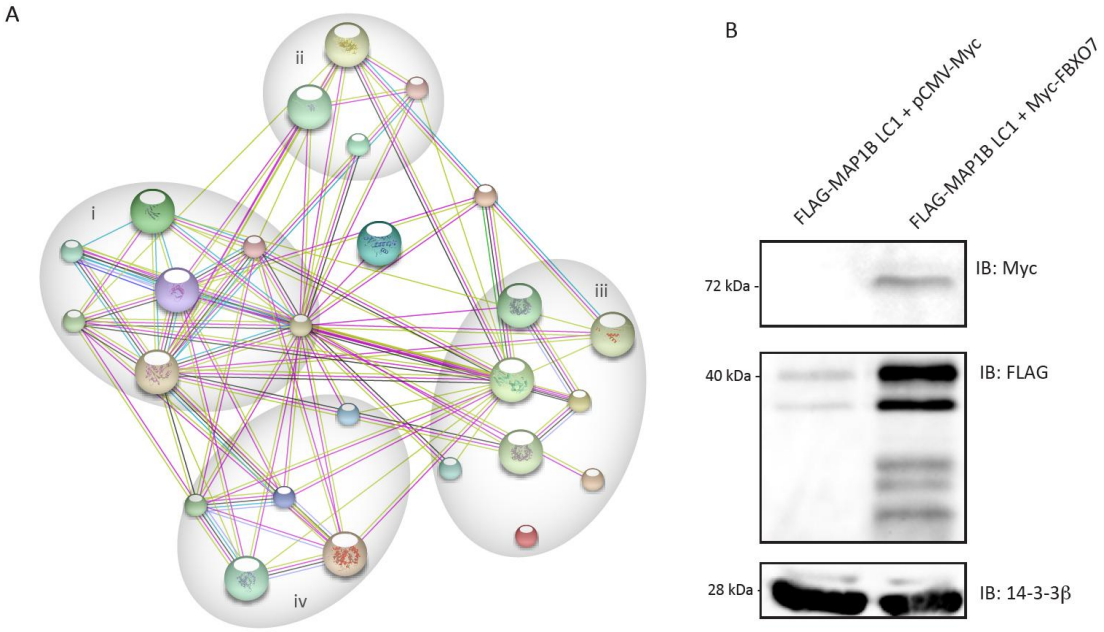

Fig. 3.5 The FBXO7-MAP1B interaction: novel involvement in mitochondrial health and DNA processing

(A) Networks of FBXO7-MAP1B LC1 enrichment experiment generated by using STRING database (http://string-db.org). The protein list was obtained through mass spectrometry analysis and 26 candidates with the highest peptide concentration ratio were picked and fed into the STRING database. The proteins were then grouped according to their generalized function in the cells as follows: ubiquitination and proteasomal degradation (i), DNA repair and transcription (ii), mitochondrial maintenance and (iii) cytoskeletal assembly (iv). **(B)** Western blotting of 50 µg of input obtained from the lysis of HEK 293T cells overexpressing either empty Myc-vector together with FLAG-MAP1B LC1 or Myc-FBXO7 together with FLAG-MAP1B LC1. The FLAG-MAP1B LC1 was immunoprecipitated using FLAG beads and sent for mass spectroscopy analysis. The 14-3-3β antibody was used as loading control.

3.3.2. FBXO7 is required for the proper dendritogenesis

As mentioned in the introduction, FBXO7 is a protein with multiple cellular functions ranging from mitophagy, cell cycle and proteasome regulation to sperm production in *Drosophila melanogaster* (Burchell et al., 2013; Kirk et al., 2008; Laman et al., 2005; Vingill et al., 2016). Having such diverse involvement in major cellular processes, as well as my previous results linking FBXO7 to the cytoskeleton, I went on to characterize the gross morphology of neurons lacking FBXO7. I transfected rat cortical neurons with control plasmids or FBXO7 shRNA together with β-galactosidase as transfection marker and subjected them to immunocytochemical staining **(Fig. 3.6 A).** Finally, I measured the average axonal and total dendritic lengths of at least 40 neurons per condition. While I saw no difference in the average axonal length **(Fig. 3.6 B)**, there was a

marked decrease by almost half in the average total dendritic length as well at the average number of dendrites in neurons transfected with the functional FBXO7 shRNA compared to control neurons **(Fig. 3.6 C, D)**. These results point to a novel role of FBXO7 in dendritic arborization and outgrowth.

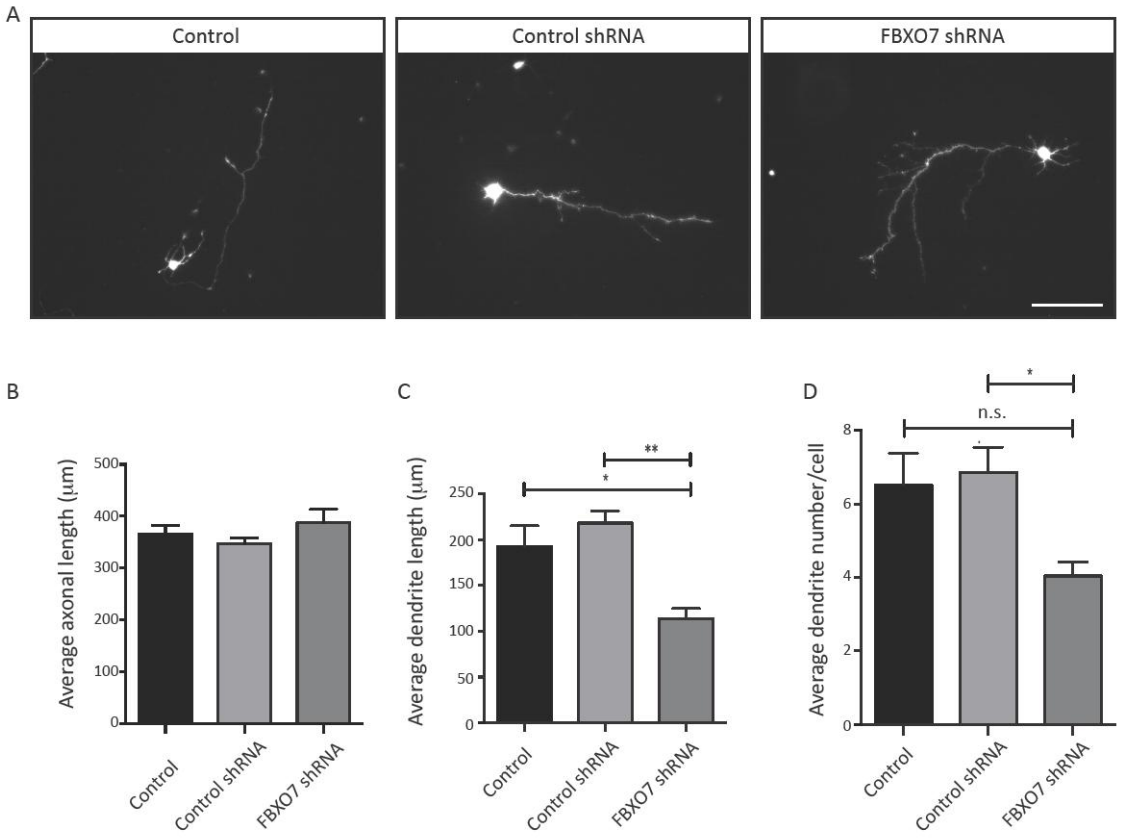

Fig. 3.6 FBXO7 knockdown results in fewer and shorter dendrites

(A) Representative images of (P0) rat cortical neurons transfected at DIV1 with either control or FBXO7 shRNA vectors together with a β-galactosidase encoding plasmid serving as transfection marker. The neurons were fixed and stained at DIV6 using anti-β-galactosidase antibody as primary antibody, followed by Cy2-conjugated antibody. Magnification: 20x. Scale bar = 100 µm. **(B)** Quantification and statistical analysis of the average axonal length using one-way ANOVA (N=3, mean + s.e.m.) **(C)** Quantification and statistical analysis of the average total dendritic length using one-way ANOVA (N=4,*P<0.5; **P<0.01, mean + s.e.m.) **(D)** Quantification and statistical analysis of the average dendritic number per cell using one-way ANOVA (N=4,*P<0.5; n.s.=non- significant, mean + s.e.m.)

3.3.3. Knockdown of FBXO7 leads to mitochondrial fragmentation

As previously noted, FBXO7 was also found to play a role in regulation of mitophagy, where misregulated mitochondrial clearance results in mitochondrial depolarization (Delgado-Camprubi et al., 2017; Zhou et al., 2015). Furthermore, disruptions in mitochondrial homeostasis and maintenance have been the cellular hallmark for PD. I used mitochondrial morphology as a read-out for healthy vs. aberrant organelles and tested whether FBXO7 leads to mitochondrial fragmentation. I co-transfected HEK 293T cells with FBXO7 shRNA together with a GFP tagged ornithine transcarbamylase (OCT) that is expressed in the inner mitochondrial membrane (IMM), serving as mitochondrial marker (Henslee and Srere, 1979; Munch and Harper, 2016). By immunoblotting whole cell extracts, I confirmed that the FBXO7 shRNA sufficiently blocks the expression of the targeted protein **(Fig. 3.7 B)**. I classified the mitochondria into three categories based on their morphological appearance: tubular, globular and fragmented **(Fig. 3.7 A)**. After analyzing a minimum of 100 cells per condition, I saw a significant increase in the number of HEK 293T cells with fragmented mitochondria at the expense of cells containing tubular organelles in the FBXO7 knockdown condition in comparison to control **(Fig. 3.7 C)**. Furthermore, there was no change in the number of cells with globular mitochondria.

To check if this is a general consequence of FBXO7 knockdown and if mitochondrial morphology is influenced by FBXO7 in neuronal cells, I repeated the experiment in immortalized neuroblastoma SH-SY5Y cells. I transfected the cells using Lipofectamine 2000 for maximal transfection rate with the same plasmids and categorized the mitochondria as previously described **(Fig. 3.7 D)**. I did not see any significant difference in the mitochondrial morphology of cells **(Fig. 3.7 F)**. To ensure that this was not due to a lack of FBXO7 expression in the SH-SY5Y cell line, I also checked for the presence of FBXO7 in these cells at different times of passaging by western blotting, and detected a clear band confirming the endogenous FBXO7 expression in SH-SY5Y **(Fig. 3.7 E)**. These data taken together indicate that FBXO7 may play a protective role in mitochondrial health and homeostasis in HEK 293T cells.

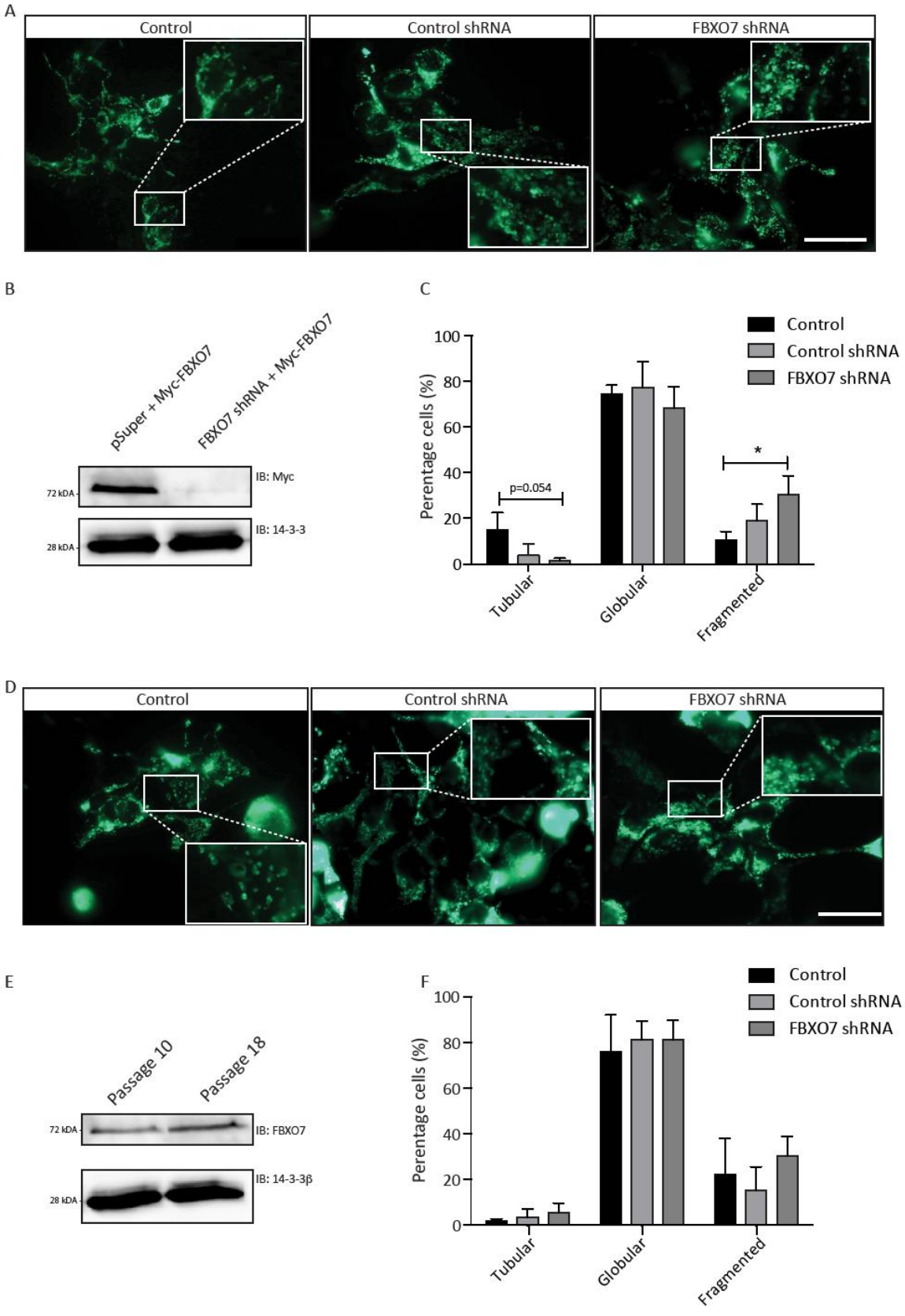
A
Control
Control shRNA
FBXO7 shRNA
B
pSuper + Myc-FBXO7
FBXO7 shRNA + Myc-FBXO7
72 kDA
IB: Myc
28 kDA
IB: 14-3-3
C
Control
Control shRNA
FBXO7 shRNA
Perentage cells (%)
100
80
60
40
20
0
p=0.054
*
Tubular
Globular
Fragmented
D
Control
Control shRNA
FBXO7 shRNA
E
Passage 10
Passage 18
72 kDA
IB: FBXO7
28 kDA
IB: 14-3-3β
F
Control
Control shRNA
FBXO7 shRNA
Perentage cells (%)
100
80
60
40
20
0
Tubular
Globular
Fragmented

Fig. 3.7 Effect of FBXO7 knockdown in mitochondria

(A) Representative images of HEK 293T cells transfected at DIV3 with either control or FBXO7 shRNA vectors together with OCT-GFP expression plasmid serving as mitochondrial marker. The cells were fixed and stained at DIV8 using DAPI as nuclear counterstain. Magnification: 60x. Scale bar = 100 μm. **(B)** Quantification and statistical analysis of minimum 100 cells per condition with their mitochondria categorized as either tubular in appearance, globular or fragmented, using one-way ANOVA after normalization (N=3,*P<0.5; mean + s.e.m.) **(C)** Proof for the FBXO7 shRNA functionality. HEK 293T cells were transfected with FBXO7 and either empty control vector or the functional FBXO7 shRNA. After lysis the samples were subjected to immunoblotting with the anti-Myc antibody. The 14-3-3β antibody served as loading control. **(D)** Representative images of SH-SY5Y cells transfected at DIV1 with either control or FBXO7 shRNA vectors together with OCT-GFP plasmid serving as mitochondrial marker. The cells were fixed and stained at DIV4. Magnification: 60x. Scale bar = 100 μm. **(E)** Western blotting of SH-SY5Y cell lysates of different passages using endogenous FBXO7 antibody and the 14-3-3β as loading control. **(F)** Quantification and statistical analysis of minimum 100 cells per condition with their mitochondria characterized as either tubular in appearance, globular or fragmented, using one-way ANOVA after normalization (N=3; mean + s.e.m.)

3.3.4. MAP1B LC1 is expressed in cortical neurons at least from P4-P8

Since we characterized MAP1B LC1 as a putative interactor to FBXO7, I went on to study and compare the expression patterns and functions of MAP1B LC1 in cortical and immortalized SH-SY5Y neurons to see if I can find a common pathway for these two novel interactors.

The exact window of expression of MAP1B LC1 has never been clearly defined. It is known to be highly expressed at the peak of axonal growth and synaptic guidance, but the levels of expression fall off as the neurons mature (Viereck et al., 1989). In order to better define the timing of expression of MAP1B LC1, I cultured P0 mouse cortical neurons and fixed them at different time points. I then stained them for endogenous MAP1B LC1 and observed that at all three time points- DIV4, 6 and 8 there was a clear signal for the protein's expression in the cytoplasm, clearly staining the neurites as well **(Fig. 3.8)**.

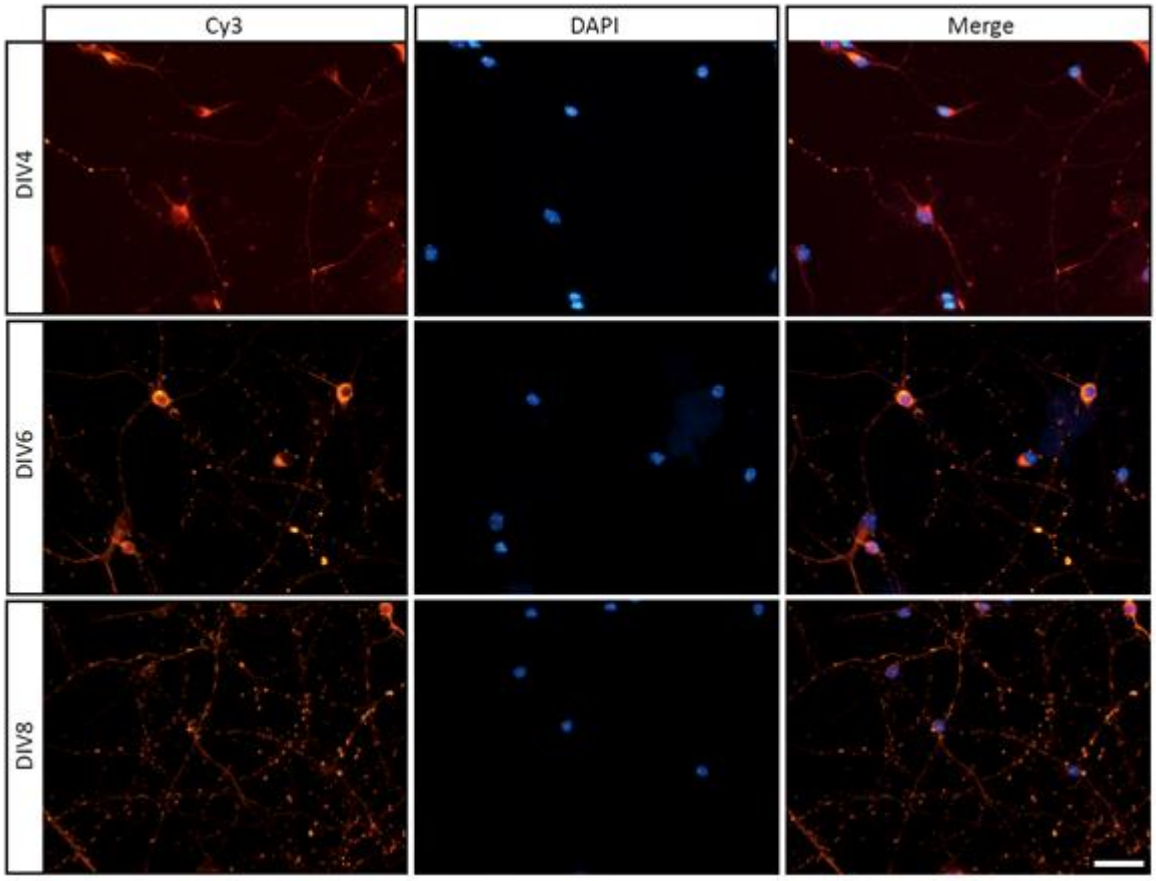

Fig. 3.8 MAP1B LC1 is expressed in cultured mouse cortical neurons at least up to DIV8

Representative images of mouse cortical neurons cultured at P0, and fixed at either DIV4, 6 or 8. The cells were then subjected to immunocytochemical staining using anti MAP1B LC1 antibody and then Cy3 as secondary antibody together with DAPI. Magnification: 60x. Scale bar = 20 μm.

3.3.5. MAP1B LC1 knockdown in SH-SY5Y cells does not lead to increased fragmentation of mitochondria

MAP1B LC1 has been linked primarily with axonal growth and guidance (Matus, 1988) In addition, it has been recently found to play a role in stress-mediated mitochondrial functionality (Yonashiro et al., 2012) and MAP1B has been shown to regulate the retrograde mitochondrial transport through the axon (Jimenez-Mateos et al., 2006). Together with the fact that MAP1B LC1 strongly interacts with FBXO7, I asked if MAP1B LC1 alone has influence on the mitochondrial maintenance. To check that, I transfected SH-SY5Y cells with control vectors and functional MAP1B LC1 shRNA that I had synthesized previously **(Fig. 3.9 C)**. Similarly to the experiments in **Section 3.3.3**, I used OCT-GFP as mitochondrial marker and after staining I categorized the mitochondria of a minimum of 100 cells as either having tubular, globular or fragmented appearance. I detected no change in the number of cells with fragmented or globular

mitochondria, but I saw fewer cells with healthy and tubular mitochondria in the knockdown condition in comparison to the control MAP1B LC1 shRNA **(Fig. 3.9 A-B)**. Interestingly, when I checked for endogenous expression of MAP1B LC1, I could not detect any signal in the SH-SY5Y cells, possibly due to the fact that the antibody does not recognize the human antigen **(Fig. 3.9 D)**.

In summary, FBXO7 lead to increase in fragmented mitochondria in HEK 293T cells but the knockdown of FBXO7 and MAP1B LC1 resulted in none or only slight decrease in tubular organelles in neuroblastoma SH-SY5Y cells.

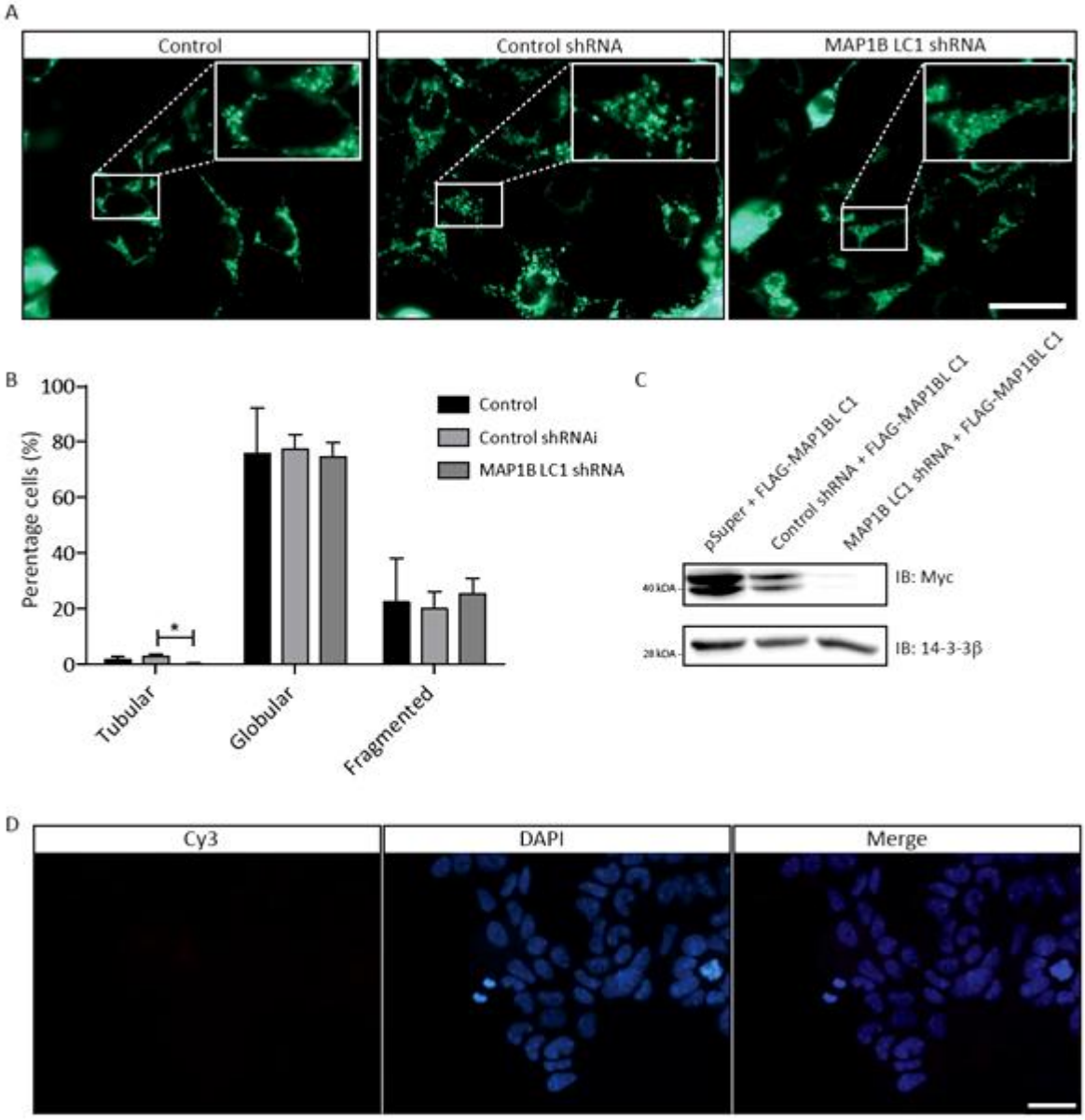

Fig. 3.9 Mitochondrial morphology of SH-SY5Y is largely unaffected after knockdown of MAP1B LC1

(A) Representative images of SH-SY5Y cells transfected at DIV1 with either control or MAP1B LC1 shRNA vectors together with OCT-GFP plasmid serving as mitochondrial marker. The cells were fixed and stained at

DIV3. Magnification: 60x. Scale bar = 20 μm. **(B)** Quantification and statistical analysis of minimum 100 cells per condition with their mitochondria characterized as either tubular in appearance, globular or fragmented, using one-way ANOVA after normalization (N=3,*P<0.5; mean + s.e.m.) **(C)** Proof for the MAP1B LC1 shRNA functionality. HEK 293T cells were transfected with MAP1B LC1 and either empty control vector or the functional MAP1B LC1 shRNA. After lysis the samples were ran on SDS-PAGE and subjected to immunoblotting with the anti-FLAG antibody. 14-3-3β antibody served as loading control. **(D)** Representative images of SH-SY5Y cells, fixed and stained using anti MAP1B LC1 antibody as primary and Cy3 as secondary antibody together with DAPI at DIV3. Magnification: 60x. Scale bar = 20 μm.

3.4. *In vivo* analysis of the role of FBXO7 in the neocortex and the pyramidal tracts

Systemic loss of FBXO7 was shown to lead to a severely detrimental phenotype, most notably decreased body size and survivability (Vingill et al., 2016). The *Fbxo7*$^{-/-}$ mice would not live longer than 25 days and the mean age of death is 18 days, making further analysis on these mice difficult (Vingill et al., 2016). In order to gain a better insight into the effects of FBXO7 in the nervous system, different mouse lines were generated previously in the lab, targeting the deletion of FBXO7 to different brain areas and cell types. The NEX-Cre/*Fbxo7*$^{fl/fl}$ mouse line has the Cre recombinase expressed under the neuronal basic helix-loop-helix (NEX) protein, allowing for the spatial control of *Fbxo7* deletion (Goebbels et al., 2006; Vingill et al., 2016). Thus, the *Fbxo7* is deleted from the neocortex and hippocampus- more specifically, the pyramidal neurons of the dorsal telencephalon and the mossy and granule cells in the dentate gyrus, sparing interneurons, oligodendrocytes and astrocytes (Goebbels et al., 2006). These mice survived much longer, and the body weight at 2 months of age was comparable to their wild type littermates allowing for further motor and behavior studies (Vingill et al., 2016).

Genotyping analysis of the NEX-Cre/*Fbxo7*$^{fl/fl}$ was performed on regular basis to ensure setting of the correct breedings and experimental setup **(Fig. 3.10 A-B)**. The NEX-Cre and the *Fbxo7*$^{fl/fl}$ mice were used as controls, since the NEX-Cre mice lack the floxed *Fbxo7* allele or the *Fbxo7*$^{fl/fl}$ mice would lack expression of the Cre-recombinase respectively rendering both genotypes to express FBXO7.

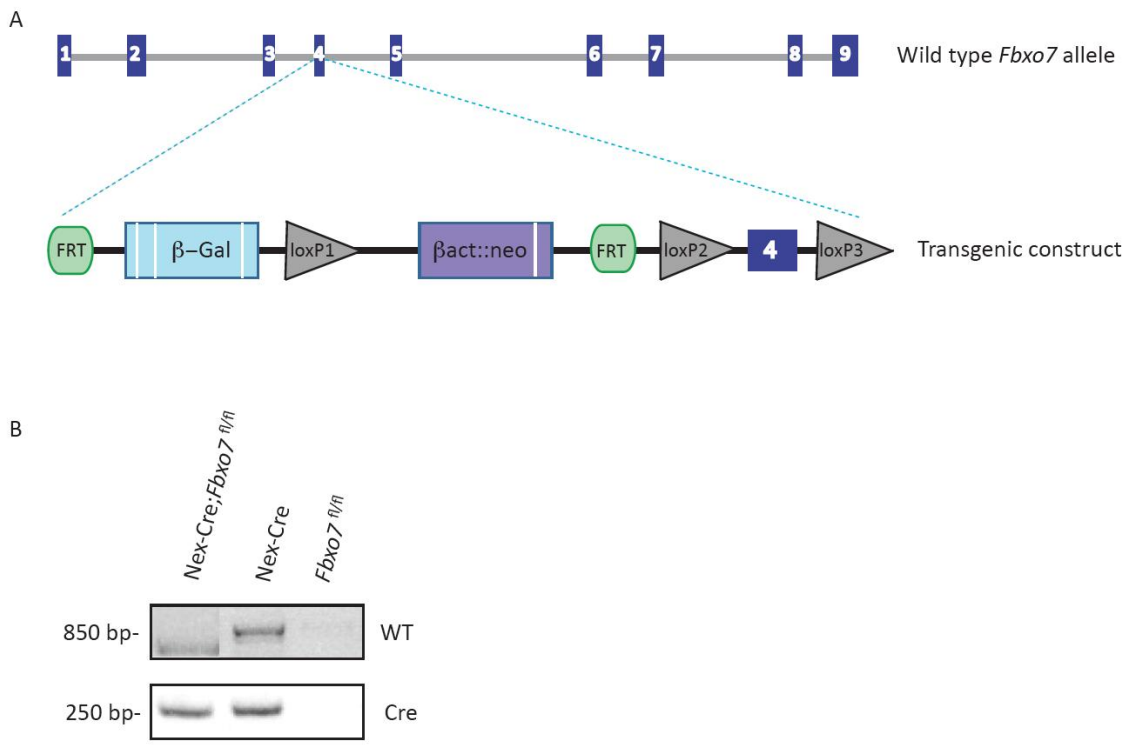

Fig. 3.10 Transgenetic mapping of the *Fbxo7*$^{fl/fl}$ construct.

(A) Schematics of the wild type allele, containing nine exons, and the insertion of the transgenic construct through homologous recombination that leads to the truncation of the protein. The construct contains FRT1 and FRT2 sites, used to excise the β-galactosidase (LacZ reporter) and the β-actin::neomycin selection cassette, as well as loxP sites flanking exon 4. **(B)** Genotyping PCR of the NEX-Cre;*Fbxo7*$^{fl/fl}$, where the presence of the NEX-Cre was detected using Cre forward and reverse primers, and the presence or absence of transgenic allele was tested by using the wildtype primers (representative image was kindly provided by Sabitha Joseph).

3.4.1. Terminal deoxynucleotidyl transferase dUTP nick end labeling assay (TUNEL) analysis reveals no increase in cellular apoptosis

Neuronal death is the hallmark for neurodegenerative diseases. Since neuronal loss was observed in the conventional knockout model, I wondered if I would also observe similar phenotype in the NEX-Cre;*Fbxo7*$^{fl/fl}$ mice at 8 weeks of age, since they already exhibited a motor phenotype at this stage (Vingill et al., 2016). To answer this question, I performed TUNEL assay, which takes advantage of the fact that cells undergoing apoptosis have their DNA nicked and fragmented and the terminal deoxynucleotidyl transferase (TdT) binds to the 3'-OH of the fragmented DNA, further incorporating biotinylated deoxyuridines to the sites of breakage (Gavrieli et al., 1992). These can then be further labeled and visualized by using chromogens such as DAB. I then went on to manually and in blinded manner count the number of apoptotic nuclei,

which appeared brown in color. In total, three mice per genotype were compared for biological triplication as well as three technical replicates for each brain. I then compared the number of apoptotic cells in the cortex, the hippocampus and the cerebellum, where the latter served as control, since FBXO7 is expressed in the cerebellum in the NEX-Cre;*Fbxo7*$^{fl/fl}$ mice. I saw a slight tendency for an increase in apoptosis in the NEX-Cre;*Fbxo7*$^{fl/fl}$ mice in all three brain regions tested, however this is statistically insignificant because of the very low count of apoptotic cells at this age **(Fig. 3.11 A-C)**. I also measured the total cerebellar and cortical area of all three mouse genotypes with a total of 6 animals tested per genotype. After running one-way ANOVA statistical test, I saw that the cerebellar area remains comparable within all three genotypes, but there is significant decrease in the cortical area when comparing the NEX-Cre and the NEX-Cre;*Fbxo7*$^{fl/fl}$ mice, and only a tendency when comparing the NEX-Cre;*Fbxo7*$^{fl/fl}$ mice with the *Fbxo7*$^{fl/fl}$ **(Fig. 3.11 D)**. These data indicate that albeit there is no cellular death ongoing in 8-week old animals, the total cortical size is decreased in the conditional knockout mice.

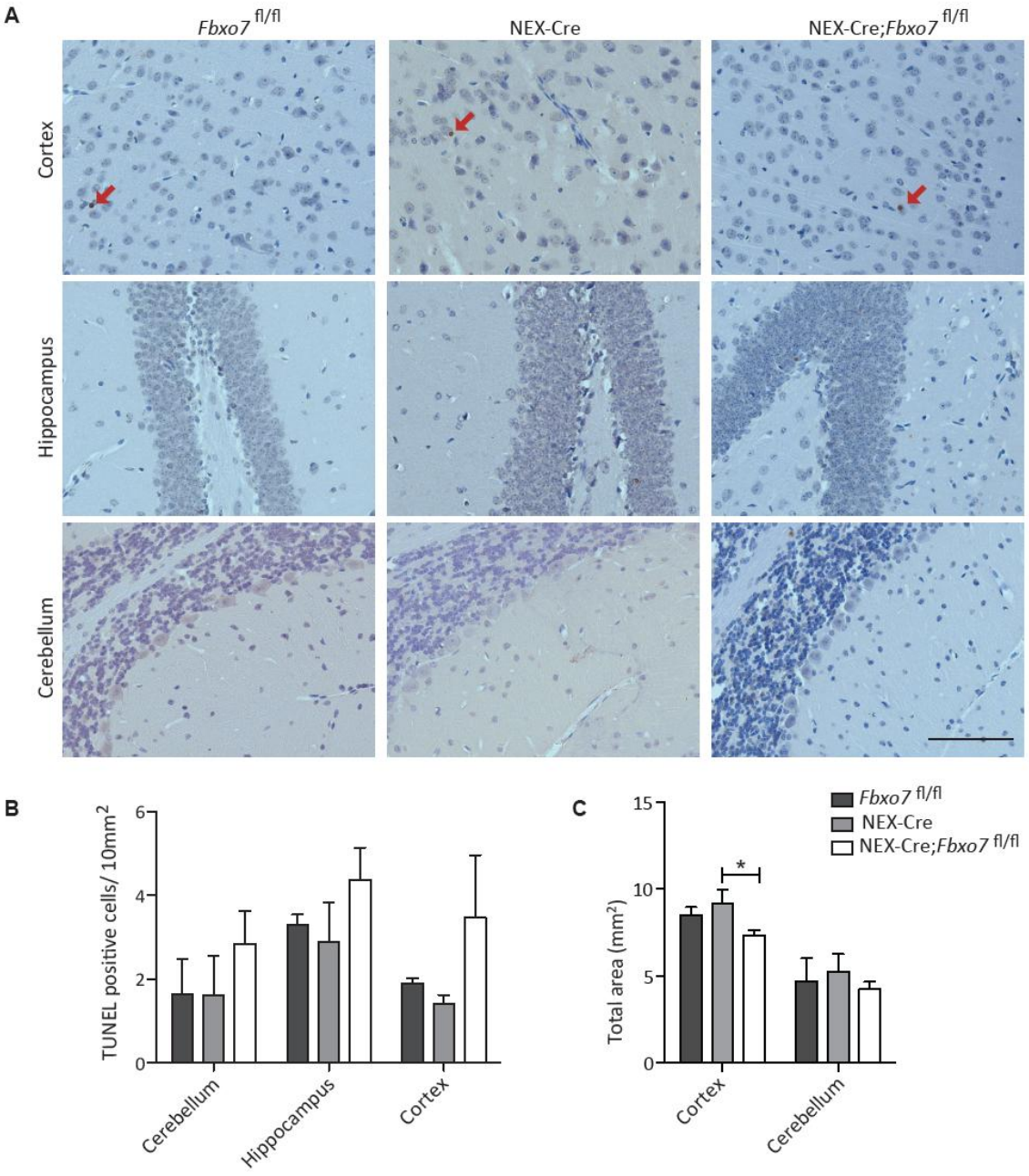

Fig. 3.11 There is no increased level of apoptosis in the cortex of NEX-Cre;*Fbxo7*$^{fl/fl}$ mice

(A) Immunohistological representative images from the cerebellum, hippocampus and cortex of 5 μm thick sagittal sections from 8-weeks old NEX-Cre;*Fbxo7*$^{fl/fl}$ and control mice. The red arrows point at nuclei that have stained positive with the TUNEL assay detection kit. Magnification: 40x. Scale bar = 100 μm. **(B)** Quantification of the TUNEL assay: the total number of apoptotic cells was counted and normalized to the area of interest and subjected to statistical analysis using the One-way ANOVA test (N=3; mean + s.e.m.) **(C)** Quantification of the total cortical or cerebellar area (mm^2) of the NEX-Cre;*Fbxo7*$^{fl/fl}$, Nex-Cre and *Fbxo7*$^{fl/fl}$ mice. One-way ANOVA (N=6, *P<0.5; mean + s.e.m.)

3.4.2. The NEX-Cre;*Fbxo7*$^{fl/fl}$ mice present with increased astrogliosis and inflammation

Gliosis is a process that occurs after a brain injury, and its main components- astrogliosis and microgliosis have been known to be dependent of each other in neurodegenerative diseases (Tong et al., 2015). In order to test whether there will be similar pathological signs in the NEX-Cre;*Fbxo7*$^{fl/fl}$ mice, I subjected paraffin brain sections to either glial fibrillary acidic protein (GFAP) or Ionized calcium-binding adapter molecule 1 (Iba1) immunohistological stainings. The GFAP was used as a marker for astrogliosis, and the Iba1 was used as a marker for inflammatory response, since these antibodies stain the astrocytes or microglia respectively. The NEX-Cre;*Fbxo7*$^{fl/fl}$ mice showed significantly increased signal corresponding to GFAP positive cells, both in the cortex as well as in the cerebellum **(Fig. 3.12 A,C)**. The count of Iba1 positive cells was also significantly greater in the NEX-Cre;*Fbxo7*$^{fl/fl}$ compared to their littermates specifically in the cortex, where the count remained comparable within the cerebellum **(Fig. 3.12 B,D**). The increase in signal of these markers present in the immunohistological sections indicate that there has been a major brain trauma and that the immune and the supporting cells have been activated as a response to it.

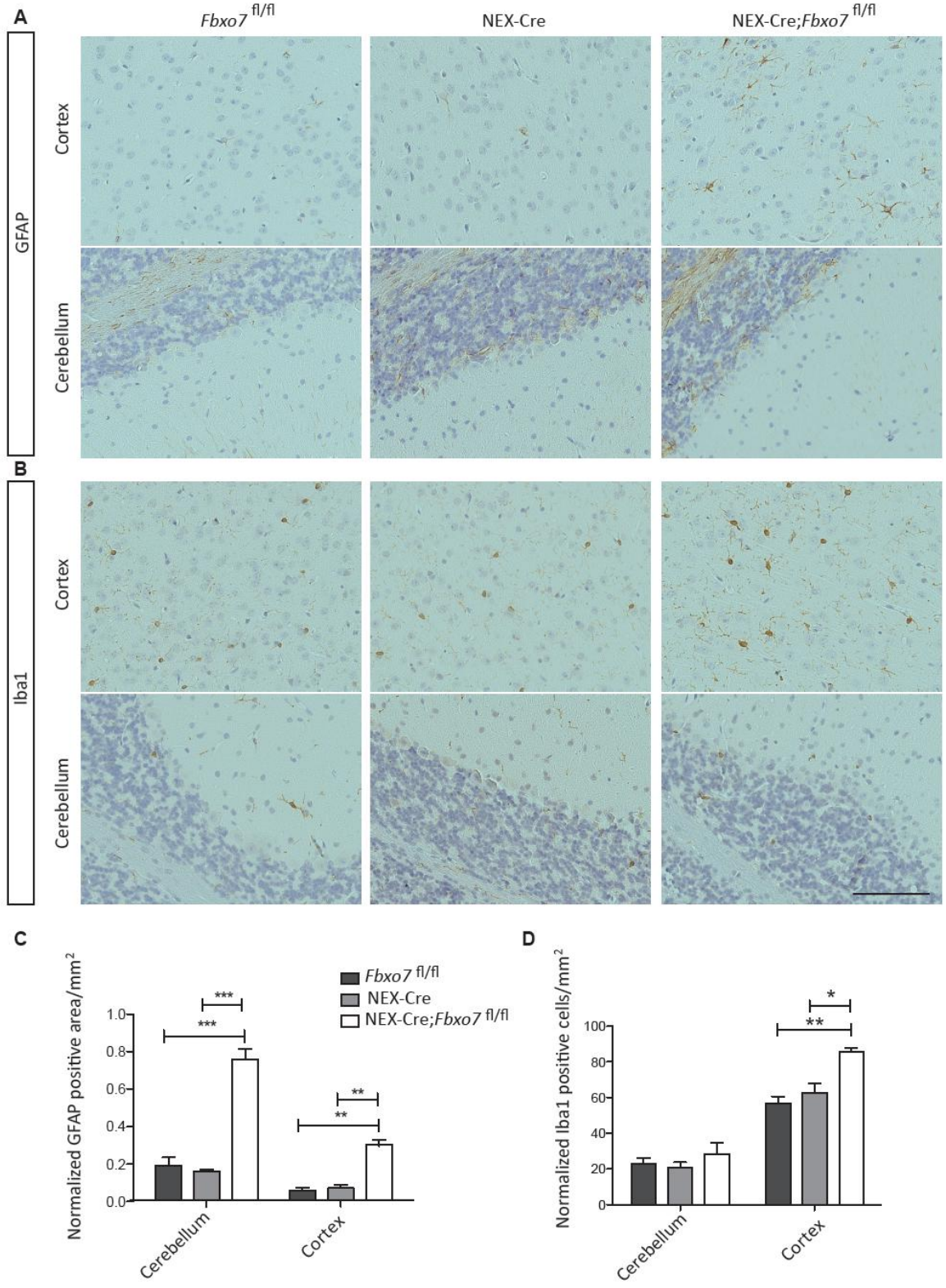

Fig. 3.12 The NEX-Cre;*Fbxo7*$^{fl/fl}$ show increased astrogliosis and inflammatory cell number in the cortex

(A) Immunohistological staining using anti-GFAP antibody on 5 µm sagittal brain sections. The representative images are taken from cerebellar and cortical areas from the NEX-Cre;*Fbxo7*$^{fl/fl}$, NEX-Cre and

the *Fbxo7*$^{fl/fl}$ mice. Magnification: 40x. Scale bar = 100 μm. **(B)** Immunohistological staining using anti-Iba1 antibody. The representative images are taken form cerebellar and cortical areas form the NEX-Cre;*Fbxo7*$^{fl/fl}$, NEX-Cre and the *Fbxo7*$^{fl/fl}$ mice. Magnification: 40x. Scale bar = 100 μm. **(C)** Quantification and statistical analysis of GFAP positive area, comparing the cortex and cerebellum within all three genotypes using One-way ANOVA (N=3; **P<0.01, ***P<0.001, mean + s.e.m.) **(D)** Quantification and statistical analysis of Iba1 positive cells and normalized to the area of interest and subjected to statistical analysis using the One-way ANOVA test (N=3, *P<0.5; **P<0.01, mean + s.e.m.)

3.4.3. NEX-Cre;*Fbxo7*$^{fl/fl}$ mice have intact pyramidal tracts with no neurofilamentous inclusions

Axonal injury causes a decrease in expression level of the Neurofilament medium (NFM) protein (Bisby et al., 1995). This has also been observed in neurodegenerative diseases including Parkinson's Disease together with deposition of neurofilaments forming neurofilamentous inclusions (Julien and Mushynski, 1998). Furthermore, neurofilaments are the major constituent of the cytoskeleton comprising the axon cylinder (Black and Lee, 1988). I therefore subjected the brain sections to NFM staining, and saw no visible difference in the pyramidal tracts of the NEX-Cre;*Fbxo7*$^{fl/fl}$ mice in comparison to the control groups **(Fig. 3.13 A)**.

The majority of patients with the parkinsonian pyramidal syndrome have reported pyramidal tract signs **(Table 1.1)** (Di Fonzo et al., 2009). I therefore stained for the amyloid precursor protein (APP) on the brain paraffin sections of the 8 week-old animals of the three genotypes, to check the integrity of the tracts. APP is synthesized in the soma and transported to the axonal terminus, where in case of axonal injury it will be accumulated at the point of cytoskeletal aberration and appears as bulbous structures or axonal swellings (Sherriff et al., 1994). The knocking out of *Fbxo7* from the forebrain had no visible effect on the pyramidal axonal tract structure **(Fig. 3.13 B)**.

These results imply that the pyramidal tract symptoms are not represented in the gross histological analysis of the 8 week-old NEX-Cre;*Fbxo7*$^{fl/fl}$ mice, raising the possibility that these aberrations may become detectable at later points of the disease progression.

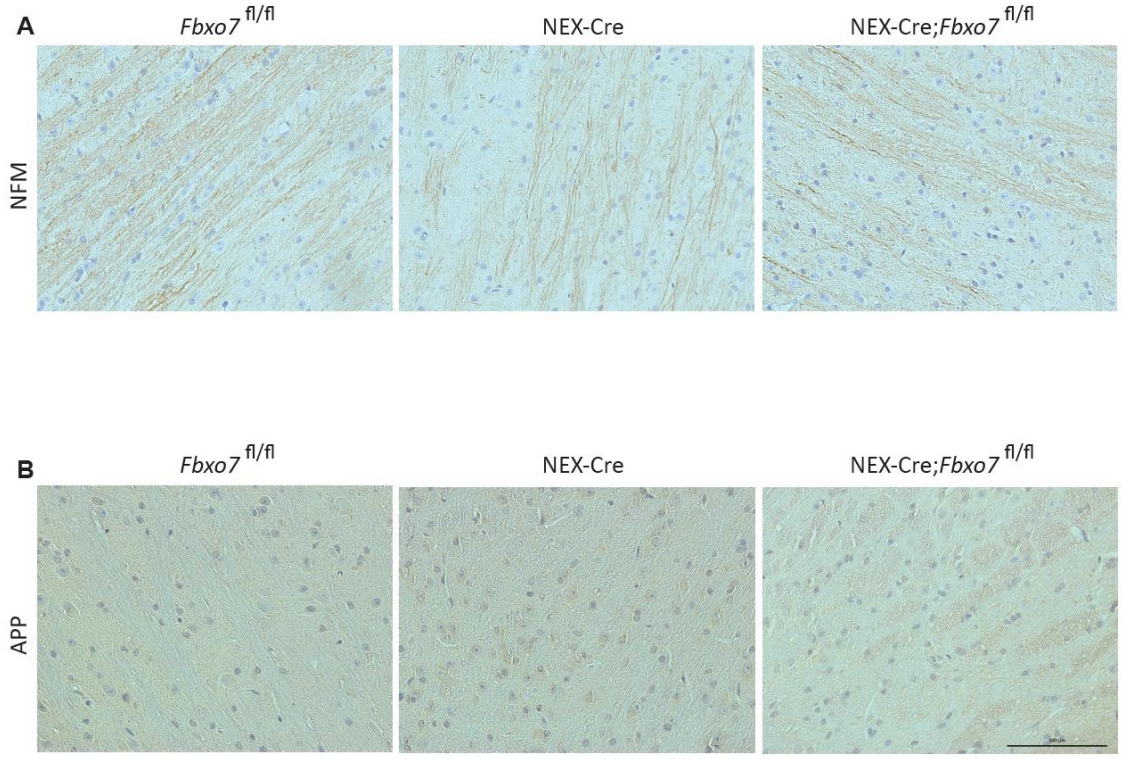

Fig. 3.13 Axons in the pyramidal tract remain unaltered and healthy

(A) Immunohistological staining using anti-NFM antibody on 5 μm sagittal brain sections of NEX-Cre;*Fbxo7*$^{fl/fl}$ **,** NEX-Cre and the *Fbxo7*$^{fl/fl}$ mice. The representative images are taken from the ventral pyramidal tract area. Magnification: 40x. Scale bar = 100 μm. **(B)** Immunohistological staining using anti-APP antibody on 5 μm sagittal brain sections of NEX-Cre;*Fbxo7*$^{fl/fl}$ **,** NEX-Cre and the *Fbxo7*$^{fl/fl}$ mice. The representative images are taken from the ventral pyramidal tract area. Magnification: 40x. Scale bar = 100 μm.

3.4.4. NEX-Cre;*Fbxo7*$^{fl/fl}$ mice do not present with Lewy body pathology

Hallmark of idiopathic PD is the presence of Lewy body inclusions whose main constituent is α-synuclein (Forno and Norville, 1976). I therefore screened for the presence of proteinase K resistant α-synudein aggregations and saw no difference in the morphology of the brains of the NEX-Cre;*Fbxo7*$^{fl/fl}$ compared to their littermates **(Fig. 3.14)**. These data indicate that deletion of *Fbxo7* in the forebrain does not induce Lewy body inclusions.

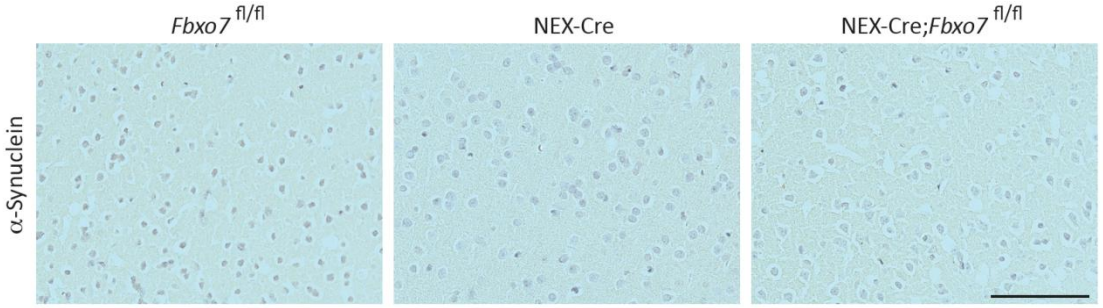

Fig. 3.14 There is no Lewy body pathology in the NEX-Cre;*Fbxo7*$^{fl/fl}$ mice

Immunohistological staining using anti-α-synuclein antibody on 5 μm sagittal pre-digested with Proteinase K brain sections of NEX-Cre;*Fbxo7*$^{fl/fl}$, NEX-Cre and the *Fbxo7*$^{fl/fl}$ mice. The representative images are taken form the cortex. Magnification: 40x. Scale bar = 100 μm

4. Discussion

Autosomal recessive mutations in the *Fbxo7* gene were first discovered and related to the Parkinsonian-pyramidal syndrome later known as late onset parkinsonism by Shojaee et al. in 2008 (Shojaee et al., 2008). Their findings were then further substantiated and up to date there are about 6 well-studied kindreds that harbor a variety of mutations in the *Fbxo7* gene. Almost a decade later, scientists have managed to link FBXO7 with major players in the mitophagy pathway, as well as the ubiquitin-proteasome system, which are in turn considered to be at the forefront of neurodegenration. Even though only a small fraction of the PD cases are genetically inherited, we study FBXO7, its interactome, its functions in cell and tissue to hopefully improve our understanding of the causes of neurodegeneration and pathological progression of idiopathic and non-idiopathic cases of PD. The main aim of this study is to unravel the molecular mechanisms involving FBXO7 and its interaction partners by the use of genetics, biochemistry, analytical chemistry and histology. Amongst the many interaction partners for FBXO7 that we identified through quantitative mass spectrometry and yeast-two-hybrid assay preformed previously in the lab, I focused on the light chain of the microtubule associated protein 1B (MAP1B LC1). I went on to characterize the type of interaction between these two proteins, and found that it is independent of the SCF-complex formation. I further tested how loss-of-function of both proteins would affect the mitochondrial morphology in cells and observed slight changes in this read-out. Finally, I also studied the consequences of the loss of FBXO7 from the neocortex, and found an up-regulation of astro- and microglial markers, indicative of generalized tissue response for brain injury in the absence of apoptosis. These results help to expand our knowledge on FBXO7 and the molecular mechanism for pathology in neurodegenerative disorders.

4.1. FBXO7 is a cytoplasmic protein

One important question to be answered when studying a protein is its localization within the cell. Zhao *et al*. overexpressed wild type untagged FBXO7 in HEK 293T, SH-SY5Y cells and mouse primary hippocampal neurons and concluded that FBXO7 localized predominantly to the nucleus, especially in the immortalized cell lines (Zhao et al., 2011). Arguably, the representative figures for the wild type FBXO7 overexpression in the hippocampal neurons clearly depicts FBXO7 in the cytoplasm as well (Zhao et al., 2011). They also obtained patients' fibroblasts harboring the T22M mutation as well as healthy control fibroblasts and examined for endogenous FBXO7 protein, where they saw cytoplasmic signal for the T22M mutation and diffuse nuclear signal in the wild type fibroblasts, reasoning that intact N-terminus is required for nuclear localization of

FBXO7 (Zhao et al., 2011). Interestingly, the specificity of the antibody they used was tested using western blotting, even though the results were obtained thought immunocytochemical analysis (Zhao et al., 2011). Our research group wanted to further substantiate these findings by performing a subcellular fractionation of cortical lysates, since the available commercial antibodies were not able to detect endogenous FBXO7 by immunocytochemistry. The subcellular fractionation analysis of *Fbxo7*$^{-/-}$, *Fbxo7*$^{+/-}$ and *Fbxo7*$^{+/+}$ of P18 brain lysates showed clearly that FBXO7 localizes to cytoplasmic fraction and not the nuclear fraction (Brockelt, 2015). I went on to further validate the cytoplasmic localization of FBXO7 in neurons as well as in HEK 293T and SH-SY5Y cells by immunocytochemistry. I saw that nearly all healthy cells expressed the FBXO7 protein in the cytoplasm. This observation is also in line with the subcellular localization of FBXO7 and also, almost all of the known functions and interactors of FBXO7 within neurons such as HURP, PINK1, Parkin, Skp1, PSMA2, Tomm20 etc. are found in the cytoplasm (Hsu et al., 2004; Nelson et al., 2013; Teixeira et al., 2016; Vingill et al., 2016). These observations are further supported by the findings of Nelson and Laman who showed in U2OS cells that FBXO7 localized to the cytoplasm but is shuttled to the nucleus specifically when the cells entered the G1/S transition (Nelson and Laman, 2011). This shuttling might be due to the fact that FBXO7 plays an important role in cell cycle regulation in mitotic cells such as haematopoietic stem cells and fibroblasts by acting as an assembly scaffold for the cydin D/Cdk6 complex which are in turn G1/S transition state regulators (Cheng et al., 1999; Meziane el et al., 2011). However, the vast majority of neurons are post-mitotic cells that are in their resting G_0 phase, further on validating all findings that FBXO7 localizes to the cytoplasm.

4.2. FBXO7 can be linked to a plethora of cellular mechanisms.

As previously mentioned, FBXO7 has several well established interaction partners in relation to its role in neurodegeneration- PINK1, Parkin and Tomm20 on one hand (Burchell et al., 2013; Teixeira et al., 2016) and Skp1 together with different subunits of the proteasomal holoenzyme on the other (Cenciarelli et al., 1999; Vingill et al., 2016). These proteins can be grouped into two main categories, namely those being part of the mitochondrial maintenance machinery or of the ubiquitin proteasome system (UPS) (Nelson et al., 2013). Upon performing a quantitative mass spectrometry analysis in collaboration with the Proteomics Facility at the RWTH Aachen, we obtained the interactome of FBXO7. I focused on a total of 88 targets omitting candidates whose high enrichment readouts could be due to contamination such as keratin. These proteins could be then arranged in six groups according to their function in the cell. Apart from the proteasomal degradation and mitochondrial maintenance, the mass spectroscopy data

also yielded a list of proteins involved in DNA repair, formation of nuclear pores, nuclear pore transport, microtubular organization and dynamics as well as endoplasmic reticulum (ER) to Golgi non-clathrin mediated vesicular transport. Since FBXO7 does shuttle between the nucleus and the cytoplasm, regulates the cellular cycle, and recently was found to be a putative up-stream activator of the DNA-repair enzyme PARP, the increase in signal for proteins and protein complexes involved in these processes does not come as a surprise (Cheng et al., 1999; Delgado-Camprubi et al., 2017; Meziane el et al., 2011; Nelson and Laman, 2011). Furthermore, I confirmed the mass spectrometry data regarding two of the novel interactors in a cell-based co-immunoprecipitation analysis. Interestingly, the involvement in cytoskeleton organization and remodeling as well as vesicular transport might point to novel functions of FBXO7. One explanation for the abundance of the latter can be the fact that Skp1 binds to the F-box protein Rcy1 to mediate early endosome to *trans*-Golgi protein recycling and since the Skp1 presence in the mass spectromety analysis was very high, it is possible that some of the Skp1 was also bound to Rcy1 (Galan et al., 2001). However, since many of the putative interaction partners are involved in ER to Golgi trafficking, this interaction can be considered as novel and as the starting point of a new line of research.

A very dominant family of proteins that are being represented in the mass spectroscopy data is the tubulin family. The closest reports associating FBXO7 and the cytoskeleton came from a large scale *in vitro* ubiquitination experiment, fishing for novel substrates of FBXO7-SCF where 10 of the 338 substrates were localized at the microtubular organizing center (Teixeira et al., 2016). The microtubule associated protein 1B light chain1 (MAP1B LC1) was identified as novel putative interactor to FBXO7 as shown in a yeast-two hybrid analysis performed previously in our laboratory (Brockelt, 2015). These discoveries unlocked the possibility to study the effect of the cytoskeleton-microtubule-UPS triangle that may ultimately contribute to neurodegeneration.

4.3. The MAP1B LC1-FBXO7 interaction results in non FBXO7-SCF-dependent functional modification

In his thesis, Dr. Brockelt confirmed the interaction between FBXO7 and the MAP1B LC1 of the yeast-two-hybrid assay also through cell-based co-immunoprecipitation analysis (Brockelt, 2015). I repeated his experiments, showing that FBXO7 indeed associates with MAP1B LC1. Since the light chains of MAP1A and MAP1B are highly homologous, Dr. Brockelt reasoned that FBXO7 should be able to interact with the light chains of the MAP1 family (Langkopf et al., 1992) (Brockelt, 2015). This was shown for the MAP1A LC2 by Dr. Brockelt and further confirmed by my results (Brockelt, 2015). In order to include the MAP1S LC to FBXO7's interactome, I generated a

pCMV10-3xFLAG-MAP1B LC1 expression vector, and proved the interaction also in a cell-based co-immunoprecipitation analysis. The interaction site was found to lie somewhere between amino acids 78 and 180 of the FBXO7 protein (Brockelt, 2015). There are two interaction partners that use this amino acid stretch for their association with FBXO7- namely the PINK1, an important regulator of mitophagy, and the Cdk6 (Burchell et al., 2013; Laman et al., 2005). Intriguingly, I found that from all known pathological mutations of FBXO7, the M115I single nucleotide polymorphism (SNP), located within this interaction sequence, results in weaker interaction strength between FBXO7 and MAP1B LC1. However, this can be due to the fact that this interaction did not result in the usual stabilization of MAP1B LC1 by FBXO7 (as discussed in the following paragraph), and that there was less protein for the co-immunoprecipitation analysis, thus weaker band is apparent on the western blot. This SNP lies within the FBXO7-PINK1 interaction domain, suggesting that the association between MAP1B LC1 and FBXO7 may be important for the maintenance of proper mitochondrial quality control. It is interesting to note that the methionine required for initiation of translation of FBXO7 isoform 3 is located at this site, and this M115I SNP would result in abolished expression of isoform 3 (Nelson et al., 2013). Unfortunately, the M115I SNP is the least excessively studied *Fbxo7*-related pathological variation and it is mostly associated with haematopoiesis, and further analysis is necessary in order to uncover the significance of this interaction (Chen et al., 2014; Ding et al., 2012; Soranzo et al., 2009; van der Harst et al., 2012).

The co-expression of FBXO7 and MAP1B, consistently resulted in a much stronger western blot signal compared to MAP1B LC1 co-expressed with the empty vector. The band was also slightly stronger but not as dramatic when MAP1B LC1 was co-expressed with the ΔF-box FBXO7 construct that is devoid of its ligase activity. These results might indicate that since FBXO7 is a main component of the FBXO7-SCF-ubiquitin ligase complex, the interaction leads to a functional modification of MAP1B LC1 and we reasoned that most probably, this modification is ubiquitination (Cenciarelli et al., 1999). To check this hypothesis, I performed cell-based ubiquitination assay, but did not observe the typical smear in the condition where I overexpressed both proteins in comparison to controls. This observation points to the conclusion that MAP1B LC1 does not get polyubiquitinated by FBXO7. Furthermore, the heavy immunoglobulin chains of the primary antibody may have hidden a signal that could correspond to a mono-ubiquitination of MAP1B LC1. Instead of long chains of ubiquitin with different lengths, resulting in a smear, in mono-ubiquitination the protein gets modified by only a single ubiquitin molecule which would appear as a single band on the western blot analysis. To test for this possibility, I checked whether the interaction between MAP1B LC1 and FBXO7 indeed depends on the formation of the SCF

complex. I used cullin1 as a protein of choice to probe whether MAP1B LC1 is capable to pull down FBXO7 together with the rest of the components of the SCF complex. Indeed, MAP1B LC1 was not able to recruit the FBXO7 proteins associated with the Skp1-cul1 complex, but could recruit FBXO7 that are not a part of the E3 ubiquitin ligase complex. These data imply that FBXO7 and MAP1B LC1 interact in a non-SCF manner, resulting in a functional modification of MAP1B LC1 other than ubiquitination. It is interesting to note that MAP1B LC1 gets post-translationally modified through heavy phosphorylation by different kinases, two of which are of particular significance to this study. One of them is the LRRK2 also known as PARK8 but the functional significance of this modification remains to be determined (Chan et al., 2014). The other kinase to phosphorylate MAP1B is the glycogen synthase kinase 3 β (Gsk3β), and this phosphorylation has a major role in the regulation of microtubular dynamics in the growth cone especially during axonal pathfinding and regeneration (Goold et al., 1999; Liz et al., 2014). Intriguingly, Gsk3β was also found to be a novel FBXO7-SCF interactor, leading to the ubiquitination of Gsk3β, but the functional significance of this interaction was not further examined (Teixeira et al., 2016). Gsk3β thus becomes the only known link between FBXO7 and MAP1B prior to the results obtained by Dr. Brockelt. Another known modification of the MAP1B LC1 is its S-nitrosylation in the event of excessive intracellular nitric oxide (Yonashiro et al., 2012). This modification in turn promotes the mitochondrial MAP1B LC1 ubiquitination by the mitochondrial ubiquitin ligase MITOL, leading to its degradation (Yonashiro et al., 2012).

4.4. Implications of FBXO7 and MAP1B LC1 in cellular morphology and mitochondrial homeostasis

To further deepen our understanding about the functional importance and the cellular mechanisms in which FBXO7 and MAP1B LC1 interaction plays a role, I prepared lysates of cells overexpressing these proteins and the lysates were subjected to a mass spectrometry analysis at the RWTH Aachen Proteomics Facility. The results yielded a functional map with a total of 26 candidates, representing up-regulated and/or overly stabilized proteins as a result of the MAP1B LC1 and FBXO7 interaction in comparison to MAP1B LC1 overexpressed with empty vector as control condition. These can be grouped in four major cellular niches, partially overlapping with the interactome network for FBXO7: DNA repair and transcription machinery, the UPS, the microtubular cytoskeleton, and mitochondrial homeostasis. The fact that the interaction resulted in overrepresentation of DNA-related proteins was quite striking, since there is no data linking MAP1B LC1 with these cellular complexes. It is possible that whilst performing its duties in the cellular cycle control and DNA repair and transcription, FBXO7 associates with the cytoskeleton to

facilitate the transport of proteins and DNA. However, further research will be required to unravel the mechanism in which FBXO7 and MAP1B LC1 act together to ensure proper DNA repair and transcription.

MAP1B carries the history of its discovery within its name- it was revealed because it would co-purify with microtubules (Bloom et al., 1985). The exact timing of its expression in rat neurons was determined to be highest in neonates, before dropping tenfold between postnatal days 10-20 (Riederer et al., 1986). I wanted to check the expression of MAP1B LC1 in mouse neurons, to make sure that the experiments are conducted in cells that express the protein. Because the available antibody directed against endogenous MAP1B LC1 was unable to detect the protein neither on a western blot nor on cryosections (data not shown), I resorted to mouse cortical primary culture and immunocytochemistry. MAP1B LC1 is still strongly expressed throughout the neurons even after keeping them for 8 days *in vitro* which is consistent with the aforementioned findings.

The main function of MAP1B is to promote axon outgrowth by stabilization of microtubules and regulation of the cytoskeletal assembly during early development (Gonzalez-Billault et al., 2001). My findings however showed no role of FBXO7 in total axonal length, indicating that the functional significance of the MAP1B LC1-FBXO7 interaction takes place in a different context. A less studied function of MAP1B is its role in dendritic morphogenesis, even though MAP1B has been often observed in the dendrites (Bloom et al., 1985; Hirokawa, 1994; Ohyu et al., 1997). One study found MAP1B acting in synergy with MAP2 is indispensable for dendritic outgrowth (Teng et al., 2001). Interestingly, I found that upon knockdown of FBXO7 there was a decrease in the average total dendritic length as well as the average number of dendritic outgrowths from the soma. These findings may provide a functional link between FBXO7 and MAP1B specifically in their role to regulate dendritic density and morphology.

Another group of proteins that were overrepresented in the quantitative mass spec analysis were oxidative-phosphorylation-related proteins, implicating the functional importance of the MAP1B LC1-FBXO7 interaction in mitochondrial homeostasis. Both proteins have been previously linked to mitochondrial health with several lines of evidence relating FBXO7 and mitochondria (Burchell et al., 2013; Teixeira et al., 2016). The earliest findings were paramount, because FBXO7 was found to directly interact with two of the key *PARK* genes *PINK1 (PARK6)* and *Parkin (PARK2)*- the main initiators of mitophagy due to mitochondrial depolarization (Burchell et al., 2013). The authors found that upon mitochondrial depolarization, FBXO7 is translocated to the damaged mitochondria, acting as recruiter of Parkin, which in turn initiates an ubiquitination cascade of

proteins inaugurating mitophagy (Burchell et al., 2013). Moreover, the T22M and the R498X mutations resulted in the inability to recruit Parkin to the organelle and the R378G mutation prevented the ubiquitination of Mitofusin1 (Mfn1) (Burchell et al., 2013). Further research on mitochondrial viability and the Parkinson's disease-related *Fbxo7* mutations revealed that the pathological forms of FBXO7 could aggregate in mitochondria, reducing the mitochondrial membrane potential and leading to increase in reactive oxygen species (ROS) formation and subsequently decreased cell survivability (Zhou et al., 2015). Additional insights into the pathophysiology of cells lacking FBXO7 substantiated the previous importance of FBXO7 in mitochondrial depolarization and ROS increase, stating that these are consequence of the depletion of nicotinamide adenine dinudeotide (NAD^+) in the cell (Delgado-Camprubi et al., 2017). This in turn lead to a reduction of the NADH availability pool that is necessary for the proper complex I and consequently electron transport chain functioning (Delgado-Camprubi et al., 2017). Severe mitochondrial damage would result in the mitochondrial autophagosomal clearance, where mitochondria will have fragmented morphological phenotype (Youle and Narendra, 2011). I used this as readout for potential mitochondrial health and maintenance disruptions in FBXO7 knockdown experiments. Although I observed no difference in mitochondrial morphology between the FBXO7 knockdown and control conditions in SH-SY5Y cells, I saw a significant increase in the number of HEK 293T cells with fragmented mitochondria. This increase appeared to be in a reverse correlation with the number of cells, containing tubular (healthy) mitochondria, indicating that indeed FBXO7 plays role in mitochondrial health in HEK 293T cells.

DJ-1 (PARK7) is found in the mitochondrial matrix and the intermembrane space, and it is recognized as a redox-sensitive molecular chaperone (Shendelman et al., 2004; Zhang et al., 2005). It was also recently found to directly interact with MAP1B, leading to the inhibition of the formation of MAP1B aggregates (Wang et al., 2011). As mentioned in the last paragraph in **Section 4.3**, S-nitrosylation of MAP1B LC1 is a functional modification leading to its selective ubiquitination and degradation of MAP1B LC1 by MITOL and the UPS respectively (Yonashiro et al., 2012). Interestingly, MITOL knockdown caused MAP1B LC1 to accumulate in mitochondria which further induced mitochondrial aggregation and cytotoxicity (Yonashiro et al., 2012). The authors proposed that S-nitrosylation causes MAP1B LC1 to translocate to microtubules thus stabilizing them (Yonashiro et al., 2012). This stabilization may also cause steric hindrance for the binding sites of motor proteins, in turn preventing any transport along the microtubules including mitochondrial transport (Yonashiro et al., 2012). MITOL then serves as a regulator of the microtubular stabilization by causing MAP1B LC1 degradation and reestablishing the normal organellar transport (Yonashiro et al., 2012). This is a proposed mechanism, by which the cell

ensures that all processes are transiently halted in the event of nitric oxide induced cytotoxicity (Yonashiro et al., 2012). In addition, the speed of mitochondrial retrograde transport along the axon is significantly increased in *Map1b*$^{-/-}$ neurons, further implicating that MAP1B may act as a competitor to the motor protein dynein for microtubule-site binding (Jimenez-Mateos et al., 2006). To check if MAP1B LC1 also plays role in mitophagy, I used the same readout as for FBXO7 knockdown, but I only saw significant decrease in the number of cells with tubular mitochondria in MAP1B LC1, which can still serve as a suggestion that MAP1B LC1 has a role in mitochondrial quality control mechanism. Interestingly, upon checking for MAP1B LC1 expression in SH-SY5Y cells, I was unable to detect signal in the immunocytochemical analysis, which can be due to one of the following reasons: either there is no MAP1B LC1 expression present in SH-SY5Y cells, or the antibody recognizes specifically mouse MAP1B LC1 but not its human orthologue. However, since mitochondria did exhibit some response to the knockdown of MAP1B LC1, the latter scenario seems more likely.

These data taken together, might lead to a new possible neurodegenerative model in neurons, in which mitochondria located in the distal end of the axons are unable to translocate into the soma as part of the mitochondrial health maintenance pathways (Miller and Sheetz, 2004). These mitochondria are subjected to high Ca^{2+}, ATP-demand and reactive oxygen species formation, leading to mitochondrial damage **(Fig. 4.1)** (Brookes et al., 2004). In healthy neurons, they are transported back to the soma using microtubular tracks, where they can fuse with lysosomes- the end stage of mitophagy, maintaining a healthy mitochondrial pool **(Fig. 4.1)**. However, it is possible that in neurons lacking FBXO7, MAP1B LC1 gets functionally modified so that it hinders the binding sites for the motor proteins, rendering microtubular transport to a halt **(Fig. 4.1)**. This in turn could lead to accumulation of aberrant and dysfunctional mitochondria, ultimately causing cellular death.

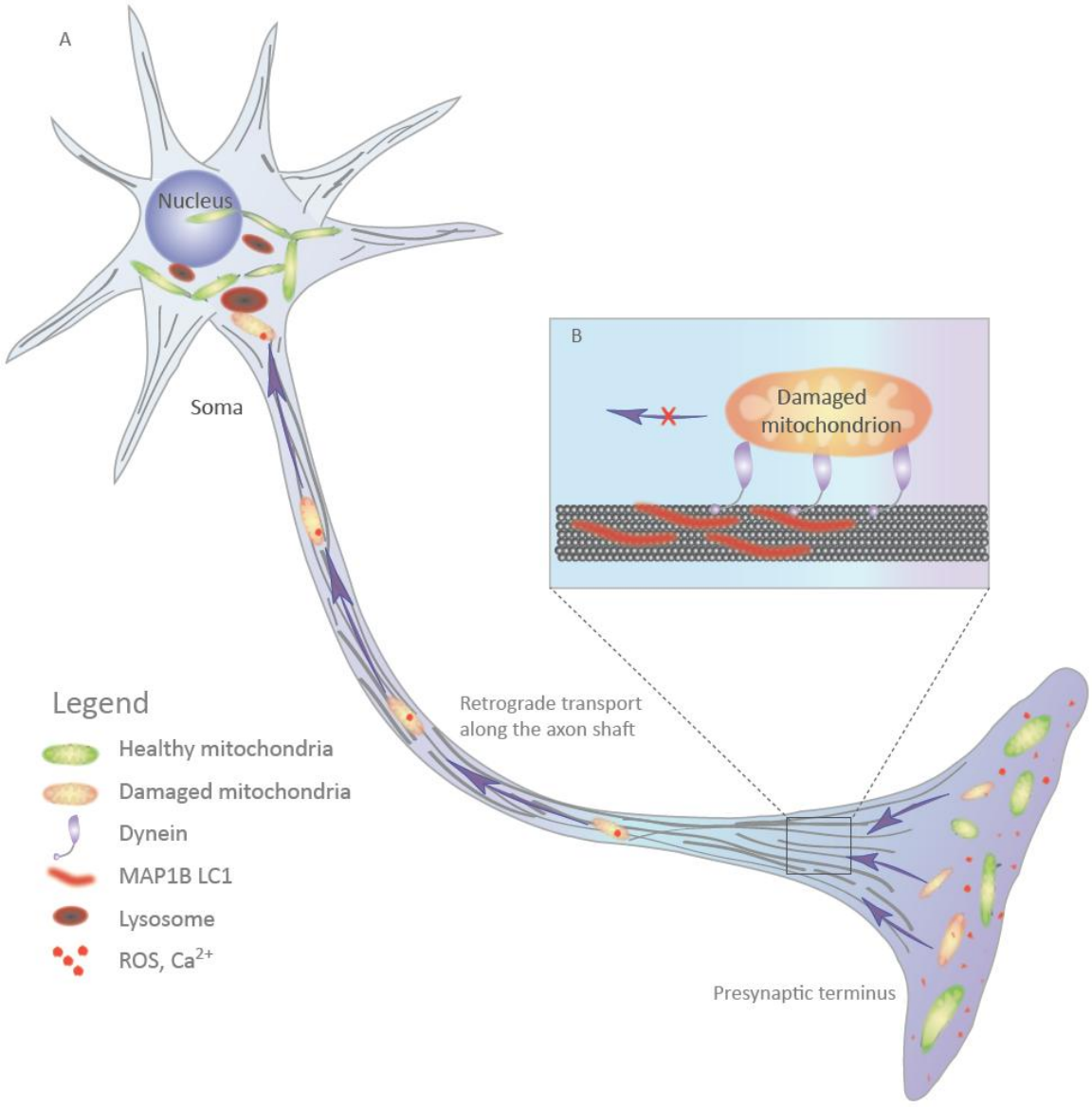

Fig. 4.1 Retrograde transport of mitochondria

(A) In healthy neurons, mitochondria located at the synaptic terminus are exposed to high concentrations of reactive oxygen species (ROS) and Ca^{2+} and simultaneously they are burdened with a high demand of ATP. Damaged mitochondria are transported back to the soma with the help of dyneins, where they fuse with lysosomes as the final step of mitophagy takes place, ensuring that damaged mitochondria will not generate an excess of reactive oxygen species (ROS). **(B)** If MAP1B LC1 is overly stabilized, it binds to microtubules thus blocking many of the dynein binding sites. This in turn leads to a decrease of the rate of transport of damaged mitochondria. As a result, they cannot be cleared out and can potentially lead to an excessive amount of ROS, decreased production of ATP and apoptosis.

4.5. Mice lacking FBXO7 in the forebrain display generalized brain damage

Vingill *el al*. published the first animal *Fbxo7*$^{-/-}$ model exhibiting a severe motor phenotype reminiscent of patient with parkinsonian pyramidal syndrome (PPS) and an average life expectancy of 21 days (Shojaee et al., 2008; Vingill et al., 2016). I further examined the consequences of *Fbxo7* knockout in the forebrain as a part of a larger project aiming at breaking down the phenotypic spectrum of pathological symptoms according to the protein's expression in different parts of the nervous system. There was no significant increase in apoptosis in the cortex, hippocampus nor the cerebellum in 8 week-old animals. However, there is a trend of increase in cell death in NEX-Cre;*Fbxo7*$^{fl/fl}$ animals possibly due to the fact that the process had occurred previously in the forebrain but at the time of experimental examination, the cells were not undergoing active apoptosis. This possibility is quite likely for three reasons. First, both cultured neurons and *in vivo* analysis of the conventional *Fbxo7* P18 knockout mice showed significant increase in the number of apoptotic cells (Brockelt, 2015; Vingill et al., 2016). Second, the gross cortex size area was significantly reduced in the NEX-Cre;*Fbxo7*$^{fl/fl}$ mice in comparison to the NEX-Cre control and only as a trend in comparison to the *Fbxo7*$^{fl/fl}$ mice, even though the average body weight was analogous at this time point (Vingill et al., 2016). Third, there is a marked increase in the glial fibrillary acidic protein (GFAP) inflammatory marker signal, as well as the microglia-specific Ionized calcium-binding adapter molecule 1 (Iba1) signal, implementing increased levels of astrogliosis and inflammation respectively. The relationship between astrogliosis, microgliosis and apoptosis can have different directionalities: brain damage caused by vascular insults or head injury as well as apoptosis caused by neurodegenerative diseases leads to increased astro- and microgliosis and *vice versa*, the induction of astro- or microgliosis through biological toxins causes apoptosis (Barreto et al., 2007; Hamby and Sofroniew, 2010; Herrera et al., 2000; Langston et al., 1999; Samantaray et al., 2007; Xiong et al., 2011). Since the mice were neither treated nor were they subjected to head trauma, this phenotype is most likely due to early apoptosis caused by neurodegeneration. It is interesting to note, that even though *Fbxo7* was not knocked-out in the cerebellum, there was also a marked increase of astrogliosis. The largest anatomical part of cerebellum is the cerebrocerebellum, whose major input arises from the corticobulbar tract as well as collateral axons form the corticospinal tract (Allen and Tsukahara, 1974). It is possible, that aberrations in the neuron's soma located in the cortex are projected through these tracts to the cerebellum, thus resulting in a secondary astrogliosis response. In conclusion, the NEX-Cre;*Fbxo7*$^{fl/fl}$ mice exhibit a pronounced inflammation and astrogliosis on a histological level, which is mirrored in their significantly worse performance on a battery of motor tests, such as rotarod, balance beam and hindlimb clasping (Vingill et al., 2016). These tests confirm that the

coordination, motor control and endurance are decreased and together with the observed spasticity, this animal model recapitulates the motor symptoms of PPS patients.

Since a major hallmark symptom of PPS is pyramidal tract lesions, I studied the gross morphology of the pyramidal tracts in the NEX-Cre;*Fbxo7*$^{fl/fl}$ mice and observed no lesions or neurofilamentous tangles (Di Fonzo et al., 2009; Shojaee et al., 2008). It is possible that at this age, these aberrations are found on a molecular level only, and have not been detected at the time of experimental conduction. Next, I checked for the presence of α-synuclein inclusions, but irrespective of the genotype, did not observe the formation Lewy body inclusions. Notably, both MAP1B LC1 and FBXO7 have been found in α-synuclein inclusions (Jensen et al., 2000; Zhao et al., 2013). Since Lewy bodies comprise of a plethora of proteins, I wanted to further test if FBXO7 and α-synuclein would co-immunoprecipitate, but this interaction was not confirmed through cell-based co-immunoprecipitation. Furthermore, there is no *Fbxo7*$^{-/-}$ patient's data stating that Lewy bodies are part of the PPS pathology.

4.6. Conclusion and Prospects

In this study, I confirmed that FBXO7 interacts with the microtubule associated protein 1B, and that it plays an important role in dendritogenesis and mitochondrial homeostasis. Further research will be necessary to show the exact molecular mechanism for the latter cellular process, more specifically if FBXO7 can influence the rate of retrograde transport of damaged axonal mitochondria.

The role of FBXO7 in neurodegeneration takes on two separate courses: one as part of the UPS and the second as the mitochondrial quality control machinery. These cellular mechanisms however are tightly interconnected since dysfunctions in one of these systems would lead inevitably to disturbances in the other creating a vicious circle that would ultimately lead to cellular stress and death.

The findings in this study together with the known mechanisms involved in the pathophysiology of PD, will hopefully take us a step forward towards preventing and curing PD.

5. References

1. Allen, G.I., and Tsukahara, N. (1974). Cerebrocerebellar communication systems. Physiol Rev *54*, 957-1006.
2. Baas, P.W., and Black, M.M. (1990). Individual microtubules in the axon consist of domains that differ in both composition and stability. J Cell Biol *111*, 495-509.
3. Bader, M., Benjamin, S., Wapinski, O.L., Smith, D.M., Goldberg, A.L., and Steller, H. (2011). A conserved F box regulatory complex controls proteasome activity in Drosophila. Cell *145*, 371-382.
4. Bai, C., Sen, P., Hofmann, K., Ma, L., Goebl, M., Harper, J.W., and Elledge, S.J. (1996). SKP1 connects cell cycle regulators to the ubiquitin proteolysis machinery through a novel motif, the F-box. Cell *86*, 263-274.
5. Barreto, G., Veiga, S., Azcoitia, I., Garcia-Segura, L.M., and Garcia-Ovejero, D. (2007). Testosterone decreases reactive astroglia and reactive microglia after brain injury in male rats: role of its metabolites, oestradiol and dihydrotestosterone. Eur J Neurosci *25*, 3039-3046.
6. Benitez-King, G., Ramirez-Rodriguez, G., Ortiz, L., and Meza, I. (2004). The neuronal cytoskeleton as a potential therapeutical target in neurodegenerative diseases and schizophrenia. Curr Drug Targets CNS Neurol Disord *3*, 515-533.
7. Binder, L.I., Frankfurter, A., Kim, H., Caceres, A., Payne, M.R., and Rebhun, L.I. (1984). Heterogeneity of microtubule-associated protein 2 during rat brain development. Proc Natl Acad Sci U S A *81*, 5613-5617.
8. Bisby, M.A., Tetzlaff, W., and Brown, M.C. (1995). Cell body response to injury in motoneurons and primary sensory neurons of a mutant mouse, Ola (Wld), in which Wallerian degeneration is delayed. J Comp Neurol *359*, 653-662.
9. Black, M.M., and Lee, V.M. (1988). Phosphorylation of neurofilament proteins in intact neurons: demonstration of phosphorylation in cell bodies and axons. J Neurosci *8*, 3296-3305.
10. Bloom, G.S., Luca, F.C., and Vallee, R.B. (1985). Microtubule-associated protein 1B: identification of a major component of the neuronal cytoskeleton. Proc Natl Acad Sci U S A *82*, 5404-5408.
11. Braak, H., Rub, U., Gai, W.P., and Del Tredici, K. (2003). Idiopathic Parkinson's disease: possible routes by which vulnerable neuronal types may be subject to neuroinvasion by an unknown pathogen. J Neural Transm (Vienna) *110*, 517-536.
12. Bradford, M.M. (1976). A rapid and sensitive method for the quantitation of microgram quantities of protein utilizing the principle of protein-dye binding. Anal Biochem *72*, 248-254.
13. Branco, D.M., Arduino, D.M., Esteves, A.R., Silva, D.F., Cardoso, S.M., and Oliveira, C.R. (2010). Cross-talk between mitochondria and proteasome in Parkinson's disease pathogenesis. Front Aging Neurosci *2*, 17.
14. Brockelt, D. (2015). The role of the E3 ubiquitin ligase FBXO7-SCF in early-onset Parkinson's disease
15. Brookes, P.S., Yoon, Y., Robotham, J.L., Anders, M.W., and Sheu, S.S. (2004). Calcium, ATP, and ROS: a mitochondrial love-hate triangle. Am J Physiol Cell Physiol *287*, C817-833.

16. Burchell, V.S., Nelson, D.E., Sanchez-Martinez, A., Delgado-Camprubi, M., Ivatt, R.M., Pogson, J.H., Randle, S.J., Wray, S., Lewis, P.A., Houlden, H.*, et al.* (2013). The Parkinson's disease-linked proteins Fbxo7 and Parkin interact to mediate mitophagy. Nat Neurosci *16*, 1257-1265.
17. Campello, S., Strappazzon, F., and Cecconi, F. (2014). Mitochondrial dismissal in mammals, from protein degradation to mitophagy. Biochim Biophys Acta *1837*, 451-460.
18. Cenciarelli, C., Chiaur, D.S., Guardavaccaro, D., Parks, W., Vidal, M., and Pagano, M. (1999). Identification of a family of human F-box proteins. Curr Biol *9*, 1177-1179.
19. Chan, S.L., Chua, L.L., Angeles, D.C., and Tan, E.K. (2014). MAP1B rescues LRRK2 mutant-mediated cytotoxicity. Mol Brain *7*, 29.
20. Chang, D.T., Honick, A.S., and Reynolds, I.J. (2006a). Mitochondrial trafficking to synapses in cultured primary cortical neurons. J Neurosci *26*, 7035-7045.
21. Chang, D.T., and Reynolds, I.J. (2006). Mitochondrial trafficking and morphology in healthy and injured neurons. Prog Neurobiol *80*, 241-268.
22. Chang, Y.F., Cheng, C.M., Chang, L.K., Jong, Y.J., and Yuo, C.Y. (2006b). The F-box protein Fbxo7 interacts with human inhibitor of apoptosis protein cIAP1 and promotes cIAP1 ubiquitination. Biochem Biophys Res Commun *342*, 1022-1026.
23. Chen, C.M., Chen, I.C., Huang, Y.C., Juan, H.F., Chen, Y.L., Chen, Y.C., Lin, C.H., Lee, L.C., Lee, C.M., Lee-Chen, G.J.*, et al.* (2014). FBXO7 Y52C polymorphism as a potential protective factor in Parkinson's disease. PLoS One *9*, e101392.
24. Cheng, M., Olivier, P., Diehl, J.A., Fero, M., Roussel, M.F., Roberts, J.M., and Sherr, C.J. (1999). The p21(Cip1) and p27(Kip1) CDK 'inhibitors' are essential activators of cyclin D-dependent kinases in murine fibroblasts. EMBO J *18*, 1571-1583.
25. Cox, J., and Mann, M. (2008). MaxQuant enables high peptide identification rates, individualized p.p.b.-range mass accuracies and proteome-wide protein quantification. Nat Biotechnol *26*, 1367-1372.
26. Cox, J., Neuhauser, N., Michalski, A., Scheltema, R.A., Olsen, J.V., and Mann, M. (2011). Andromeda: a peptide search engine integrated into the MaxQuant environment. J Proteome Res *10*, 1794-1805.
27. de Lau, L.M., and Breteler, M.M. (2006). Epidemiology of Parkinson's disease. Lancet Neurol *5*, 525-535.
28. Delgado-Camprubi, M., Esteras, N., Soutar, M.P., Plun-Favreau, H., and Abramov, A.Y. (2017). Deficiency of Parkinson's disease-related gene Fbxo7 is associated with impaired mitochondrial metabolism by PARP activation. Cell Death Differ *24*, 120-131.
29. Di Fonzo, A., Dekker, M.C., Montagna, P., Baruzzi, A., Yonova, E.H., Correia Guedes, L., Szczerbinska, A., Zhao, T., Dubbel-Hulsman, L.O., Wouters, C.H.*, et al.* (2009). FBXO7 mutations cause autosomal recessive, early-onset parkinsonian-pyramidal syndrome. Neurology *72*, 240-245.
30. Diaz-Nido, J., Serrano, L., Hernandez, M.A., and Avila, J. (1990). Phosphorylation of microtubule proteins in rat brain at different developmental stages: comparison with that found in neuronal cultures. J Neurochem *54*, 211-222.
31. Ding, K., Shameer, K., Jouni, H., Masys, D.R., Jarvik, G.P., Kho, A.N., Ritchie, M.D., McCarty, C.A., Chute, C.G., Manolio, T.A.*, et al.* (2012). Genetic Loci implicated in erythroid differentiation and cell cycle regulation are associated with red blood cell traits. Mayo Clin Proc *87*, 461-474.
32. Engelender, S. (2008). Ubiquitination of alpha-synuclein and autophagy in Parkinson's disease. Autophagy *4*, 372-374.

33. Forno, L.S., and Norville, R.L. (1976). Ultrastructure of Lewy bodies in the stellate ganglion. Acta Neuropathol *34*, 183-197.
34. Friedman, J.R., and Nunnari, J. (2014). Mitochondrial form and function. Nature *505*, 335-343.
35. Galan, J.M., Wiederkehr, A., Seol, J.H., Haguenauer-Tsapis, R., Deshaies, R.J., Riezman, H., and Peter, M. (2001). Skp1p and the F-box protein Rcy1p form a non-SCF complex involved in recycling of the SNARE Snc1p in yeast. Mol Cell Biol *21*, 3105-3117.
36. Gavrieli, Y., Sherman, Y., and Ben-Sasson, S.A. (1992). Identification of programmed cell death in situ via specific labeling of nuclear DNA fragmentation. J Cell Biol *119*, 493-501.
37. Gegg, M.E., Cooper, J.M., Chau, K.Y., Rojo, M., Schapira, A.H., and Taanman, J.W. (2010). Mitofusin 1 and mitofusin 2 are ubiquitinated in a PINK1/parkin-dependent manner upon induction of mitophagy. Hum Mol Genet *19*, 4861-4870.
38. Goebbels, S., Bormuth, I., Bode, U., Hermanson, O., Schwab, M.H., and Nave, K.A. (2006). Genetic targeting of principal neurons in neocortex and hippocampus of NEX-Cre mice. Genesis *44*, 611-621.
39. Goldman, J.G., and Postuma, R. (2014). Premotor and nonmotor features of Parkinson's disease. Curr Opin Neurol *27*, 434-441.
40. Gonzalez-Billault, C., Avila, J., and Caceres, A. (2001). Evidence for the role of MAP1B in axon formation. Mol Biol Cell *12*, 2087-2098.
41. Gonzalez-Billault, C., Owen, R., Gordon-Weeks, P.R., and Avila, J. (2002). Microtubule-associated protein 1B is involved in the initial stages of axonogenesis in peripheral nervous system cultured neurons. Brain Res *943*, 56-67.
42. Goold, R.G., Owen, R., and Gordon-Weeks, P.R. (1999). Glycogen synthase kinase 3beta phosphorylation of microtubule-associated protein 1B regulates the stability of microtubules in growth cones. J Cell Sci *112 (Pt 19)*, 3373-3384.
43. Hamby, M.E., and Sofroniew, M.V. (2010). Reactive astrocytes as therapeutic targets for CNS disorders. Neurotherapeutics *7*, 494-506.
44. Hammarback, J.A., Obar, R.A., Hughes, S.M., and Vallee, R.B. (1991). MAP1B is encoded as a polyprotein that is processed to form a complex N-terminal microtubule-binding domain. Neuron *7*, 129-139.
45. Henslee, J.G., and Srere, P.A. (1979). Resolution of rat mitochondrial matrix proteins by two-dimensional polyacrylamide gel electrophoresis. J Biol Chem *254*, 5488-5497.
46. Herrera, A.J., Castano, A., Venero, J.L., Cano, J., and Machado, A. (2000). The single intranigral injection of LPS as a new model for studying the selective effects of inflammatory reactions on dopaminergic system. Neurobiol Dis *7*, 429-447.
47. Hirokawa, N. (1994). Microtubule organization and dynamics dependent on microtubule-associated proteins. Curr Opin Cell Biol *6*, 74-81.
48. Hsu, J.M., Lee, Y.C., Yu, C.T., and Huang, C.Y. (2004). Fbx7 functions in the SCF complex regulating Cdk1-cyclin B-phosphorylated hepatoma up-regulated protein (HURP) proteolysis by a proline-rich region. J Biol Chem *279*, 32592-32602.
49. Ikegami, K., and Setou, M. (2010). Unique post-translational modifications in specialized microtubule architecture. Cell Struct Funct *35*, 15-22.
50. Jamison DT, Jha P, Malhotra V, Verguet S. Human health: the twentieth century transformation of human health—its magnitude and value" In: How much have global problems cost the world. Cambridge: Cambridge University Press; 2013. 207–46.)

51. Jensen, P.H., Islam, K., Kenney, J., Nielsen, M.S., Power, J., and Gai, W.P. (2000). Microtubule-associated protein 1B is a component of cortical Lewy bodies and binds alpha-synuclein filaments. J Biol Chem *275*, 21500-21507.
52. Jimenez-Mateos, E.M., Gonzalez-Billault, C., Dawson, H.N., Vitek, M.P., and Avila, J. (2006). Role of MAP1B in axonal retrograde transport of mitochondria. Biochem J *397*, 53-59.
53. Julien, J.P., and Mushynski, W.E. (1998). Neurofilaments in health and disease. Prog Nucleic Acid Res Mol Biol *61*, 1-23.
54. Kirk, R., Laman, H., Knowles, P.P., Murray-Rust, J., Lomonosov, M., Meziane el, K., and McDonald, N.Q. (2008). Structure of a conserved dimerization domain within the F-box protein Fbxo7 and the PI31 proteasome inhibitor. J Biol Chem *283*, 22325-22335.
55. Klein, C., and Schlossmacher, M.G. (2007). Parkinson disease, 10 years after its genetic revolution: multiple clues to a complex disorder. Neurology *69*, 2093-2104.
56. Klein, C., and Westenberger, A. (2012). Genetics of Parkinson's disease. Cold Spring Harb Perspect Med *2*, a008888.
57. Komander, D. (2009). The emerging complexity of protein ubiquitination. Biochem Soc Trans *37*, 937-953.
58. Kondapalli, C., Kazlauskaite, A., Zhang, N., Woodroof, H.I., Campbell, D.G., Gourlay, R., Burchell, L., Walden, H., Macartney, T.J., Deak, M.*, et al.* (2012). PINK1 is activated by mitochondrial membrane potential depolarization and stimulates Parkin E3 ligase activity by phosphorylating Serine 65. Open Biol *2*, 120080.
59. Konishi, Y., Stegmuller, J., Matsuda, T., Bonni, S., and Bonni, A. (2004). Cdh1-APC controls axonal growth and patterning in the mammalian brain. Science *303*, 1026-1030.
60. Laemmli, U.K. (1970). Cleavage of structural proteins during the assembly of the head of bacteriophage T4. Nature *227*, 680-685.
61. Laman, H., Funes, J.M., Ye, H., Henderson, S., Galinanes-Garcia, L., Hara, E., Knowles, P., McDonald, N., and Boshoff, C. (2005). Transforming activity of Fbxo7 is mediated specifically through regulation of cyclin D/cdk6. EMBO J *24*, 3104-3116.
62. Langkopf, A., Hammarback, J.A., Muller, R., Vallee, R.B., and Garner, C.C. (1992). Microtubule-associated proteins 1A and LC2. Two proteins encoded in one messenger RNA. J Biol Chem *267*, 16561-16566.
63. Langston, J.W., Ballard, P., Tetrud, J.W., and Irwin, I. (1983). Chronic Parkinsonism in humans due to a product of meperidine-analog synthesis. Science *219*, 979-980.
64. Langston, J.W., Forno, L.S., Tetrud, J., Reeves, A.G., Kaplan, J.A., and Karluk, D. (1999). Evidence of active nerve cell degeneration in the substantia nigra of humans years after 1-methyl-4-phenyl-1,2,3,6-tetrahydropyridine exposure. Ann Neurol *46*, 598-605.
65. Liz, M.A., Mar, F.M., Santos, T.E., Pimentel, H.I., Marques, A.M., Morgado, M.M., Vieira, S., Sousa, V.F., Pemble, H., Wittmann, T.*, et al.* (2014). Neuronal deletion of GSK3beta increases microtubule speed in the growth cone and enhances axon regeneration via CRMP-2 and independently of MAP1B and CLASP2. BMC Biol *12*, 47.
66. Lohmann, E., Coquel, A.S., Honore, A., Gurvit, H., Hanagasi, H., Emre, M., Leutenegger, A.L., Drouet, V., Sahbatou, M., Guven, G.*, et al.* (2015). A new F-box protein 7 gene mutation causing typical Parkinson's disease. Mov Disord *30*, 1130-1133.
67. Lowry, O.H., Rosebrough, N.J., Farr, A.L., and Randall, R.J. (1951). Protein measurement with the Folin phenol reagent. J Biol Chem *193*, 265-275.

68. Lu, C., Pribanic, S., Debonneville, A., Jiang, C., and Rotin, D. (2007). The PY motif of ENaC, mutated in Liddle syndrome, regulates channel internalization, sorting and mobilization from subapical pool. Traffic *8*, 1246-1264.
69. Mandelkow, E., and Mandelkow, E.M. (1995). Microtubules and microtubule-associated proteins. Curr Opin Cell Biol *7*, 72-81.
70. Mattson, M.P., Taylor-Hunter, A., and Kater, S.B. (1988). Neurite outgrowth in individual neurons of a neuronal population is differentially regulated by calcium and cyclic AMP. J Neurosci *8*, 1704-1711.
71. Matus, A. (1988). Microtubule-associated proteins: their potential role in determining neuronal morphology. Annu Rev Neurosci *11*, 29-44.
72. Meixner, A., Haverkamp, S., Wassle, H., Fuhrer, S., Thalhammer, J., Kropf, N., Bittner, R.E., Lassmann, H., Wiche, G., and Propst, F. (2000). MAP1B is required for axon guidance and Is involved in the development of the central and peripheral nervous system. J Cell Biol *151*, 1169-1178.
73. Meziane el, K., Randle, S.J., Nelson, D.E., Lomonosov, M., and Laman, H. (2011). Knockdown of Fbxo7 reveals its regulatory role in proliferation and differentiation of haematopoietic precursor cells. J Cell Sci *124*, 2175-2186.
74. Miller, K.E., and Sheetz, M.P. (2004). Axonal mitochondrial transport and potential are correlated. J Cell Sci *117*, 2791-2804.
75. Mohri, H. (1968). Amino-acid composition of "Tubulin" constituting microtubules of sperm flagella. Nature *217*, 1053-1054.
76. Morris, R.L., and Hollenbeck, P.J. (1993). The regulation of bidirectional mitochondrial transport is coordinated with axonal outgrowth. J Cell Sci *104 (Pt 3)*, 917-927.
77. Munch, C., and Harper, J.W. (2016). Mitochondrial unfolded protein response controls matrix pre-RNA processing and translation. Nature *534*, 710-713.
78. Nakamura, T., and Lipton, S.A. (2009). Cell death: protein misfolding and neurodegenerative diseases. Apoptosis *14*, 455-468.
79. Narendra, D., Walker, J.E., and Youle, R. (2012). Mitochondrial quality control mediated by PINK1 and Parkin: links to parkinsonism. Cold Spring Harb Perspect Biol *4*.
80. Narendra, D.P., Jin, S.M., Tanaka, A., Suen, D.F., Gautier, C.A., Shen, J., Cookson, M.R., and Youle, R.J. (2010). PINK1 is selectively stabilized on impaired mitochondria to activate Parkin. PLoS Biol *8*, e1000298.
81. Nelson, D.E., and Laman, H. (2011). A Competitive binding mechanism between Skp1 and exportin 1 (CRM1) controls the localization of a subset of F-box proteins. J Biol Chem *286*, 19804-19815.
82. Nelson, D.E., Randle, S.J., and Laman, H. (2013). Beyond ubiquitination: the atypical functions of Fbxo7 and other F-box proteins. Open Biol *3*, 130131.
83. Noiges, R., Eichinger, R., Kutschera, W., Fischer, I., Nemeth, Z., Wiche, G., and Propst, F. (2002). Microtubule-associated protein 1A (MAP1A) and MAP1B: light chains determine distinct functional properties. J Neurosci *22*, 2106-2114.
84. Ohyu, J., Yamanouchi, H., and Takashima, S. (1997). Immunohistochemical study of microtubule-associated protein 5 (MAP5) expression in the developing human brain. Brain Dev *19*, 541-546.
85. Orban-Nemeth, Z., Simader, H., Badurek, S., Trancikova, A., and Propst, F. (2005). Microtubule-associated protein 1S, a short and ubiquitously expressed member of the microtubule-associated protein 1 family. J Biol Chem *280*, 2257-2265.

86. Paisan-Ruiz, C., Guevara, R., Federoff, M., Hanagasi, H., Sina, F., Elahi, E., Schneider, S.A., Schwingenschuh, P., Bajaj, N., Emre, M.*, et al.* (2010). Early-onset L-dopa-responsive parkinsonism with pyramidal signs due to ATP13A2, PLA2G6, FBXO7 and spatacsin mutations. Mov Disord *25*, 1791-1800.
87. Polymeropoulos, M.H., Higgins, J.J., Golbe, L.I., Johnson, W.G., Ide, S.E., Di Iorio, G., Sanges, G., Stenroos, E.S., Pho, L.T., Schaffer, A.A.*, et al.* (1996). Mapping of a gene for Parkinson's disease to chromosome 4q21-q23. Science *274*, 1197-1199.
88. Riederer, B., Cohen, R., and Matus, A. (1986). MAP5: a novel brain microtubule-associated protein under strong developmental regulation. J Neurocytol *15*, 763-775.
89. Saiki, R.K., Scharf, S., Faloona, F., Mullis, K.B., Horn, G.T., Erlich, H.A., and Arnheim, N. (1985). Enzymatic amplification of beta-globin genomic sequences and restriction site analysis for diagnosis of sickle cell anemia. Science *230*, 1350-1354.
90. Samantaray, S., Knaryan, V.H., Guyton, M.K., Matzelle, D.D., Ray, S.K., and Banik, N.L. (2007). The parkinsonian neurotoxin rotenone activates calpain and caspase-3 leading to motoneuron degeneration in spinal cord of Lewis rats. Neuroscience *146*, 741-755.
91. Sarraf, S.A., Raman, M., Guarani-Pereira, V., Sowa, M.E., Huttlin, E.L., Gygi, S.P., and Harper, J.W. (2013). Landscape of the PARKIN-dependent ubiquitylome in response to mitochondrial depolarization. Nature *496*, 372-376.
92. Scarffe, L.A., Stevens, D.A., Dawson, V.L., and Dawson, T.M. (2014). Parkin and PINK1: much more than mitophagy. Trends Neurosci *37*, 315-324.
93. Schnapp, B.J., and Reese, T.S. (1989). Dynein is the motor for retrograde axonal transport of organelles. Proc Natl Acad Sci U S A *86*, 1548-1552.
94. Schnapp, B.J., Reese, T.S., and Bechtold, R. (1992). Kinesin is bound with high affinity to squid axon organelles that move to the plus-end of microtubules. J Cell Biol *119*, 389-399.
95. Sena, L.A., and Chandel, N.S. (2012). Physiological roles of mitochondrial reactive oxygen species. Mol Cell *48*, 158-167.
96. Shendelman, S., Jonason, A., Martinat, C., Leete, T., and Abeliovich, A. (2004). DJ-1 is a redox-dependent molecular chaperone that inhibits alpha-synuclein aggregate formation. PLoS Biol *2*, e362.
97. Sherriff, F.E., Bridges, L.R., Gentleman, S.M., Sivaloganathan, S., and Wilson, S. (1994). Markers of axonal injury in post mortem human brain. Acta Neuropathol *88*, 433-439.
98. Shojaee, S., Sina, F., Banihosseini, S.S., Kazemi, M.H., Kalhor, R., Shahidi, G.A., Fakhrai-Rad, H., Ronaghi, M., and Elahi, E. (2008). Genome-wide linkage analysis of a Parkinsonian-pyramidal syndrome pedigree by 500 K SNP arrays. Am J Hum Genet *82*, 1375-1384.
99. Shulman, J.M., De Jager, P.L., and Feany, M.B. (2011). Parkinson's disease: genetics and pathogenesis. Annu Rev Pathol *6*, 193-222.
100. Soranzo, N., Spector, T.D., Mangino, M., Kuhnel, B., Rendon, A., Teumer, A., Willenborg, C., Wright, B., Chen, L., Li, M.*, et al.* (2009). A genome-wide meta-analysis identifies 22 loci associated with eight hematological parameters in the HaemGen consortium. Nat Genet *41*, 1182-1190.
101. Teixeira, F.R., Randle, S.J., Patel, S.P., Mevissen, T.E., Zenkeviciute, G., Koide, T., Komander, D., and Laman, H. (2016). Gsk3beta and Tomm20 are substrates of the SCFFbxo7/PARK15 ubiquitin ligase associated with Parkinson's disease. Biochem J *473*, 3563-3580.
102. Teng, J., Takei, Y., Harada, A., Nakata, T., Chen, J., and Hirokawa, N. (2001). Synergistic effects of MAP2 and MAP1B knockout in neuronal migration, dendritic outgrowth, and microtubule organization. J Cell Biol *155*, 65-76.

103. Togel, M., Wiche, G., and Propst, F. (1998a). Evidence against structural and functional identity of microtubule-associated protein 1B and proteoglycan daustrin. FEBS Lett *423*, 254-258.
104. Togel, M., Wiche, G., and Propst, F. (1998b). Novel features of the light chain of microtubule-associated protein MAP1B: microtubule stabilization, self interaction, actin filament binding, and regulation by the heavy chain. J Cell Biol *143*, 695-707.
105. Tong, J., Ang, L.C., Williams, B., Furukawa, Y., Fitzmaurice, P., Guttman, M., Boileau, I., Hornykiewicz, O., and Kish, S.J. (2015). Low levels of astroglial markers in Parkinson's disease: relationship to alpha-synuclein accumulation. Neurobiol Dis *82*, 243-253.
106. Tucker, R.P., Garner, C.C., and Matus, A. (1989). In situ localization of microtubule-associated protein mRNA in the developing and adult rat brain. Neuron *2*, 1245-1256.
107. Valente, E.M., Abou-Sleiman, P.M., Caputo, V., Muqit, M.M., Harvey, K., Gispert, S., Ali, Z., Del Turco, D., Bentivoglio, A.R., Healy, D.G.*, et al.* (2004). Hereditary early-onset Parkinson's disease caused by mutations in PINK1. Science *304*, 1158-1160.
108. van der Harst, P., Zhang, W., Mateo Leach, I., Rendon, A., Verweij, N., Sehmi, J., Paul, D.S., Elling, U., Allayee, H., Li, X.*, et al.* (2012). Seventy-five genetic loci influencing the human red blood cell. Nature *492*, 369-375.
109. Van Laar, V.S., and Berman, S.B. (2009). Mitochondrial dynamics in Parkinson's disease. Exp Neurol *218*, 247-256.
110. Viereck, C., Tucker, R.P., and Matus, A. (1989). The adult rat olfactory system expresses microtubule-associated proteins found in the developing brain. J Neurosci *9*, 3547-3557.
111. Vingill, S., Brockelt, D., Lancelin, C., Tatenhorst, L., Dontcheva, G., Preisinger, C., Schwedhelm-Domeyer, N., Joseph, S., Mitkovski, M., Goebbels, S.*, et al.* (2016). Loss of FBXO7 (PARK15) results in reduced proteasome activity and models a parkinsonism-like phenotype in mice. EMBO J *35*, 2008-2025.
112. Wakabayashi, K., Hayashi, S., Kakita, A., Yamada, M., Toyoshima, Y., Yoshimoto, M., and Takahashi, H. (1998). Accumulation of alpha-synuclein/NACP is a cytopathological feature common to Lewy body disease and multiple system atrophy. Acta Neuropathol *96*, 445-452.
113. Wang, Z., Zhang, Y., Zhang, S., Guo, Q., Tan, Y., Wang, X., Xiong, R., Ding, J., and Chen, S. (2011). DJ-1 can inhibit microtubule associated protein 1 B formed aggregates. Mol Neurodegener *6*, 38.
114. Whitworth, A.J., Lee, J.R., Ho, V.M., Flick, R., Chowdhury, R., and McQuibban, G.A. (2008). Rhomboid-7 and HtrA2/Omi act in a common pathway with the Parkinson's disease factors Pink1 and Parkin. Dis Model Mech *1*, 168-174; discussion 173.
115. Willems, A.R., Schwab, M., and Tyers, M. (2004). A hitchhiker's guide to the cullin ubiquitin ligases: SCF and its kin. Biochim Biophys Acta *1695*, 133-170.
116. Winston, J.T., Koepp, D.M., Zhu, C., Elledge, S.J., and Harper, J.W. (1999). A family of mammalian F-box proteins. Curr Biol *9*, 1180-1182.
117. Xiong, X., Barreto, G.E., Xu, L., Ouyang, Y.B., Xie, X., and Giffard, R.G. (2011). Increased brain injury and worsened neurological outcome in interleukin-4 knockout mice after transient focal cerebral ischemia. Stroke *42*, 2026-2032.
118. Yalcin-Cakmakli, G., Olgiati, S., Quadri, M., Breedveld, G.J., Cortelli, P., Bonifati, V., and Elibol, B. (2014). A new Turkish family with homozygous FBXO7 truncating mutation and juvenile atypical parkinsonism. Parkinsonism Relat Disord *20*, 1248-1252.
119. Yi, J.J., and Ehlers, M.D. (2007). Emerging roles for ubiquitin and protein degradation in neuronal function. Pharmacol Rev *59*, 14-39.

120. Yonashiro, R., Kimijima, Y., Shimura, T., Kawaguchi, K., Fukuda, T., Inatome, R., and Yanagi, S. (2012). Mitochondrial ubiquitin ligase MITOL blocks S-nitrosylated MAP1B-light chain 1-mediated mitochondrial dysfunction and neuronal cell death. Proc Natl Acad Sci U S A *109*, 2382-2387.
121. Youle, R.J., and Narendra, D.P. (2011). Mechanisms of mitophagy. Nat Rev Mol Cell Biol *12*, 9-14.
122. Youle, R.J., and van der Bliek, A.M. (2012). Mitochondrial fission, fusion, and stress. Science *337*, 1062-1065.
123. Zhang, L., Shimoji, M., Thomas, B., Moore, D.J., Yu, S.W., Marupudi, N.I., Torp, R., Torgner, I.A., Ottersen, O.P., Dawson, T.M.*, et al.* (2005). Mitochondrial localization of the Parkinson's disease related protein DJ-1: implications for pathogenesis. Hum Mol Genet *14*, 2063-2073.
124. Zhao, T., De Graaff, E., Breedveld, G.J., Loda, A., Severijnen, L.A., Wouters, C.H., Verheijen, F.W., Dekker, M.C., Montagna, P., Willemsen, R.*, et al.* (2011). Loss of nuclear activity of the FBXO7 protein in patients with parkinsonian-pyramidal syndrome (PARK15). PLoS One *6*, e16983.
125. Zhao, T., Severijnen, L.A., van der Weiden, M., Zheng, P.P., Oostra, B.A., Hukema, R.K., Willemsen, R., Kros, J.M., and Bonifati, V. (2013). FBXO7 immunoreactivity in alpha-synuclein-containing inclusions in Parkinson disease and multiple system atrophy. J Neuropathol Exp Neurol *72*, 482-488.
126. Zhou, Z.D., Xie, S.P., Sathiyamoorthy, S., Saw, W.T., Sing, T.Y., Ng, S.H., Chua, H.P., Tang, A.M., Shaffra, F., Li, Z.*, et al.* (2015). F-box protein 7 mutations promote protein aggregation in mitochondria and inhibit mitophagy. Hum Mol Genet *24*, 6314-6330.

Acknowledgements

First and foremost I would like to express my gratitude towards PD Dr. Judith Stegmüller for giving me the opportunity to make my passion into reality by introducing me into the world of science. Her drive and devotion to science is truly inspirational and served as motivation for me. She has given me the precious knowledge through many advices and persistent mentoring on how to be an honest, strong and virtuous scientist. Thank you!

I consider myself privileged to have Prof. Dr. Anastassia Stoykova and Prof. Dr. Nils Brose as thesis committee members. Thank you for the support and the readiness to help and for all the inputs and discussions that have enriched my PhD thesis.

This whole journey would not have been possible if it wasn't for the IMPRS program, Prof. Dr. Michael Hörner, Sandra Drube and Katharina Gramberg. I highly appreciate their incredible work to make everything for the students to flow as easy as possible. The support I received from the IMPRS and the GGNB is immense and I truly, truly cherish the fact that I am affiliated with these programs. This work was partially supported by the Göttingen Graduate School for Neurosciences, Biophysics, and Molecular Biosciences Bridging fund and the Michael J. Fox Foundation for Parkinson's Research.

I would also like to thank everyone at the amazing Max Planck Institute of Experimental Medicine, Göttingen. It was truly a great experience to start my Ph.D. project there and I am very proud to be part of the Max Planck Society. Furthermore, I would also like to thank Prof. Dr. Jörg Schulz for welcoming us at the Department of Neurology at the University Hospital, RWTH Aachen and for his interest and suggestions in my PhD project.

A big thank you to my colleagues that worked together with me during my time in the lab. I am extremely lucky to have Sabitha as my lab-mate, support and friend from day one. Your sense of humour, intelligence and courage has been contagious and I will miss your positive influence and our happy times together. Thank you for your readiness to help whatever the situation! I am so happy to also have Vibha as a colleague and friend, whose support and colorful attitude towards the world also brought positivity and lightness in my life. Thank you also for proof-reading my thesis. I would like to thank Nikola, Anna, Siv, Chaitali, Shih-Ju, Annika and especially David for helping me during my starting year. My best wishes to the exceptionally sweet and intelligent Yuhao and Chuan, and I hope you continue the cheerful vibes of the "Awesome" group. Thank you Daniel, Simon, Anna, Jens and Theodora for accepting us with such readiness, and making our transition into Aachen as pleasant and homey as possible. Last but not least, thank you Mathias for your help, advices, and the pleasant company during our coffee breaks, as well as for proof-reading my Ph.D. Thesis.

Acknowledgements

The biggest joy of my life is my family. Salim Burak being the newest member helped me a lot and thought me many new things I would never imagine knowing. You kept me going and happy and for this and many, many other things, seni seviyorum! I cannot express my gratitude towards my parents and my sister for being the best role-models and my biggest support and all my achievements in life are a reality because of them! Обичам ви! И последни, но най-хубави думи за баба- благодаря ти, че си ни отгледала с толква любов и си ни научила да бъдем искрени и борбени! Я тебя очень люблю!

Appendix

Table A List of primer sequences used in this study and their corresponding number

	Primer number	Sequence 5'-3'	Description
Cloning	15222	ATATGAATTCATATGAGGCTGCGGGTG	pCMV-myc fwd
	15223	ATATGGTACCTCACATGAATGACAGCCGG	pCMV-myc rev
	32501	ATAAAGCTTATGGTGGACCCGGAGGCGCTA	MAP1S LC fwd
	29440	CTCGTCGACCTAGAACTCCACCTTGCAGGCC	MAP1S LC rev
	32890	GATCCCCGGCCTCCCTGTGTATTTGGA TTCAAGCTTTCCAAATACACAGGGAGGCCTTTT	functional LC1 RNAi, fwd
	32991	AGCTAAAAAGGCCTCCCTGTGTATTTGGAAAGTTAACGTCCAA ATACACAGGGAGGCCGG	functional LC1 RNAi, rev
	32888	GATCCCCTGCAAGACCGAAGCCCTTCTTCAAGCTTGAAG GGCTTCGGTCTTGCATTTT	non-functional LC1 RNAi, fwd
	32989	AGCTAAAAATGCAAGACCGAAGCCCTTCTTCAAGCTTGAAGGG CTTCGGTCTTGCAGGG	non-functional LC1 RNAi, rev
Genotyping	31215	GGGCTGTATGAAGGAAGTGCTATT	FBXO7 wt, fwd
	31214	CCCTGAGAGTGAAGGGTGCTGTTC	FBXO7 wt, rev
	04193-9	CAGGGTGTTATAAGCAATCCC	Cre, fwd
	04192-8	CCTGGAAAATGCTTCTGCCG	Cre, rev

Appendix

Table B List of plasmid vectors used in this study

Vector	cDNA/shRNA	Generated by
pSUPER	shFBXO7 #1	Siv Vingill
pSUPER	shFBXO7 #4	Siv VIngill
pSUPER	shFBXO7 #1	Guergana Dontcheva
pSUPER	shFBXO7 #3	Guergana Dontcheva
pCMV-myc	FBXO7	Madhuvanthi Kannan
pCMV-myc	FBXO7 T22M	Siv VIngill
pCMV-myc	FBXO7 M115I	Siv VIngill
pCMV-myc	FBXO7 R378G	Siv VIngill
pCMV-myc	FBXO7 R598X	Siv VIngill
pCMV-myc	FBXO7 ΔN-terminus	Siv VIngill
pCMV-myc	FBXO7 ΔUbl	Siv VIngill
pCMV-myc	FBXO7 ΔPRR	Siv VIngill
pCMV-myc	FBXO7 ΔFP	Siv VIngill
pCMV-myc	FBXO7 ΔC-terminus	Siv VIngill
pCMV-myc	FBXO7 Δfbox	Siv VIngill
pCMV10-3xFLAG	MAP1B LC1	David Brockelt
pCMV10-3xFLAG	MAP1B LC2	David Brockelt
pCMV10-3xFLAG	MAP1S LC	Guergana Dontcheva
pCMV10-3xFLAG	FBXO7	Siv Vingill
pRK-HA	Ubiquitin	Hiroshi Kawabe
pcDNA3.0	FBXO7-FLAG	Siv Vingill
pcDNA3.0	Bcl-xL	-
pEGFP-N1	α-Synudein wt	Theodora Saridaki

Abbreviations

List of all abbreviations used within this thesis:

Abbreviation	Spelled-out version
°C	Degrees Celsius
aa	Amino acid
ADP	Adenosine diphosphate
ANOVA	Analysis of variance
APP	Amyloid precursor protein
APS	Ammonium Persulfate
ATP	Adenosine triphosphate
ATP13A2	ATPase 13A2
β-gal	β-galactosidase
Bcl-xL	B-cell lymphoma-extra large
BME	Basal medium eagle
bp	Base pairs
BSA	Bovine serum albumin
ca.	circa
Cdk6	Cyclin-dependent kinase 6
cDNA	Complimentary Deoxyribonucleic acid
CIP	Calf intestinal phosphatase
CMV	Cytomegalovirus
Co-IP	Co-immunoprecipitation
DAB	3,3'-diaminobenzidine
DAPI	4',6-diamidino-2-phenylindole
dd	Double distilled

DIV	Day *in vitro*
DMEM	Dulbecco's modified eagle medium
DmPI31	Drosophila melanogaster Proteasome inhibitor 31
DNA	Deoxyribonucleic acid
DTT	1,4-dithiothreitol
dNTP	Nucleoside triphosphate
DTT	Dithiothreitol
DUB	Deubiquitinating enzyme
E1	Ubiquitin activating enzyme
E2	Ubiquitin conjugating enzyme
E3	Ubiquitin ligase enzyme
EDTA	Ethylene-diaminetetraacetic acid
ERAD	Endoplasmic reticulum-associated degradation
FBXO7	F-box protein other 7
FRT	Flippase recognition target
g	gram
GFAP	Glial fibrillary acidic protein
GFP	Green fluorescent protein
GSK3β	Glycogen synthase kinase 3 β
HA	Hemagglutinin
HBSS	Hank's balanced salt solution
HC	Heavy chain
HEK	Human enbryonic kidney
HEPES	4-(2-hydroxyethyl)-1-piperazineethanesulfonic acid
Het	Heterozygous
Hom	Homozygous
hr	hour

HRP	Horseradish peroxidase
HURP	Hepatoma up-regulated protein
IB	Immunoblot
Iba1	Ionized calcium-binding adapter molecule 1
ICC	Immunocytochemistry
$IgG_{(H/L)}$	Immunoglobulin G (heavy/light chain)
IHC	Immunohistochemistry
IP	Immunoprecipitate
IVS	InterVening Sequence (intron)
kb	Kilobase
kDa	Kilodalton
LC	Light chain
LRRK2	Leucine-rich repeat kinase 2
M	Molar
MAP	Microtubule associated protein
Mfn	Mitofusin
mA	Milli Ampers
mg	Milligram
µg	Microgram
Miro	Mitochondrial Rho GTPase 1
mm^2	Square millimeter
mM	Millimolar
µM	Micromolar
mL	Milliliter
µL	Microliter
MPTP	1-Methyl-4-phenyl-1,2,3,6-tetrahydropyridin
MT	Microtubule

N	Number
NAD	Nicotinamide adenine dinucleotide
NEM	N-ethylmaleimide
NEX	Neuronal basic helix-loop-helix
NFM	Neurofilament, medium
ng	nanogram
nm	nanometer
neo	neomycin
n.s.	non-significant
OCT	Ornithine-carbamyl transferase
OOM	Outer mitochondrial membrane
P	Postnatal day
PAGE	Polyacrylamide gel electrophoresis
PARP	Poly [ADP-ribose] polymerase
PINK1	PTEN-induced putative kinase 1
PBS	Phosphate buffered saline
PCR	Polymerase chain reaction
PD	Parkinson's disease
PFA	Paraformaldehyde
PI31	Proteasomal inhibitor 31
pmol	picomol
PPS	Parkinsonian pyramidal syndrome
PSG	Penicillin, streptomycin, L-glutamine
PSMA	Proteasomal subunit α
PSMA2	Proteasomal subunit β
Rbx1	RING-box protein 1
Rcy1	Recyclin1

REM	Rapid-eye movement
RIPA	Radioimmunopresipitation assay buffer
RNA	Ribonucleic acid
RNAi	Ribonucleic acid interference
ROS	Reactive oxygen species
rpm	Revolutions per minute
RT	Room Temperature
SCF	Skp1, Cullin, F-box containing complex
sec	Second
SDS	Sodium dodecyl sulfate
SDS-PAGE	Sodium dodecyl sulfate-Polyacrilamide gel electrophoresis
s.e.m.	Standard error of mean
Skp1	S-phase kinase-associated protein 1
SNCA	Synuclein, α
SNP	Single nucleotide polymorpohism
S.O.C.	Super optimal broth with catabolite repression
shRNA	Short hairpin ribonucleic acid
TAE	Tris Base, Acetic acid, EDTA
TEMED	Tetra-methyl-ethylene-diamine
TUNEL	Terminal deoxynucleotidyl transferase dUTP nick end labeling
TdT	Terminal deoxynucleotidyl transferase
VPS35	Vacuolar protein sorting-associated protein 35
v/v	Volume per volume
Ub	Ubiquitin
UbRD	Ubiquitin-related domain
UPS	Ubiquitin proteasome system
WB	Western Blot

wt	Wild type
w/v	Weight per volume
C	Cysteine
G	Glycine
K	Lysine
L	Leucine
M	Methionine
T	Threonine
Y	Tyrosine
X	Stop
A	Adenosine
G	Guanine
C	Cytosine
T	Thymine